

https://dspace.org/

Multi-wavelength study of large-scale outflows from the Circinus galaxy

Ebrahim, Rozeena

2021
https://hdl.handle.net/10539/33032

Downloaded from a DSpace repository. https://dspace.org/

MULTI-WAVELENGTH STUDY OF LARGE-SCALE OUTFLOWS FROM THE CIRCINUS GALAXY



WITS
UNIVERSITY

A Dissertation submitted to the Faculty of Science at the University of the Witwatersrand, Johannesburg, in fulfillment of the requirements for the degree of Master of Science in Physics.

By
Rozeena Ebrahim
rozeenaebrahim14@gmail.com

Supervised by
Prof. Andrew Chen
Dr. Dmitry Prokhorov

Johannesburg, South Africa
September 2021

Declaration

I, Rozeena Ebrahim, student number [1049197], declare that this Dissertation is my own unaided work. It is being submitted for the Degree of Master of Science in Physics at the University of the Witwatersrand, Johannesburg. It has not been submitted before for any degree or examination at any other university.



(Signature of candidate)

7th day of **September** 20 **21** in **Johannesburg**

Abstract

The Circinus galaxy is a composite starburst/Seyfert galaxy that exhibits radio lobes inflated by kpc scale outflows along its minor axis. Its proximity (4 Mpc) makes it a unique target to study the physical nature of these outflows. We investigate if they originate from nuclear star formation activity or if they are jets from an active galactic core. The MeerKAT radio observations allow us to study the morphology of the arcminute lobes of the Circinus galaxy. In this work, a multi-wavelength analysis of this system is conducted using the available MeerKAT observations and Fermi-LAT data, to aid in the understanding of the origin of these structures. We found that the shell of the radio lobes is likely created by a weak shock that swept up and accelerated electrons in the interstellar medium to produce the edge-brightening effect. The MeerKAT spectral index map of the lobes also challenges previous evidence made against the starburst model. Our Fermi-LAT analysis results support a starburst origin for the GeV emission of Circinus due to the CR-ISM interaction and a proton calorimeter model for Circinus. However, we also show that the flux decline of SN1996cr as the origin of the GeV emission of Circinus cannot be ruled out. These results are also compared to the star-formation driven Fermi bubbles in the Milky Way, which have been observed in both the γ-ray and the radio bands, to determine physical similarities between these structures.

This Masters dissertation is dedicated to my parents, Halima and Nazeer, for their love, sacrifice, and motivation that has enabled me to pursue my dreams, and to my husband, Zubair, for his unwavering support, patience and encouragement throughout this degree.

Acknowledgements

This work is based on the research supported wholly/in part by the National Research Foundation of South Africa (Grant Number: 113833). This work has made use of radio data from the MeerKAT telescope, provided by the South African Radio Astronomy Observatory (SARAO). The MeerKAT telescope is operated by the South African Radio Astronomy Observatory, which is a facility of the National Research Foundation, an agency of the Department of Science and Technology. This work has also made use of γ-ray data from the *Fermi*-LAT telescope provided by the Fermi Science Support Center.

I would like to acknowledge my supervisors, Prof. Andrew Chen and Dr Dmitry Prokhorov, for the opportunity to be their student, for their constant assistance, guidance, support, and understanding, and for giving me the skills and experience needed to grow as a researcher throughout this project.

I am grateful to my collaborators on the MeerKAT observations of the Circinus galaxy project, Dr Kshitij Thorat, Dr Gyula Józsa & Dr Paolo Serra, for providing the reduced MeerKAT images of Circinus and for their advice on and review of the interpretations of the MeerKAT analysis of Circinus.

I would also like to thank Dr Jacco Vink for the useful discussions on SNe, Dr Beatriz Mingo and Dr Emil Lenc for providing their original ATCA radio maps of Circinus used in the spatial analysis and Dr Lukasz Stawarz for the idea to include external interstellar radiation fields in the broadband lobe emission model.

Presentations

64th Annual Conference of the South African Institute of Physics (SAIP)	Polokwane, South Africa	July 2019
7th High Energy Astrophysics in Southern Africa (HEASA) Conference	Swakopmund, Namibia	August 2019
30th Texas Symposium on Relativistic Astrophysics	Portsmouth, United Kingdom	December 2019
2020 SARAO Postgraduate Scholarship Conference	Virtual	December 2020
The SKA Observatory: A Precursor View of the SKA Sky	Virtual	March 2021
9th International Fermi Symposium	Virtual	April 2021

Publications

Conference Proceedings

1. R. Ebrahim, A. W. Chen, D. Prokhorov, K. Thorat, G. I. G. Józsa, and P. Serra, "Multi-wavelength study of large-scale outflows from the Circinus galaxy," in *The Proceedings of SAIP2019* (M. Chithambo, ed.), 64th Annual Conference of the South African Institute of Physics, pp. 179–184, Oct. 2020.

   Ebrahim - 70% (conception of the project, conducted the spatial analysis of the MeerKAT observations of Circinus, wrote the manuscript)

   Prokhorov & Chen - 20% (supervisors, the conception of the project, assisted with the spatial analysis of the MeerKAT observations of Circinus and its interpretations, reviewed the manuscript)

   Thorat, Józsa, & Serra - 10% (collaborators, reduced MeerKAT images, verified interpretations of the spatial analysis of the MeerKAT observations of Circinus, reviewed the manuscript)

2. R. Ebrahim, A. W. Chen, D. Prokhorov, K. Thorat, G. I. G. Józsa, and P. Serra, "Multi-wavelength study of large-scale outflows from the Circinus galaxy," in *The 7th Annual Conference on High Energy Astrophysics in Southern Africa*, p. E18, Dec. 2020.

   Ebrahim - 70% (conception of the project, developed the broadband lobe emission model, wrote the manuscript)

   Prokhorov & Chen - 20% (supervisors, the conception of the project, assisted with the development of the broadband lobe emission model and its interpretations, reviewed the manuscript)

   Thorat, Józsa, & Serra - 10% (collaborators, reduced MeerKAT images, verified interpretations of the broadband lobe emission model, reviewed the manuscript)

Contents

Declaration i

Abstract ii

Dedication iii

Acknowledgements iv

Presentations v

Publications vi

List of Figures xii

List of Tables xviii

List of Symbols xx

Nomenclature xxi

1 Introduction 1

1.1 Motivation 1

1.2 Aims 3

1.3 Outline 4

2 Literature Review and Theoretical Background 5

2.1 Seyfert galaxies 5

2.2 Starburst galaxies 7

2.3 Radio lobes 7

2.3.1 Emission processes 8

2.4 Circinus galaxy 10

2.4.1 Discovery 10

2.4.2 Classification 11

2.4.3 Structures 11

2.4.4 Starburst properties 16

2.4.5 Seyfert properties 19

2.4.6 Spectral energy distribution 20

2.5 Fermi bubbles 20

2.5.1 GeV emission 20

2.5.2 Radio & X-ray emission 21

2.5.3 Origin of emission 24

2.5.4 Fermi bubbles and Circinus' lobes 26

2.6 SN1996cr 26

2.6.1 Radio emission 28

2.6.2 GeV emission 28

2.7 Radio interferometry 29

2.8 *Fermi*-LAT 32

2.8.1 Instrument 32

2.8.2 Data products and analysis 33

2.8.3 GeV emission of Circinus with *Fermi*-LAT 34

3 Methodology **36**

3.1 Radio data 36

3.1.1 Flux calculations 37

3.1.2 Beam convolution 40

3.1.3 Spectral analysis 42

3.1.4 RMS computation 43

3.2 *Fermi*-LAT data 45

3.2.1 Likelihood analysis 45

3.2.2 Approach 48

3.3 Broadband emission modelling 48

3.3.1 Input parameters 49

3.3.2 Broadband emission data 52

3.3.3 Sensitivity curves for γ-ray observations 53

3.3.4 Case 1 53

3.3.5 Case 2 54

3.3.6 NGC 1068 57

3.4 Origin of the emission from the shocked region 58

3.4.1 Width of the shocked region 59

3.5 Multi-wavelength analysis of SN1996cr 60

3.5.1 Modelling the radio light curve 60

3.5.2 Modelling the γ-ray light curve 62

4 Results **65**

4.1 Results of MeerKAT observations 65

4.1.1 Spatial analysis 65

4.1.2 RMS results 67

4.1.3 Flux results 68

4.1.4 Spectral analysis 70

4.2 *Fermi*-LAT likelihood analysis - 10 years 73

4.3 Broadband emission modelling 75

4.3.1 Case 1 75

4.3.2 Case 2 79

4.3.3 NGC 1068 82

4.4 Origin of the emission from the shocked region 83

4.4.1 Synchrotron cooling timescale approach 83

4.4.2 Hydrodynamical approach 85

4.5 Multi-wavelength analysis of SN1996cr 87

4.5.1 Modelling the radio light curve 87

4.5.2 Modelling the γ-ray light curve 94

4.6 Discussion of results 96

4.6.1 Superiority of MeerKAT images. 96

4.6.2 Comparison to the Fermi bubbles 97

4.6.3 Towards understanding the origin of the lobe emission 97

4.6.4 Interpretation of the GeV emission of Circinus 99

5 Conclusion **105**

5.1 Summary of results 105

5.2 Future work 107

List of Figures

2.1 Radio-loud AGN model proposed by Urry and Padovani (1995). . . . 6

2.2 4860 MHz Very Large Array (VLA) image of FRII galaxy 3C98 with well defined edge-brightened lobes (Leahy et al., 2013). 8

2.3 608 MHz Westerbork Synthesis Radio Telescope (WSRT) image of FRI galaxy 3C31 with a bright core region (Leahy et al., 2013). . . . 8

2.4 Standard supersonic jet model (Worrall, 2004). 9

2.5 Starburst-driven superwind model from numerical simulations of M82 (Tomisaka and Ikeuchi, 1988) taken from Heckman et al. (1990). . . 10

2.6 [O III] emission image of Circinus from SUSI showing the ionisation cone (Marconi et al., 1994). 13

2.7 Hα+[N II] emission image of Circinus from SUSI showing the partial starburst ring (Marconi et al., 1994). 13

2.8 Orientation and direction of the molecular ring-outflow model (Curran et al., 1999). 14

2.9 Grey scale intensity image of the molecular ring-outflow model (1 arcsec $\sim$ 20 pc) (Curran et al., 1999). 14

2.10 Proposed geometry of Circinus from ATCA observations (Elmouttie et al., 1998a). 14

2.11 ATCA 3 cm radio map with a 5×5 arcsec^2 beam (Elmouttie et al., 1998a). 15

2.12 ATCA 6 cm radio map with a 1.4×1.4 arcsec^2 beam (Elmouttie et al., 1998a). 15

2.13 ATCA 13 cm radio map with a 12×11 arcsec^2 beam (Elmouttie et al., 1998a). 15

2.14 0.4-5 keV Chandra image of Circinus with 13 cm ATCA radio contours (Mingo et al., 2012). 16

2.15 Spitzer image of Circinus using three combined IR bands (For et al., 2012). 17

2.16 Global Kennicutt-Schmidt law (Kennicutt, 1998) for a sample of nearby galaxies (For et al., 2012). 18

2.17 Broadband SED of Circinus by Hayashida et al. (2013): Blue curves = modeled synchrotron and IC emission of the lobes and plumes. Grey curves = thermal components of the ISRF, due to emission from the galactic disk (starlight and dust emission), taken from GALPROP models for the Milky Way at the distance of Circinus. Black open squares = the total 'lobes + plumes' radio fluxes. Black filled circles = the total (integrated) fluxes from various catalogs and instruments. Red curves = modeled emission of the accretion disk and the disk coronae. The thick grey dotted line = the γ-ray spectrum of a star-forming system. 21

2.18 Template of the Fermi bubbles and the enhanced GeV emission cocoon (Ackermann et al., 2014) compiled by Hallmann (2015). 22

2.19 2.3 GHz S-PASS image of the Fermi bubbles by Carretti et al. (2013) with the radio lobes shown as the thick dashed lines and the γ-ray bubbles shown as the thin dashed lines. 22

2.20 ROSAT X-Ray image (Bland-Hawthorn and Cohen, 2003) superimposed on the γ-ray map of the Fermi bubbles (Ackermann et al., 2014) compiled by J.B. Hawthorn. 23

2.21 Proposed structure of the Fermi bubbles alongside ROSAT X-ray and WMAP observations (Su et al., 2010). 23

2.22 *Fermi*-LAT 10-500 GeV map of the Fermi bubbles (Ackermann et al., 2014) with the overlaid black line showing the filaments of Loop I from WMAP/Planck polarised intensity maps which trace the edges of the bubbles, compiled by Dickinson (2018). 24

2.23 Extent of the e-ROSITA bubbles (yellow) compared to the Fermi bubbles (purple) (Predehl et al., 2020). 25

2.24 a) γ-ray vs. total IR luminosity and b) γ-ray vs. 1.4 GHz radio luminosity for a sample of starburst and Seyfert galaxies (Hayashida et al., 2013). 26

2.25 Basic setup demonstrating the interaction between a SN, its shocks and the surrounding medium (Bauer et al., 2008). 27

2.26 Simple two-dish interferometer setup taken from Thompson (1989). . 30

2.27 Position vectors for extended sources in a two-dish interferometer setup taken from Thompson (1989). 30

3.1 Mingo et al. (2012) template of lobes showing the truncation line used in black. 39

3.2 Application of Mingo et al. (2012) lobes template to the 1030 GHz MeerKAT radio map showing the hotspots (yellow), lobes (orange) and shells (red) for each lobe. 39

3.3 1375 MHz MeerKAT radio image before beam correction. The image RMS is 51.12 μJy/beam and the beam is shown on the bottom left. 41

3.4 1375 MHz MeerKAT radio image after beam correction and the beam is shown on the bottom left. 41

3.5 1030 MHz MeerKAT radio image. The image RMS is 92.24 μJy/beam and the 1020 MHz beam is shown on the bottom left. 41

3.6 Histogram equalisation scaled 1375 MHz radio map with RMS regions outlined. 44

3.7 Square-root scaled 1375 MHz radio map with RMS regions outlined. 44

3.8 Broadband SED of the Fermi bubbles by Kataoka et al. (2018). . . . 51

3.9 CTA-South differential flux sensitivity curves (CTA Consortium and Observatory, a). 53

3.10 *Fermi*-LAT differential flux sensitivity curves (Maldera et al., 2019). 54

3.11 Ratio between the γ-ray luminosities (0.1-100 GeV) and total IR luminosities (8-1000 μm) for a sample of Seyferts and star-forming galaxies detected by *Fermi*-LAT (Tang et al., 2014). 55

3.12 SN1996cr elliptical flux and annulus background regions outlined in the 1375±74.5 MHz MeerKAT radio map. The beam FWHM is shown in the bottom left of the image by the filled white circle. The image RMS is 9.03 μJy/beam. The contour levels are 0.0001, 0.0038, 0.0151, 0.0338, 0.06 μJy/beam. 61

4.1 1.375 GHz MeerKAT radio map of Circinus at a 149 MHz bandwidth with a 7.6×4.4 arcsec^2 beam (shown in the bottom left of the image) obtained using 60 antennas. The map is in units of Jy/beam with a scale of 1 px$\sim$1.3 arcsec. The image RMS is 9.03 μJy/beam. The contour levels are 0.0001, 0.0017, 0.0063, 0.1411, 0.0250 μJy/beam. . 66

4.2 1.499 GHz ATCA radio contour map with a 20×19 arcsec^2 spatial resolution (Elmouttie et al., 1998a). 67

4.3 1.499 GHz ATCA radio contour map with a 6.0×5.4 arcsec^2 spatial resolution (Elmouttie et al., 1998a). 67

4.4 1.375 GHz MeerKAT radio map of Circinus with edge-brigthened regions outlined (white). The image RMS is 9.03 μJy/beam with a 7.6×4.4 arcsec^2 beam (shown in the bottom left of the image). The contour levels are 0.00041, 0.00049, 0.00074, 0.0012, 0.0017 μJy/beam. 68

4.5 1.375 GHz MeerKAT radio map of Circinus with plumes outlined (white). The image RMS is 9.03 μJy/beam with a 7.6×4.4 arcsec^2 beam (shown in the bottom left of the image). The contour levels are 0.00056, 0.00059, 0.00075, 0.0017, 0.0068 μJy/beam. 69

4.6 Two-point spectral index map of Circinus using the 1020 MHz and smoothed 1380 MHz MeerKAT data with a 2D Gaussian convolution overlaid with 1020 MHz MeerKAT radio intensity contours (0.0001, 0.0037, 0.0050, 0.0072, 0.0090 μJy/beam).The image RMS is 43.62 μJy/beam. 71

4.7 Two-point spectral index map of Circinus using the 1020 MHz and smoothed 1380 MHz MeerKAT data overlaid with 1020 MHz MeerKAT radio intensity contours (0.0001, 0.0037, 0.0050, 0.0072, 0.0090 μJy/beam).The image RMS is 43.62 μJy/beam. 72

4.8 Case 1 SED model (green curve) compared with Hayashida et al. (2013) (red curve). 76

4.9 SED model with γ_{break} varied and B=3.5 μG & N=1.5$\times10^{-10}$ cm^{-3}. 77

4.10 5σ H.E.S.S. detection time as a function of γ_{break}. 78

4.11 SED model (B=3.5 μG, γ_{break}=7.0$\times10^{6}$ & N=1.5$\times10^{-10}$ cm^{-3}) of the VHE flux with a power-law fit (red curve) between 0.3-3.0 TeV. . 78

4.12 Blackbody spectrum fit for the high-temperature radiation field. . . 79

4.13 Blackbody spectrum fit for the low-temperature radiation field. . . . 79

4.14 SED of the case 2 model which includes the CMB and ISRF seed photons for inverse Compton emission. 80

4.15 Case 2 power-law fit in the 0.2-5.0 TeV range. 81

4.16 Case 2 SED model for the NGC 1068 lobes. 83

4.17 NGC 1068 lobes case 2 power-law fit in the 0.25-5.0 TeV range. . . 84

4.18 1.375 GHz MeerKAT radio map of Circinus at a 149 MHz bandwidth showing the width of the northern shell (white box) compared to the expected width for a strong shock (green line). The image RMS is 9.03 μJy/beam with a 7.6$\times$4.4 arcsec^2 beam (shown in the bottom left of the image). 87

4.19 SN1996cr radio flux model 1 with χ^2 fit for ATCA data with four free parameters. 89

4.20 SN1996cr radio flux model 1 with least squares fit for ATCA data with four free parameters. 89

4.21 SN1996cr radio flux model 1 with χ^2 fit for ATCA data with two free parameters. 89

4.22 SN1996cr radio flux model 1 with least squares fit for ATCA data with two free parameters. 89

4.23 SN1996cr radio flux model 1 with χ^2 fit for ATCA+MeerKAT data with four free parameters. 90

4.24 SN1996cr radio flux model 1 with least squares fit for ATCA+MeerKAT data with four free parameters. 90

4.25 Behaviour of $K1$ and $K2$ in the SN1996cr MFC radio flux model. . . 91

4.26 Behaviour of m and p in the SN1996cr MFC radio flux model. 92

4.27 Behaviour of $K1$ and $K2$ in the SN1996cr AFC radio flux model. . . 92

4.28 Behaviour of m and p in the SN1996cr AFC radio flux model. 93

4.29 GeV light curve of Circinus above 1 GeV fitted with two models. . . 95

4.30 1.499 GHz ATCA radio map of Circinus with a 20.1×18.6 arcsec^2 beam [Image scale: 1 px $\sim$ 2.0 arcsec] (Mingo et al., 2012). 96

4.31 1.499 GHz - 5.000 GHz ATCA spectral index map with 5.000 GHz ATCA radio emission contours (Elmouttie et al., 1998a). 98

4.32 0.1-100 GeV γ-ray to 8-1000μm IR luminosity ratio for a sample of galaxies including Circinus (Guo et al., 2019). 100

List of Tables

2.1 Properties of the *Fermi*-LAT instrument (Abdollahi et al., 2020). . 32

3.1 MeerKAT radio maps used in the analysis. 38

3.2 Summary of all nine approaches of the binned likelihood analysis over the full ten years. 48

3.3 Fixed parameters of the broken power-law electron distribution used in the SED model of the lobes of Circinus compared with Hayashida et al. (2013) 51

3.4 Derivation of $a(p, m)$ & $b(p, m)$ using the time dependencies by Chevalier (1996). 62

4.1 RMS and MAD values for the five regions in the WSClean 1375 MHz radio map. 68

4.2 RMS values for the MeerKAT radio maps. 69

4.3 MeerKAT flux density measurements at different central frequencies and bandwidths for the lobe structure of Circinus. 70

4.4 Quantities required to compute the flux errors of each region demonstrated for the 1375±74.5 MHz map. 70

4.5 Higher frequency MeerKAT flux measurements for the lobe structure of Circinus compared to 20cm (1 499 MHz) ATCA observations by Mingo et al. (2012). 70

4.6 MeerKAT spectral index measurements for the lobe structure of Circinus compared to the ATCA spectral indices by Mingo et al. (2012). . 71

4.7 Summary of results from all nine approaches of the binned likelihood analysis over the full ten years. 73

4.8 v9 binned likelihood output for Circinus. 74

4.9 Comparison of input parameters used in the broadband emission modelling of the lobes of Circinus and the Fermi bubbles. 75

4.10 Best-fit temperature and energy density for the ISRF components for the lobes of the Circinus and the solar system. 79

4.11 Radio flux data points used in the modelling of the radio light curve of SN1996cr. 88

4.12 Results for models 1-4 with $K1$, $K2$, p and m free for the ATCA data. 88

4.13 Results for models 1-4 with p and m fixed for the ATCA data. . . . 88

4.14 Results for models 1 with $K1$, $K2$, p and m free for the ATCA data only and the ATCA + MeerKAT data. 90

4.15 Summary of SN1996cr radio light curve modelling results. 91

4.16 GeV flux of Circinus and corresponding TS value for the final two-year binned likelihood analysis. 94

4.17 *Fermi*-LAT γ-ray luminosity in the 0.1-100.0 GeV range for different photon indices. 101

4.18 H.E.S.S. integral flux upper limits compared to the modeled VHE predictions. 103

4.19 Predicted VHE flux of Circinus detectable by H.E.S.S. based on the GeV flux decline model of SN1996cr. 103

List of Symbols

c	Speed of light in a vacuum inertial frame
$M_\odot$	Mass of the sun
λ	Wavelength
ν	Frequency
γ	Lorrentz factor
FWHM	Full width at half maximum

Nomenclature

AGN	Active Galactic Nuclei
ATCA	Australia Telescope Compact Array
BLR	Broad Line Region
CARACal	Containerized Automated Radio Astronomy Calibration
CLR	Coronal Line Region
CMB	Cosmic Microwave Background
CSM	Circumstellar Medium
CTA	Cherenkov Telescope Array
Dec.	Declination
FIR	Far Infrared
FITS	Flexible Image Transport System
FRI	Fanaroff-Riley I
FRII	Fanaroff-Riley II
FSSC	*Fermi* Science Support Centre
H.E.S.S.	High Energy Stereoscopic System
IC	Inverse Compton
IR	Infrared
IRAS	Infrared Astronomical Satellite
ISM	Interstellar Medium
ISRF	Interstellar Radiation Field
LAT	Large Area Telescope
MAD	Mean Absolute Deviation
MET	Mission Elapsed Time
NIR	Near Infrared
NLR	Narrow Line Region
NPS	North Polar Spur
PSF	Point Spread Function
R.A.	Right Ascension
RASS	ROSAT All-Sky Survey
RoI	Region of Interest
RMS	Root Mean Square
SARAO	South African Radio Astronomy Observatory
SED	Spectral Energy Distribution
SFR	Star Formation Rate
SNR	Supernova Remnant
S-PASS	S-band Polarisation All Sky Survey

SSC	Synchrotron Self-Compton
UV	Ultra-violet
VHE	Very High Energy
VLA	Very Large Array
VLBI	Very Long Baseline Interferometry
WMAP	Wilkinson Microwave Anisotropy Probe
WSRT	Westerbork Synthesis Radio Telescope
XML	Extensible Markup Language

Chapter 1

Introduction

1.1 Motivation

Galaxies with strong radio sources were first identified in the 1950s. The development of radio interferometers provided a new way to probe these radio galaxies and study their structures such as jets and radio lobes. The MeerKAT array of radio telescopes (Jonas and MeerKAT Team, 2016) is capable of imaging low radio brightness extended emission at improved resolutions and sensitivity compared to previous interferometers. The Circinus galaxy is one such case of a low-power radio galaxy observable with MeerKAT.

Circinus is a spiral galaxy only 4 Mpc away (Freeman et al., 1977). This galaxy is interesting as it possesses characteristics of both Seyfert and starburst galaxies. A key feature of Circinus is its kpc-scale radio lobe outflows. There are two models commonly used to describe the origin of the radio lobe emission - an Active galactic nucleus (AGN) jet-driven model [e.g., (Worrall, 2004)] and a starburst wind-driven model (Heckman et al., 1990; Tomisaka and Ikeuchi, 1988). The composite nature of Circinus means that studying its lobes in greater detail could enable a better understanding of these lobe emission models.

This type of kpc-scale radio emission has been observed in the Milky Way in the form of the Fermi bubbles. They were first discovered in 2010 from γ-ray observations with the *Fermi*-LAT telescope (Su et al., 2010), but later detected at other frequencies including X-ray (Snowden et al., 1997; Predehl et al., 2020) and radio (Carretti et al., 2013). These bubbles are eight times larger than the Circinus lobes but, like Circinus, the origin of the bubble emission is still not clear. To better understand

the origins of the Fermi bubbles, observations of other lobed galaxies are important (see NGC 1068 [e.g., Young et al. (2001)], Centaurus A [e.g.,Kraft et al. (2003)], NGC 3079 [e.g., Irwin and Saikia (2003)] and M82 [e.g.,Griffiths et al. (2000)]. By understanding the lobe emission in galaxies such as Circinus, we can develop a better understanding of the origins of the Fermi bubble emission.

Radio lobes are rarely detected in spiral galaxies, such as Circinus, but mostly in elliptical ones. The dense interstellar medium (ISM) in spiral galaxies hampers the easy movement of the jet through its surrounding medium, which is necessary for the formation of radio lobes. Circinus, the Milky Way, NGC 1068, and NGC 3079 are all examples of spiral galaxies with large outflows. Studying these galaxies presents the opportunity to study the interaction between radio lobed spiral galaxies and their environments.

Circinus is one of the closest starburst galaxies to us along with NGC 253 (Kaneda et al., 2010), NGC 3079 (Irwin and Saikia, 2003) and M82 (Griffiths et al., 2000). These galaxies are excellent candidates to study the star formation feedback mechanism and its interaction with the ISM. As a consequence of its starburst nature, Circinus hosts one of the brightest Type II supernova in the radio and X-ray, SN1996cr, which exploded in 1996 (Bauer, 2007), also detectable by MeerKAT as a point source.

In summary, Circinus is the galaxy of interest for this study as it is the closest galaxy which allows us to probe lobe emission models, a better understanding of the Fermi bubbles, the interaction between radio lobes and the ISM in spiral galaxies and the study of star formation feedback mechanisms.

Circinus was discovered in the optical band but has also been observed at radio, X-ray and γ-ray frequencies. Australia Telescope Compact Array (ATCA) studies of the radio emission of Circinus [e.g., Elmouttie et al. (1998a); Mingo et al. (2012)] have enabled observations of the extended lobe structures resolving the lobes into cylindrical plumes of brightened emission surrounded by brightened edges. MeerKAT observations allow us to observe these lobes through deeper and higher resolution images relative to ATCA, allowing us access to potentially new information about the lobes which may have eluded previous efforts. This includes a spatial analysis to identify new structures and a spectral index analysis to identify regions of electron ageing and particle acceleration and detect the presence of hotspots.

GeV studies of Circinus have also been carried out with *Fermi*-LAT [e.g.,Hayashida et al. (2013), Guo et al. (2019)]. The significance of this emission is that if variability is detected, we can confirm the presence of an AGN core. The GeV emission can also be used to probe the starburst nature of Circinus by testing its compatibility

with the empirical relation between GeV and IR luminosity for star-forming galaxies (Ackermann et al., 2012). Initial analysis of the *Fermi*-LAT observations (Hayashida et al., 2013) using the first four years of observations and the early two-year *Fermi* source catalogue found no variability and a high luminosity that was inconsistent with the starburst relation. More recently, marginal variability and compatibility with the starburst relation (due to a lower observed luminosity) has been claimed (Guo et al., 2019) using ten years of data and the eight-year source catalog (4FGL). In this thesis, we reanalyse the ten-year data set of *Fermi*-LAT observations using the most recent source catalog 4FGL-DR2 to search for variability and to study the origin of this emission.

A leptonic broadband emission model of the Circinus lobes has been developed by Hayashida et al. (2013) using archival data across various frequencies. Their model matched well with the radio observations, but the detected GeV emission exceeded the model's predictions. The renalysed GeV emission which is expected to be lower whilst using the 4FGL-DR2 can be tested against the broadband emission model. This model can also be used to make predictions about the very high energy (VHE) emission we expect to see with other γ-ray telescopes like the upcoming Cherenkov Telescope Array (CTA).

1.2 Aims

This dissertation aims to study the physical nature of the radio lobes in Circinus. This will be achieved through:

1. Observing the kpc scale radio lobes with MeerKAT.
2. Conducting a multi-wavelength analysis of the lobes through the MeerKAT radio observations and *Fermi*-LAT γ-ray observations to investigate the observational properties of the lobes and study their formation.
3. Comparing the Circinus lobes to the Fermi bubbles to determine any similarities.
4. Studying the multi-wavelength emission of SN1996cr located in the Circinus galaxy.

1.3 Outline

Chapter 2 of this dissertation covers a literature review of the topics required in this project, including background on Seyfert and starburst galaxies, properties of the Circinus galaxy and its observations across the electromagnetic spectrum, as well as the instruments used to perform the observations in this analysis. In Chapter 3, we describe the methods used and the approaches taken to analyse the MeerKAT and *Fermi*-LAT data in the context of the radio lobes, to generate a broadband lobe emission model, to study the origin of the emission and to study the flux decline of SN1996cr. Chapter 4 contains the results of this project followed by a discussion on the interpretation of the results, and Chapter 5 presents the final conclusions and a brief discussion on future work.

Chapter 2

Literature Review and Theoretical Background

2.1 Seyfert galaxies

AGNs are galaxies with bright, variable nuclei and are powered by a central supermassive black hole. They are highly luminous across the electromagnetic spectrum and their emission is dominated by non-thermal processes. Figure 2.1 (Urry and Padovani, 1995) shows the general structure of AGNs. These galaxies have dense and active cores hosting a central supermassive blackhole which is surrounded by an accretion disk and fast-moving clouds associated with broad emission lines (Padovani, 1997). A torus structure consisting of dust and gas may also be present. For a transverse viewing angle, the dusty torus can obscure the nucleus (and the broad emission lines). Further away from the torus are clouds emitting narrow emission lines. AGNs can also have relativistic jets which are collimated structures created by the material surrounding the black hole which is flung out almost perpendicularly to the disk at relativistic speeds.

Observations of AGNs show that they have rapidly varying fluxes on relatively short timescales across the electromagnetic spectrum. For variability to be detected on these timescales, the size of the variable source needs to be small. This is implied from simple causality arguments in which the emitting region needs to be causally connected and to vary coherently on short timescales. This sets a constraint on the size D of the source since $D \leq ct$, where c is the speed of light traveling across the source with a size D within a time t. It should be noted that Doppler boosting, occurring in relativistic jets, shortens the observed timescale relative to the co-

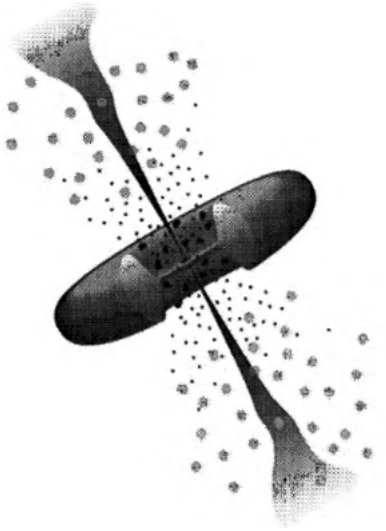

Figure 2.1: Radio-loud AGN model proposed by Urry and Padovani (1995).

moving frame timescale (Protheroe, 2002).

AGNs are divided into two classes: radio-loud and radio-quiet AGNs. They can be characterised into these types based on their radio-loudness parameter which is the ratio of the 5 GHz radio flux density to the 4400 Å B-band optical flux density (Kellermann et al., 1989) with a value of 10 as the lower limit for radio-loud AGNs.

The AGN of interest for this project are Seyfert galaxies which are typically radio-quiet. However, there are reports of radio-loud Seyferts such as Mrk 6 (radio-loudness parameter = 23) (Kharb et al., 2014). They are usually low luminosity galaxies and thus observed close-by (Urry and Padovani, 1995). Seyferts can also feature small-scale jets and other radio sources such as lobes and often these structures are misaligned (Kharb et al., 2014).

The spectra of Seyfert galaxies are characteristic of photoionisation interactions between the accretion disk and the circumnuclear gas (Marconi et al., 1994). Ultraviolet (UV) continuum radiation is emitted by the accretion disk onto the blackhole. This radiation ionises and heats up the surrounding gas in the broad-line region (BLR) and narrow-line region (NLR) to produce emission lines (Aldrovandi, 1981). Seyfert 1 and Seyfert 2 galaxies are distinguished by this emission spectra. Seyfert 2 galaxies, like Circinus, present narrow emission lines only since the BLR is obstructed by a dusty molecular torus. Seyfert 1 galaxies on the other hand feature both broad and narrow emission lines as both regions are visible.

2.2 Starburst galaxies

Starburst galaxies show high star-formation rates (SFR) on the order of 10-100 $M\odot$/year (Muxlow et al., 2006). These galaxies are also associated with short starburst lifetimes ($\leq 10^9$ years (Kennicutt and Evans, 2012)) relative to the age of the galaxy. This is because the large SFR depletes the available gas responsible for star formation on a timescale faster than the age of the galaxy.

The radio emission of starburst galaxies includes thermal and non-thermal emission. The thermal emission originates from HII regions in which UV photons from the stars ionise the hydrogen gas in the ISM to produce free-free emission between the thermal electrons present in the ISM. The non-thermal emission comes from the interaction between electrons, accelerated to relativistic speeds by supernova remnants (SNR) shocks, and magnetic fields to produce synchrotron radiation.

Starburst galaxies can be studied through multi-wavelength observations. The total infrared (IR) luminosity of a galaxy is usually used as a probe for its SFR (Elmouttie et al., 1997). The UV photons, produced by hot young stars, are absorbed by the dust grains which in turn emit in the ISM and emit strongly in the IR bands. The radio emission observed in star-forming galaxies is dominated by the synchrotron radiation. Starburst activity can also be observed in the form of radio recombination lines from ionisation of the surrounding gas (Roy et al., 2008). γ-ray observations of starburst activity can result from cosmic-rays that are accelerated by SNRs. This emission can come from neutral pion decay due to inelastic collisions between cosmic-ray nuclei and ambient gas or inverse Compton (IC) scattering between cosmic-ray electrons and photons in the ISM.

2.3 Radio lobes

Radio lobes are bubbles of non-thermal radio emission that usually originate from the center of a galaxy and extend outwards. They are kpc scale structures that can be larger than the host galaxy itself.

Radio continuum emission in the lobes consists of a compact and diffuse component. The compact emission usually corresponds to thermal bremsstrahlung HII regions, and the diffuse emission is associated with non-thermal synchrotron radiation (Elmouttie et al., 1998a).

2.3.1 Emission processes

AGN jet model

The type of jet present in an AGN will influence the type of radio lobe that is observed. Galaxies with high powered collimated jets have more defined radio lobes (Alloin et al., 2006) classified as Fanaroff-Riley II (FRII) galaxies (Fanaroff and Riley, 1974) with the brightest features located away from the core. On the contrary, FRI galaxies (Fanaroff and Riley, 1974) have low-powered, but bright and turbulent jets that cause significant disruptions to the surrounding material. In FRI galaxies the surface brightness is highest at the core and then fades off further away (Alloin et al., 2006). Hence the radio lobe structures do not typically dominate over the jets. Figures 2.2 and 2.3 present a typical FRII and FRI galaxy respectively.

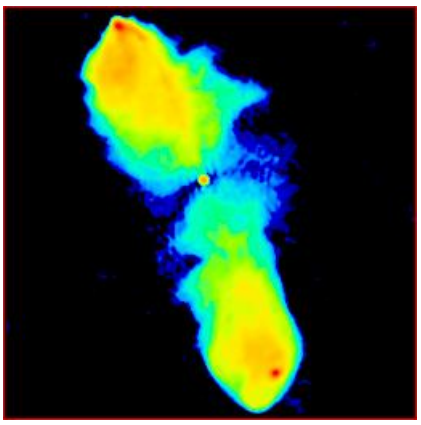

Figure 2.2: 4860 MHz Very Large Array (VLA) image of FRII galaxy 3C98 with well defined edge-brightened lobes (Leahy et al., 2013).

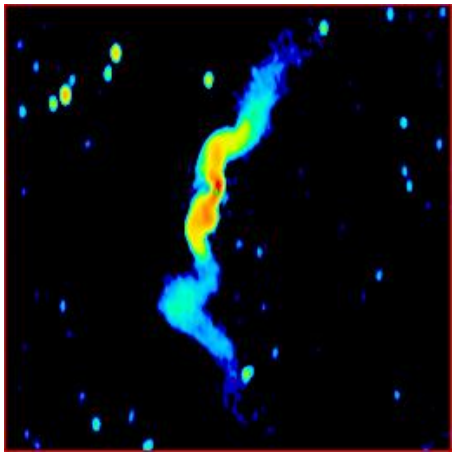

Figure 2.3: 608 MHz Westerbork Synthesis Radio Telescope (WSRT) image of FRI galaxy 3C31 with a bright core region (Leahy et al., 2013).

Figure 2.4 (Worrall, 2004) shows the standard emission model for a FRII AGN with a supersonic jet. The jet moves at much higher speeds relative to the surrounding medium. As the medium tries to slow the jet down, shock waves form. This jet structure terminates at the beam head creating a bright and compact region which is observed as a radio hotspot (Alloin et al., 2006). The fluid from the jet then passes through a strong shock to create a contact discontinuity and the region inside this boundary forms the radio lobe emission (Alloin et al., 2006). With sufficient energy and momentum, the flow can then drive a bow shock through the ambient gas to create a cocoon of shocked gas that is usually detected in the X-ray (Alloin et al., 2006), but can be detected at other wavelengths.

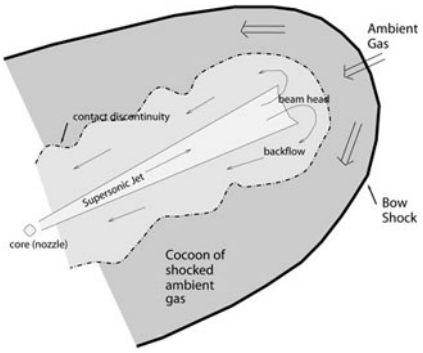

Figure 2.4: Standard supersonic jet model (Worrall, 2004).

Radio galaxies that feature large jets can pump abundant amounts of energy into the ISM. As a result of this AGN feedback mechanism, it is often found that the SFR in these galaxies is much lower than in normal galaxies (Singh et al., 2015). In the context of the AGN model, it is worth noting that radio lobes are more often found in elliptical AGNs (Matthews et al., 1964). These galaxies feature a low-density ISM enabling the jet structures to extend for hundreds of kpc (Singh et al., 2015). Seyfert galaxies, which are spiral, thus have a very dense ISM and smaller jets which do not extend beyond the galaxy itself. As a result, there is a lower possibility of AGN-driven lobes forming. However, Circinus is a unique case in that it is a spiral Seyfert galaxy with unusually large lobes.

Starburst driven model

The other competing model for the formation of radio lobes is the starburst driven model. In this scenario, the lobes are fueled by starburst regions containing supernova (SN) explosions and stellar winds. These explosions and winds can combine and drive shock waves as they move through the surrounding ISM to form a hot and pressurised bubble observed as the lobe (Heckman et al., 1990).

The superwind model shown in Figure 2.5 (Heckman et al., 1990) is based on numerical simulations of the starburst galaxy M82 by Tomisaka and Ikeuchi (1988). In this model, the superwind is driven by shock interactions between the ISM and hot fluid consisting of the ejecta material from supernovae (SNe) and stellar winds. For the large-scale outflow to be driven, the SN rate must be sufficiently high such that the SN and stellar wind interactions efficiently convert the kinetic energy of the ejecta fluid primarily into thermal energy, as opposed to radiation, via shocks (Heckman et al., 1990). The hot fluid escapes through a cavity (C) in the molecular disk (MD), passes through a shock, and expands as a free wind (FW). This wind is shock heated as it interacts with an internal wind shock (WS) and the shocked

wind (SW) can be observed as thermal X-ray emission. The pressure from the wind then inflates a bubble of gas that is hot and pressurised relative to the ISM. This bubble produces a shock wave that sweeps up the ambient gas and accelerates it. The shocked gas will eventually cool down to form a thin dense shell (S) when it can cool down faster than the wind is expanding. As the bubble expands, it can eventually escape the galactic halo (GH).

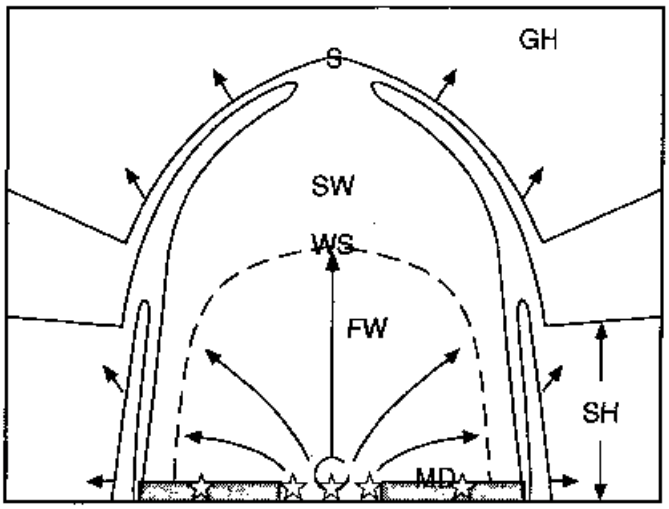

Figure 2.5: Starburst-driven superwind model from numerical simulations of M82 (Tomisaka and Ikeuchi, 1988) taken from Heckman et al. (1990).

2.4 Circinus galaxy

Circinus is a southern galaxy (R.A. $14^h13^m10^s$, Dec. -65°20′21″) located at 4±1 Mpc (Freeman et al., 1977). This distance is determined by observations of its luminosity and its mass distribution totalling around $10^{11}M_\odot$ (Freeman et al., 1977). It is inclined at $\sim 65°$ (Harnett et al., 1990) and is very close to the galactic plane at $b = -4°$.

2.4.1 Discovery

Circinus was first detected in 1972 from an atlas of nebulae in the Southern Milky Way (Lyngå and Hansson, 1972). This atlas was compiled from optical observations using the Schmidt telescope at the Mount Stromlo Observatory in Australia. It was later classified as a spiral galaxy by Freeman et al. (1977). The galaxy gets its name from its location within the Circinus constellation (Freeman et al., 1977).

Since its discovery in the optical Circinus has also been observed across the electromagnetic spectrum (radio [e.g.,Elmouttie et al. (1995, 1997, 1998a); Freeman et al. (1977); Harnett et al. (1990); Mebold et al. (1977); Gardner and Whiteoak (1982); Whiteoak and Bunton (1985); Greenhill et al. (2003)], infrared [e.g., Moorwood and Glass (1984); Bisht et al. (1990); For et al. (2012)], X-ray [e.g.,Mingo et al. (2012)] and GeV γ-ray [e.g.,Hayashida et al. (2013); Guo et al. (2019)]) in various studies.

2.4.2 Classification

Classifying this galaxy has always been a challenge. In the optical it is identified in the range of a Sb-Sd type galaxy and this is a result of significant interstellar absorption and the high star field density which limits the aperture size usually used to classify the UBV colour of galaxies (Freeman et al., 1977). In the radio Circinus is observed as a composite Seyfert/starburst galaxy for reasons that will be discussed further in this section.

2.4.3 Structures

Disk

In the optical regime, observations of Circinus reveal a diffuse disk with a diameter of $\sim$5 kpc. ATCA observations show a radio disk emission of 4.2 kpc in radius (Elmouttie et al., 1998a). There are also several star-forming regions observed along the major axis of the galaxy (Elmouttie et al., 1998a).

Nucleus

The radio emission of Circinus is dominated by its nucleus. This nucleus hosts a compact radio source with a flux of 1.5 Jy at 1400 MHz (Freeman et al., 1977). Surrounding the nucleus is a rapidly rotating cloud suggested by observations of OH absorption (Harnett et al., 1990). There is an Hα core that is coincident with the radio continuum core suggesting the presence of ionised gas surrounding the core (Elmouttie et al., 1998b).

Ionisation cone

The nuclear activity occurring within Circinus has been reported since 1990 in which radio continuum images revealed spur emission with a nuclear origin (Harnett et al., 1990). (Marconi et al., 1994) reported Circinus to be the nearest Seyfert with both a nuclear starburst ring and an ionization cone. The asymmetric ionization cone is shown in Figure 2.6. It was detected from [OIII] line emission images obtained from the SUSI camera on the New Technology Telescope at the La Silla Observatory. This provides support for the presence of an obscuring torus since the torus is known for collimating ionising radiation in the form of an ionisation cone in this case. Its one-sided nature could be a result of the disk obscuring its southern counterpart.

Elmouttie et al. (1998b) looked at the [OIII] ionisation cone and detected it in the Hα with the Anglo-Australian telescope. They found that it extends for about 400 pc and is oriented away from us. Mingo et al. (2012) observed Chandra X-ray emission from Circinus coincident with the ionisation cone that is further coincident with the base of the northern X-ray lobe. This spatial coincidence is not detected in the radio band. Their results suggest that the AGN could be responsible for the photoionisation effects causing the ionisation cone.

Starburst ring

Marconi et al. (1994) obtained an Hα image from SUSI shown in Figure 2.7 which presents a partial starburst ring of highly variable intensity encircling the nucleus at a distance of 10 arcsec (200 pc). This ring also contains several HII regions. However, they did not establish any relation between this ring and the Seyfert core. Other line emission observations (Marconi et al., 1994) indicate that this emission originates from a young starburst of $\leq 10^8$ years.

H_2O maser

Circinus is among the few observed galaxies that have a high luminosity nuclear H_2O maser (Gardner and Whiteoak, 1982). H_2O maser observations show two bright features symmetrically positioned attributed to hotspots - this effect is also observed in our Galaxy (Gardner and Whiteoak, 1982). Very long baseline interferometry (VLBI) (Greenhill et al., 2003) shows a warped accretion disk with a pc-scale outflow from its center aligned with the ionisation cone.

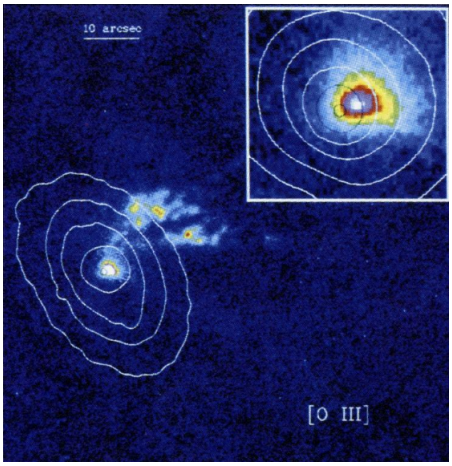

Figure 2.6: [O III] emission image of Circinus from SUSI showing the ionisation cone (Marconi et al., 1994).

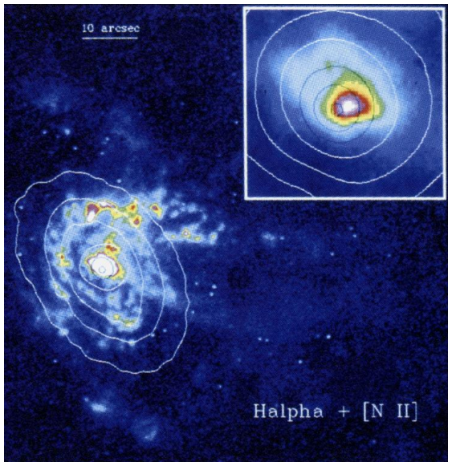

Figure 2.7: Hα+[N II] emission image of Circinus from SUSI showing the partial starburst ring (Marconi et al., 1994).

CO molecular ring

Curran et al. (1998) looked at CO transitions in Circinus and found a molecular ring and possibly a 600 pc molecular outflow associated with this ring (see Figures 2.8 and 2.9). These findings are coincident with the ionisation cone (Marconi et al., 1994). The observations also show both outflows sharing a large conical angle ($> 90°$). Curran et al. (1998) also proposed that the molecular ring's extent and orientation obscures the view of the southern counterpart to the detected ionisation cone. Davies et al. (1998) looked at the [FeII] emission usually associated with SNRs and found no significant emission in this ring. This suggests that the star-formation activity is associated with young stars implying that there are no supernovae older than 10^4 yr. Further, their observations found HII to decrease towards the ring, which indicates that star formation did not propagate from the AGN (Davies et al., 1998).

Hα observations with the Anglo-Australian telescope (Elmouttie et al., 1998b) show that this is a rotating ring inclined at $40°\pm10°$. Therefore, it is not inclined along the plane of the radio continuum disk.

Lobes

The first detailed study of the lobes of Circinus was conducted by Elmouttie et al. (1995) using ATCA observations (see Figures 2.11 - 2.13). The proposed geometry of Circinus from these images (Elmouttie et al., 1998a) can be seen in Figure 2.10. The ATCA images were able to resolve the lobes such that the hotspots within

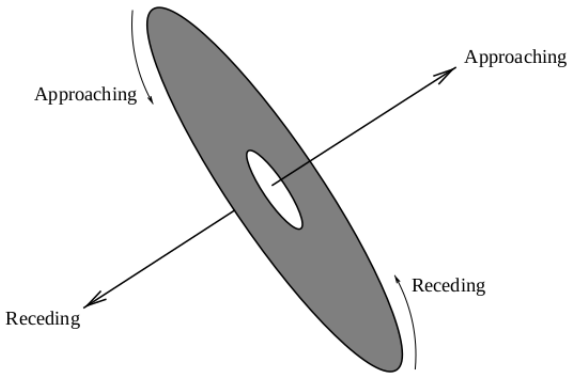

Figure 2.8: Orientation and direction of the molecular ring-outflow model (Curran et al., 1999).

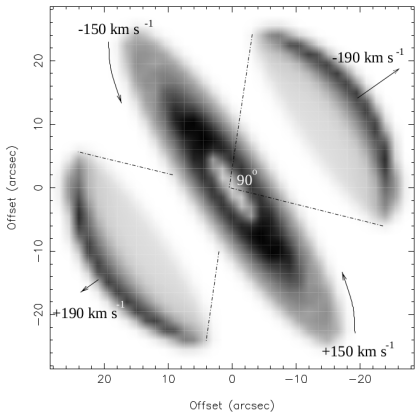

Figure 2.9: Grey scale intensity image of the molecular ring-outflow model (1 arcsec $\sim$ 20 pc) (Curran et al., 1999).

bisymmetric plumes surrounded by an edge-brightened region were observed. The cylindrical plumes extend to 1 kpc in length and 500 pc in width with magnetic fields oriented along the plume axis (Elmouttie et al., 1998a). They were the first to detect the linearly polarised nature of the lobes. The northern lobe is brighter and more polarized than its southern counterpart. The brightened emission towards the center of the southern lobe is identified as the southern plume.

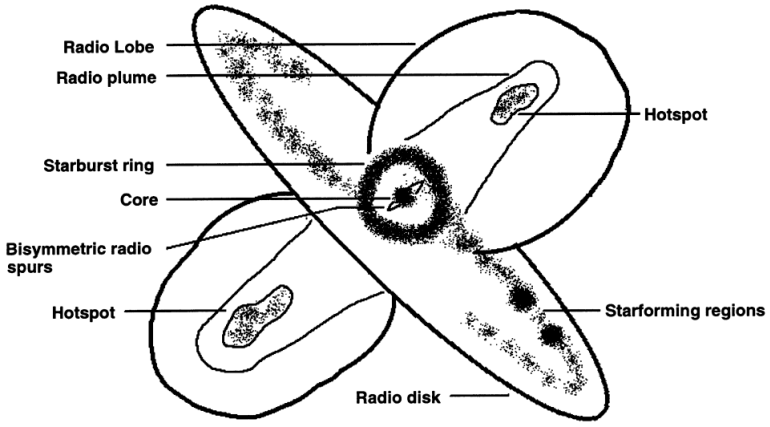

Figure 2.10: Proposed geometry of Circinus from ATCA observations (Elmouttie et al., 1998a).

They also studied a non-thermal synchrotron spectrum of these lobes. The combined presence of an ionization cone (Marconi et al., 1994) and the northern plume provided support for a nuclear outflow model (Elmouttie et al., 1995). λ=6 cm ATCA observations (see Figure 2.12) show bisymmteric spurs oriented along the plume axis and close to the core at a distance of 5 arcsec (Elmouttie et al., 1998a) providing further support for nuclear outflows.

Another prominent feature of the lobes of Circinus is its brightened edges. The

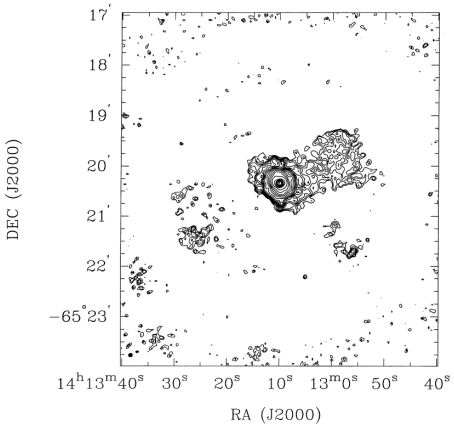

Figure 2.11: ATCA 3 cm radio map with a 5×5 arcsec^2 beam (Elmouttie et al., 1998a).

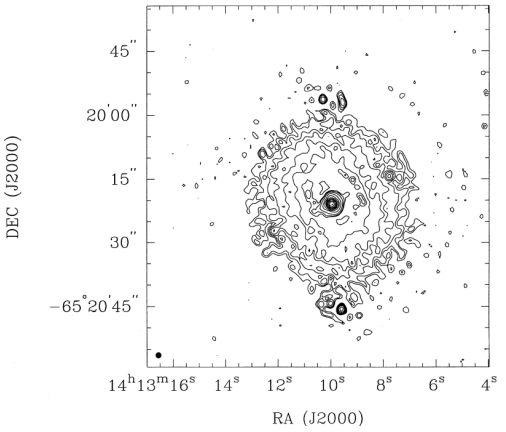

Figure 2.12: ATCA 6 cm radio map with a 1.4×1.4 arcsec^2 beam (Elmouttie et al., 1998a).

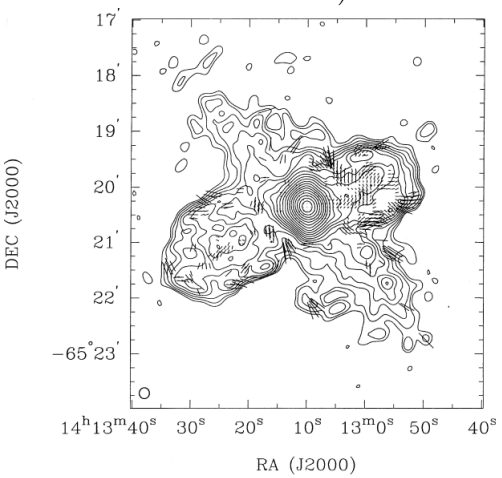

Figure 2.13: ATCA 13 cm radio map with a 12×11 arcsec^2 beam (Elmouttie et al., 1998a).

spatial coincidence between the brightened X-ray edges and radio edges were first detected by Mingo et al. (2012) from X-ray observations with Chandra shown in Figure 2.14. This structure is usually observed in shocks found in supernova remnants. Their results also show that the AGN is not likely to be the driver of the edge-brightened emission. Instead, they present a model in which the AGN photoionises the gas initially in the lobes. The ionised gas eventually transitions into a shocked gas to explain the brighter lobe and edge structure.

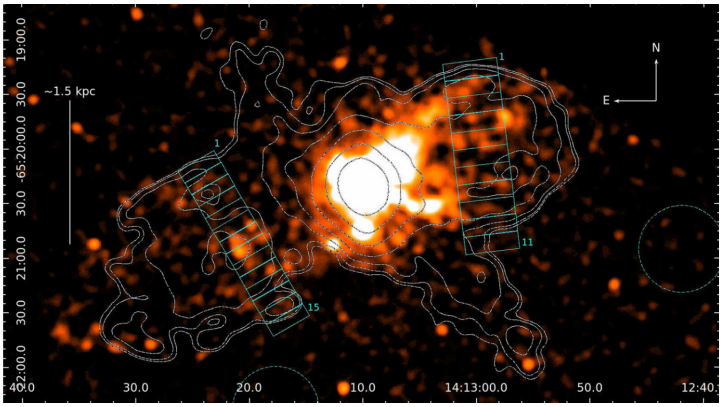

Figure 2.14: 0.4-5 keV Chandra image of Circinus with 13 cm ATCA radio contours (Mingo et al., 2012).

Jet

The extended H_2 emission associated with jet flaring activity in Circinus is weak (Davies et al., 1998) which implies that the location of the jet is restricted to the nuclear region. In addition, the coronal line emission is blue-shifted suggesting that the radio jet makes a small contribution to the outflows since the jet is not strong enough to clear a path in the coronal line region (CLR) and into the NLR (Nazarova et al., 1999).

Spectral analysis observations from ATCA show the core and star-forming regions to have a flatter spectrum. The spectrum flattens closer to the hotspots within the plumes - typical of what is observed in jets (Elmouttie et al., 1998a). There are two possible causes for this spectral flattening - thermal free-free absorption in the core or a compact core with synchrotron self-absorption present (Elmouttie et al., 1998a).

2.4.4 Starburst properties

There are some notable similarities between Circinus and other starburst galaxies like NGC 4945. Circinus and NGC 4945 are both spiral galaxies with distinct radio outflows (Harnett et al., 1990). One explanation for the radio lobes in NGC 4945 is that it results from interactions between nuclear ejecta material and the galactic disk (Harnett et al., 1990). Circinus and NGC 4945 both have starburst associated molecular rings and similar dynamical masses ($\sim 10^9 M\odot$) in its central 600 pc region (Curran et al., 2001). Also, H_2O masers are commonly associated with star-forming regions (Harnett et al., 1990) and this has been detected in both galaxies.

IR observations have shown several starburst properties of Circinus. A starburst characteristic IR excess is observed which also is found in NGC 4945 (Harnett et al., 1990). Infrared Astronomical Satellite (IRAS) observations (Moorwood and Glass, 1984) show a thermal IR distribution and absorption activity similar to what is observed in another popular starburst galaxy - M82. Figure 2.15 is a Spitzer IR image of Circinus (For et al., 2012) which shows a spiral arm and an outer and inner disk. These observations were correlated with ATCA HI maps to identify twelve star-forming regions within Circinus.

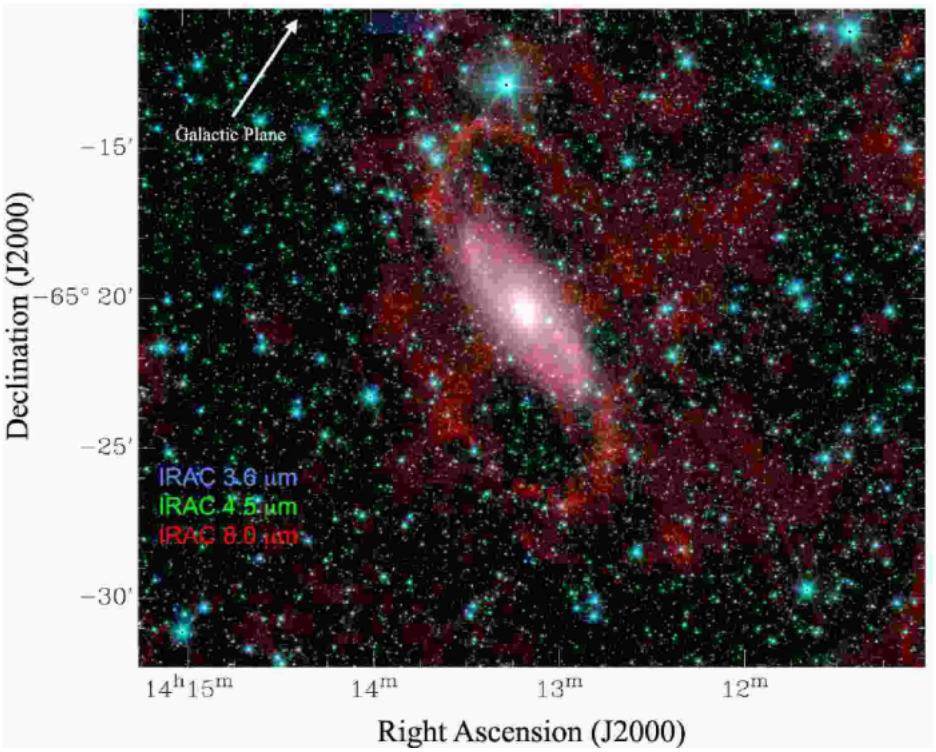

Figure 2.15: Spitzer image of Circinus using three combined IR bands (For et al., 2012).

The SFR of Circinus is also consistent with starburst galaxies. Circinus has an SFR of 2.52 $M_{\odot}\mathrm{yr}^{-1}$ which is derived from the total IR luminosity. This value is greater than the average for other spiral galaxies (Elmouttie et al., 1997). This property is also demonstrated in Figure 2.16 which shows the global Kennicutt-Schmidt law (Kennicutt, 1998) for a sample of nearby star-forming and normal galaxies (For et al., 2012). This law is a parametrised relation between the SFR and gas density in a galaxy. The SFR of Circinus lies comfortably within the regime of known starburst galaxies in this sample.

Another starburst property of Circinus is the lack of polarisation observed in the core relative to its lobes (Elmouttie et al., 1998a). This observation favours the presence of nuclear star formation since starburst activity is known to create a turbulent ISM

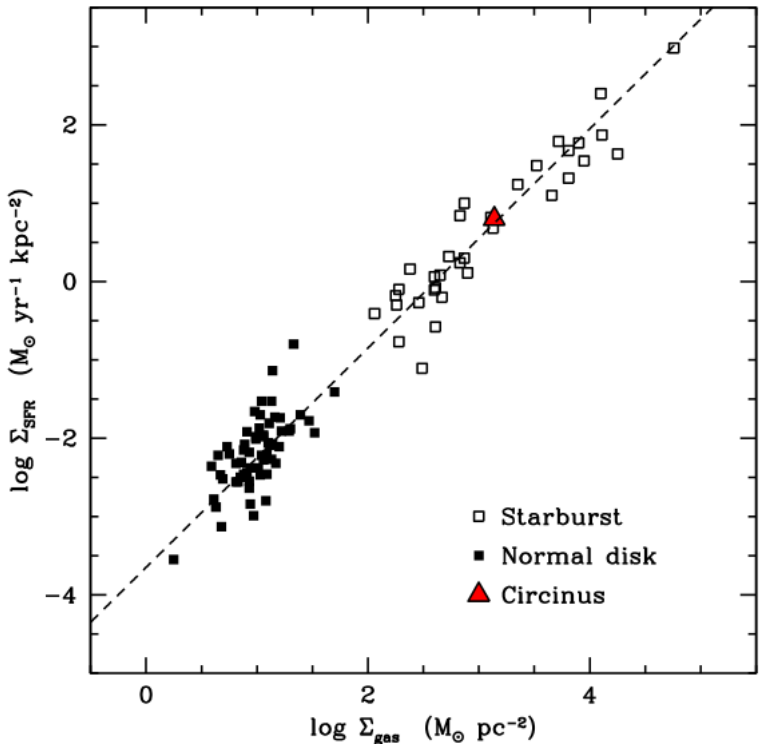

Figure 2.16: Global Kennicutt-Schmidt law (Kennicutt, 1998) for a sample of nearby galaxies (For et al., 2012).

corresponding to tangled and thus non-uniform magnetic fields.

Some of the starburst properties of Circinus can be studied in the context of the starburst wind-driven/super-bubble lobe outflow model. The age of the starburst is estimated to be 10^8 yr (Marconi et al. (1994); Elmouttie et al. (1998a)) and the age of the radio lobe assuming a pure starburst model is computed to be 10^6 yr (Elmouttie et al., 1998a) and so the starburst activity could be partially responsible for the production of the lobes.

Hα observations (Elmouttie et al., 1998b) also provide support for the starburst wind-driven model. The detected Hα ring is similar in radius to the northern plume at $\sim r = 250$ pc, and there is a geometrical alignment between the plume and ring axis, suggesting that these two structures are related. It is thus possible for the plume to be driven by the starburst activity associated with the ring.

GeV emission can also be used to probe emission models. In the starburst model, the enhanced supernovae explosions and stellar winds that result can serve as cosmic-ray acceleration sites. The cosmic-ray electrons are transported away from the galactic plane and radiate via the inverse Compton mechanism to produce the lobes observed as GeV emission.

Hayashida et al. (2013) studied four years worth of GeV emission from the *Fermi*-LAT (*Fermi*-Large Array Telescope) γ-ray telescope. A 7.3 σ excess was found, but no spatial structure was detected. They also searched for a variable Seyfert core but found no significant variability. More recently, Guo et al. (2019) studied the GeV emission from Circinus using ten years of *Fermi*-LAT data and found a drop in photon flux with time suggesting marginal variability. Section 2.8.3 reports on the *Fermi*-LAT GeV analysis of Circinus in further detail.

Guo et al. (2019) also found the flux of Circinus to be compliant with an empirical relation between the γ-ray and total IR luminosity for star-forming galaxies. They also proposed that the observed luminosity suggests that Circinus could be a proton calorimeter. In this model, the cosmic-ray protons interact with the ambient gas producing γ-ray emission from the galaxy with the γ-ray luminosity scaling linearly with the SFR. The expected luminosity of Circinus from the observed SFR in the proton calorimeter model is consistent with the *Fermi*-LAT observations.

The consistency between observations and the proton calorimeter model, the absence of significant variability, and the spatial coincidence between the GeV emission and the core suggests that this emission originates from interactions between the cosmic-rays and the ISM and not AGN activity thus providing support for the starburst model.

2.4.5 Seyfert properties

The strongest support for a Seyfert classification for Circinus is the presence of its radio lobes. The suggested non-thermal origin of this emission is similar to what is observed in AGNs such as NGC 3079 (Harnett et al., 1990). NGC 3079 is an edge-on spiral galaxy with symmetric radio lobes oriented along its minor axis with one lobe more polarised than the other similar to Circinus (Elmouttie et al., 1995). Its lobe emission originates from a nuclear wind interacting with interstellar material and radiating via the synchrotron mechanism (Harnett et al., 1990).

Elmouttie et al. (1998a) detected a compact radio continuum core providing support for a Seyfert nucleus. In addition, the ionisation cone (Marconi et al., 1994) suggests the presence of a compact source causing this ionisation providing further support for the AGN model. Mingo et al. (2012) proposed that the ionisation cone can result from photoionisation by the AGN, using the spatial coincidence between the X-ray lobe and ionisation cone and emission-line ratios as evidence. A compact coronal line region was also detected in the optical and NIR (near infrared) (Oliva et al.,

1994) consistent with a Seyfert core.

Further evidence against the starburst model includes large variations in the spectral index implying variations in the electron population within the lobes (Mingo et al., 2012). The spectral index flattens at the hotspots suggesting particle acceleration that can be explained by interactions with a radio jet and the ISM. This interaction supplies energy to heat the ISM and creates a bow shock observed as the radio lobe. The lack of observation of the active jet does not imply its absence - this is common in FRII radio galaxies in which the jets are not detected, but the presence of hotspots suggest that there are jets present (Mingo et al., 2012).

2.4.6 Spectral energy distribution

Hayashida et al. (2013) modeled the broadband emission of the lobes of Circinus shown in blue in the SED (spectral energy distribution) in Figure 2.17. They considered a leptonic model including inverse Compton emission with seed photons from the cosmic microwave background (CMB) and the interstellar radiation field (ISRF). A broken power-law model was considered for the electron distribution with a low energy index of 2 between $1 < \gamma < \gamma_{break}$ and a high energy index of 3 for $\gamma_{break} < \gamma < 10^6$. They also considered energy equipartition between the electron energy and magnetic field. This model was constrained using radio (0.4-8.6 GHz) , IR (170-52 μm, 100-25 μm, 70-1 μm), optical (U, B and V bands), X-ray (0.1-2.4 keV, 2-10 keV, 14-195 keV) and *Fermi*-LAT (0.1-100 GeV) data (Hayashida et al., 2013). They used an ISRF model for the Milky Way but applied it at the location of the lobes of Circinus as seed photons for the IC emission. They varied the normalisation of electrons and γ_{break} whilst maintaining energy equipartition and fitting the radio data for the expected IC emission. From this modelling, they found that the observed GeV emission is much higher than what is expected and so there is an excess source of IC needed to explain the GeV emission in Circinus.

2.5 Fermi bubbles

2.5.1 GeV emission

The Milky Way also features a similar emission structure known as the Fermi bubbles. They were first discovered as γ-ray emitting lobes in 2010 with *Fermi*-LAT by Su et al. (2010) but has been detected across the electromagnetic spectrum. They

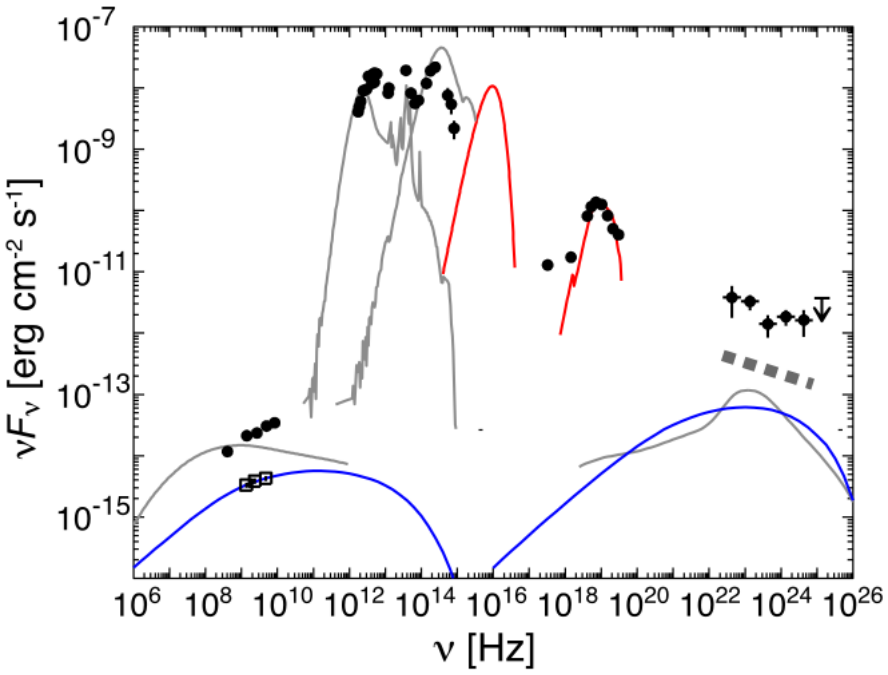

Figure 2.17: Broadband SED of Circinus by Hayashida et al. (2013): Blue curves = modeled synchrotron and IC emission of the lobes and plumes. Grey curves = thermal components of the ISRF, due to emission from the galactic disk (starlight and dust emission), taken from GALPROP models for the Milky Way at the distance of Circinus. Black open squares = the total 'lobes + plumes' radio fluxes. Black filled circles = the total (integrated) fluxes from various catalogs and instruments. Red curves = modeled emission of the accretion disk and the disk coronae. The thick grey dotted line = the γ-ray spectrum of a star-forming system.

are symmetric giant lobes with sharp edges that extend up to 8.5 kpc from the galactic centre. The Milky Way is thus another case of a spiral galaxy with unusually large radio lobes and thus presents a unique opportunity to study nuclear feedback and its interaction with the ISM in a non-elliptical galaxy.

The Fermi bubbles also show enhanced GeV emission found mainly in the south-east region of the bubble identified as the "cocoon" by Su and Finkbeiner (2012). This is seen in Figure 2.18.

2.5.2 Radio & X-ray emission

Carretti et al. (2013) studied the Fermi bubbles in the radio using S-band Polarisation All-Sky Survey (S-PASS) data from the Parkes Radio Telescope shown in Figure 2.19. They found 8 kpc-long linearly polarised radio lobes coincident with the γ-ray counterpart with the exception that the lobes extend a bit further to the west at the top of each lobe. Their observations show that the radio bubbles are

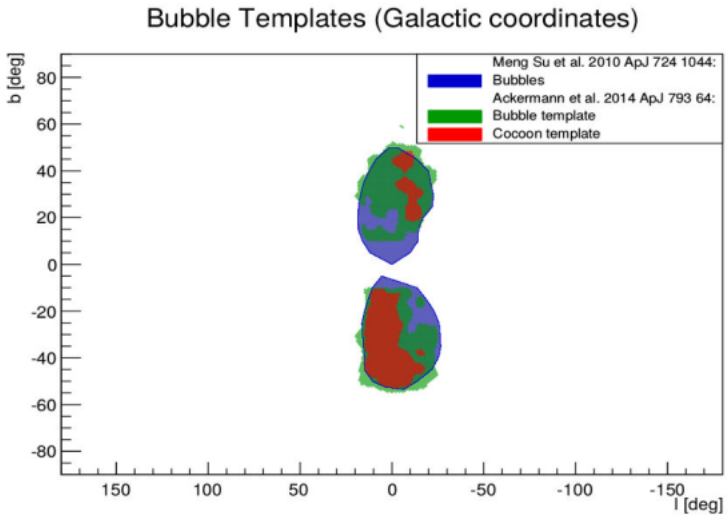

Figure 2.18: Template of the Fermi bubbles and the enhanced GeV emission cocoon (Ackermann et al., 2014) compiled by Hallmann (2015).

bi-conical with star-formation ridges winding along the conical structure.

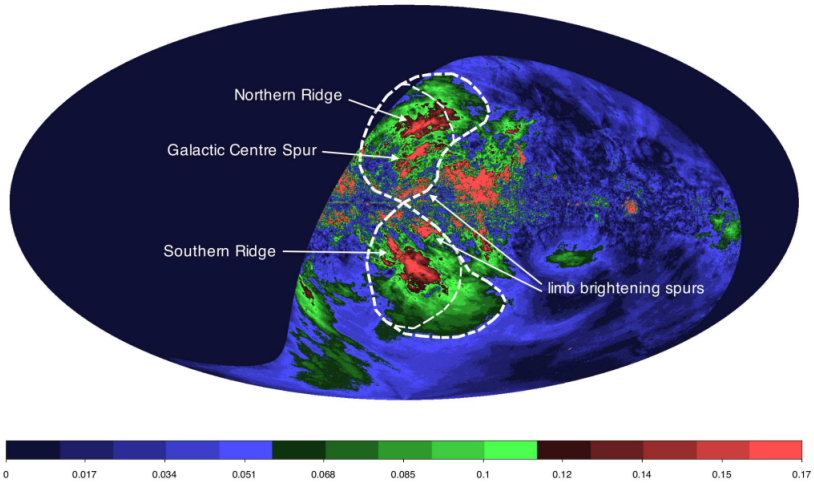

Figure 2.19: 2.3 GHz S-PASS image of the Fermi bubbles by Carretti et al. (2013) with the radio lobes shown as the thick dashed lines and the γ-ray bubbles shown as the thin dashed lines.

The Fermi bubbles were also detected in the X-rays from the ROSAT All-Sky Survey (RASS) at 1.5 keV (Snowden et al., 1997) which spatially correlate well with the γ-ray bubbles seen in Figure 2.20. The ROSAT image lines up with the edges of the Fermi Bubbles usually interpreted as shock waves. The microwave haze observed on the residual Wilkinson Microwave Anisotropy Probe (WMAP) map shows a sphere of radius 4 kpc interpreted as synchrotron emission from cosmic-ray electrons (Finkbeiner, 2004). It was believed that the physical nature of the X-ray and microwave structures are related and this was confirmed by the observation of the

Fermi bubbles which showed similarities between all three structures shown in Figure 2.21 (Su et al., 2010). A cosmic-ray model is required to connect the Fermi bubbles to the WMAP haze in which the same population of cosmic-ray electrons produces the IC GeV emission observed by *Fermi* and synchrotron emission observed as the haze (Su et al., 2010).

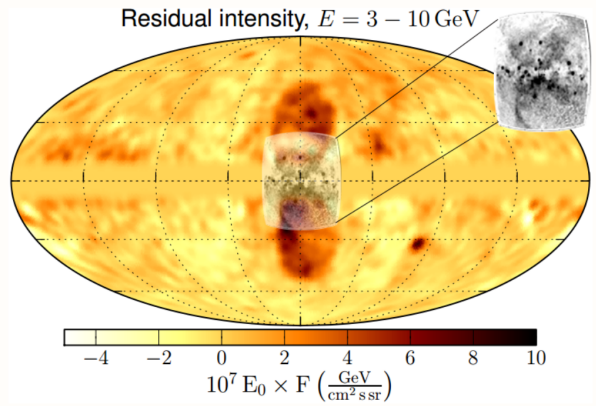

Figure 2.20: ROSAT X-Ray image (Bland-Hawthorn and Cohen, 2003) superimposed on the γ-ray map of the Fermi bubbles (Ackermann et al., 2014) compiled by J.B. Hawthorn.

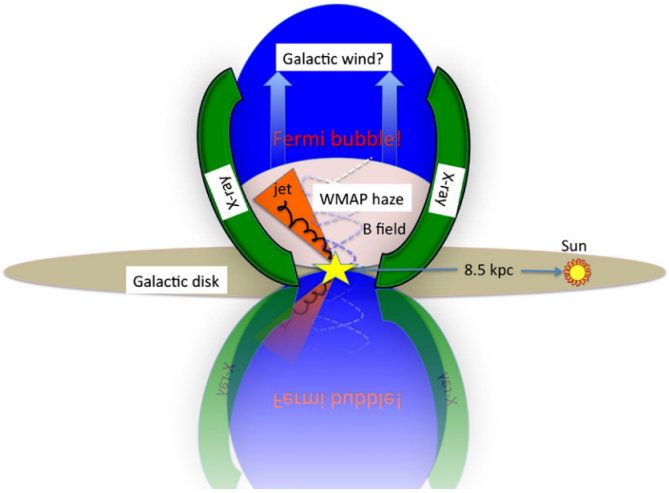

Figure 2.21: Proposed structure of the Fermi bubbles alongside ROSAT X-ray and WMAP observations (Su et al., 2010).

The radio sky also shows loops and spurs of brightened radio emission. This emission is dominated by synchrotron radiation produced by cosmic-ray electrons spiralling in a magnetic field. The loops trace out circles indicative of expanding shells that are best explained as 10^5 – 10^6-year-old SNRs (Spoelstra, 1973). In this SNR model, the SN shock waves trap cosmic-ray electrons and compress the magnetic fields as it pushes through the dense ISM which enables strong synchrotron emission. Loop I, which is most likely within 1 kpc of the Sun [e.g., Dickinson (2018)], has also been modeled well as a superbubble (Egger and Aschenbach, 1996) - a collective effect of

SN explosions and stellar winds (see Section 2.3.1).

A prominent feature of Loop I is the North Polar Spur (NPS) (Baldwin, 1955). The NPS is a ridge of bright radio emission that appears at $l \approx 30°$ where it starts as a narrow ridge perpendicular to the galactic plane and extends for $\sim$30° and thereafter forms part of a wider loop of radio emission (Dickinson, 2018).

Within Loop I are filaments of polarised emission in the north and south of the galactic plane which partially traces out the edge of the Fermi bubbles shown in Figure 2.22 from WMAP/*Planck* polarised intensity maps. This spatial correlation suggests that the filaments and the Fermi bubbles could be produced by the same phenomenon.

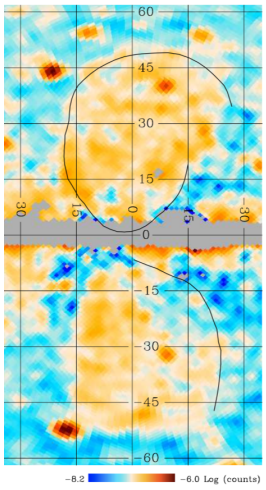

Figure 2.22: *Fermi*-LAT 10-500 GeV map of the Fermi bubbles (Ackermann et al., 2014) with the overlaid black line showing the filaments of Loop I from WMAP/-Planck polarised intensity maps which trace the edges of the bubbles, compiled by Dickinson (2018).

2.5.3 Origin of emission

Similar to the origin of the lobes of Circinus, the origin of this bubble emission is still debated - AGN or starburst driven outflows?

A cosmic-ray model has been proposed to explain this emission where cosmic-ray electrons, accelerated by supernovae, are transported from the galactic plane outward and radiate via the synchrotron mechanism at radio and microwave frequencies (Carretti et al., 2013). This is motivated by the steepening of the spectral index along the flow and the high degree of polarisation observed in the lobes. They provide further support for a star-formation model by reporting that observations in the

γ-ray, X-ray, and microwave bands show the Fermi bubbles to have a narrow waist consistent with a star-forming molecular ring of gas that was observed (Molinari et al., 2011).

AGN origins have also been explored to explain the Fermi bubbles. It has been proposed that the bubble could be caused by a spherical outflow from the core (Zubovas et al., 2011). In this model, the outflow is driven by a combination of a very bright yet brief accretion event on Sgr A*, the supermassive black hole (SMBH) of the Milky Way, and a known star-formation event from $\sim$ 6 Myr ago. The bubbles have also been explained by different jet events that were 1-3 Myr ago [e.g., Guo and Mathews (2012)] and 5-6 Myr ago [e.g., Zhang and Guo (2020)]. The latter jet event model also explains the X-ray structure observed with ROSAT to be caused by the compression of the halo gas by the jet-driven forward shock.

More recently, eROSITA observations showed large-scale X-ray bubbles (Predehl et al., 2020) extending for about 14 kpc above and below the galactic plane. These X-ray observations show the full extent of the X-ray emission compared to the ROSAT observations which only revealed the brighter features. Despite the different morphology of the almost spherical e-ROSITA bubbles and the more elliptical Fermi bubbles (Figure 2.23), the two structures seem to have a common origin. This can be explained in terms of the AGN jet model (Figure 2.4) in which the boundary of the Fermi bubble represents the contact discontinuity and the e-ROSITA bubble beyond it is the cocoon of shocked gas.

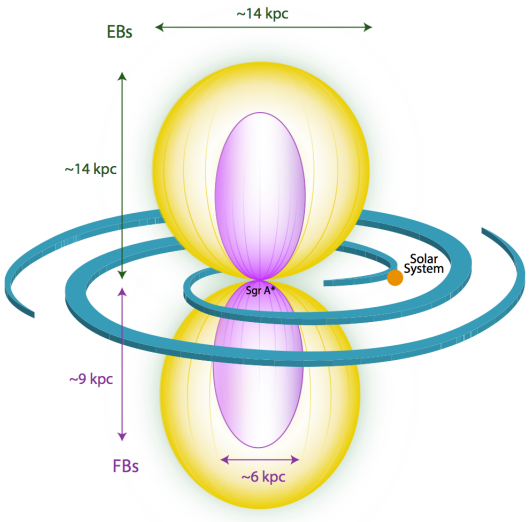

Figure 2.23: Extent of the e-ROSITA bubbles (yellow) compared to the Fermi bubbles (purple) (Predehl et al., 2020).

2.5.4 Fermi bubbles and Circinus' lobes

Several motives make a comparison between the Fermi bubbles and the lobes of Circinus meaningful. This includes comparable central black hole masses in both galaxies, both on the order of 10^6 $M\odot$ (Greenhill et al., 2003). Both "bubbles" are kpc structures with comparable magnetic field strengths of ~ 10 μG. Further, Figure 2.24 compiled by Hayashida et al. (2013) shows that the luminosities of the Milky Way and Circinus are in the 8-1000 μm IR band and 1.4 GHz radio luminosity are the same order of magnitude. The comparable IR luminosity suggests that both galaxies have similar ISRFs used as seed photons for the IC process.

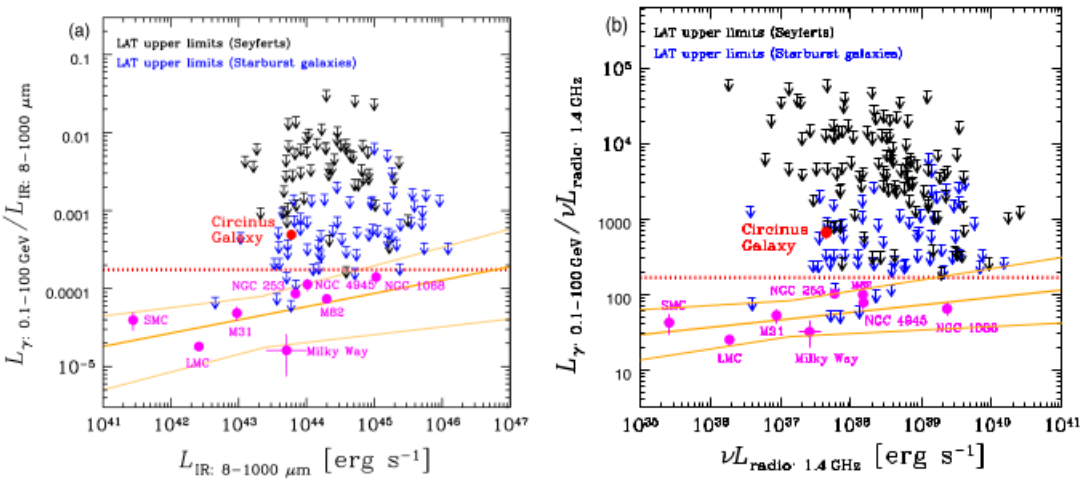

Figure 2.24: a) γ-ray vs. total IR luminosity and b) γ-ray vs. 1.4 GHz radio luminosity for a sample of starburst and Seyfert galaxies (Hayashida et al., 2013).

2.6 SN1996cr

As a consequence of its starburst activity, Circinus is known to host one of the closest Type IIn SNe, SN1996cr, located 25 arcsec south of its nucleus (Bauer et al., 2008). It exploded 25 years ago but was first detected as an X-ray source, CG X-2 (Sambruna et al., 2001), presented as an SN candidate in 2001 (Bauer et al., 2001) and then confirmed as a Type IIn SN in 2007 (Bauer, 2007). Type II SNe are formed through core-collapse processes. Massive stars ($Mass \geq 8M\odot$ (Woosley and Janka, 2005)), can undergo core-collapse at the end of its lifetime until it becomes a proto-neutron star or in the more massive cases, a black hole. The sub-class Type IIn are core-collapse SNe with narrow hydrogen emission lines associated with a dense circumstellar medium (CSM) (Vink, 2017).

A typical structure of the SN and its surroundings is shown in Figure 2.25 (Bauer

et al., 2008) which can be used to explain the idealised picture of SN1996cr. An abrupt end to the progenitor star's core collapse is what drives the forward shock. This forward shock interacts with the CSM or stellar wind (produced by the progenitor star before the SN blast wave) and produces a region of shocked wind behind it, detected in the radio, UV, and hard X-rays. This interaction also generates a reverse shock wave that propagates back into the expanding ejecta to produce the shocked ejecta region. The reverse shockfront's interaction with the ejecta produces radiative cooling downstream that results in the formation of a cool dense shell. The reverse shock is responsible for the soft X-ray emission that can be absorbed by the dense shell that may result in photoionisation observed as optical line emission.

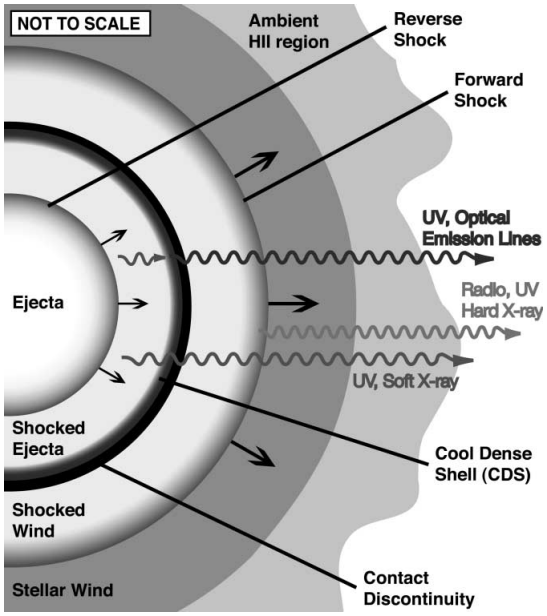

Figure 2.25: Basic setup demonstrating the interaction between a SN, its shocks and the surrounding medium (Bauer et al., 2008).

Studying this SN could provide a better understanding of the interaction between the supernova ejecta and the surrounding CSM. At the shock front, produced by the ejecta/CSM interaction, charged particles are accelerated relativistically to produce non-thermal synchrotron emission (Meunier et al., 2013). This emission can be detected in the radio and so SN1996cr will also be considered for this study.

One way to carry out this SN study is to look at the light curves of SN1996cr. There are two phases to these light curves - an early absorption phase associated with an optically thick medium and a later emission phase with an optically thin medium. During the early phase, the radio emission can be absorbed by two mechanisms: free-free absorption or synchrotron self-absorption (SSA) (Bauer et al., 2008). The mechanisms depend on the magnetic field strength and the density and structure of the CSM. This absorption reduces as the shock waves overcome more of the CSM.

In this study, I will consider the SSA mechanism in the early phase and follow an approach similar to Meunier et al. (2013).

2.6.1 Radio emission

The basic Chevalier synchrotron self-absorption emission model (Chevalier, 1998) is typically used to describe the temporal evolution of SNe radio flux, shown in Equation 2.1 as a function of frequency ν and time t.

$$\begin{aligned} F(\nu,t) =& K1 \left(\frac{\nu}{5\,\mathrm{GHz}}\right)^{\frac{5}{2}} \left(\frac{t}{100\,\mathrm{days}}\right)^{a} \\ & \times \left(1 - exp\left(-K2 \times \left(\frac{\nu}{5\,\mathrm{GHz}}\right)^{-\frac{p+4}{2}} \times \left(\frac{t}{100\,\mathrm{days}}\right)^{-a-b}\right)\right) \end{aligned} \tag{2.1}$$

This model contains four free parameters: $K1, K2, a(m,p)$ and $b(p,m)$ where $K1$ is the flux density normalisation, $K2$ is the optical depth normalisation, a and b are the temporal indices of the radio flux density in the optically thick $[F \propto t^{a}]$ and thin phases $[F \propto t^{-b}]$ respectively, m is the shock deceleration parameter, and p is the power-law index of the emitting electron distribution.

2.6.2 GeV emission

The initial SN blast wave can also accelerate protons which for a very dense CSM (densities in the 10^{7}-10^{12} cm^{-3} range) can inelastically collide with protons in the CSM. This hadronic interaction produces neutral pions which can decay to produce γ-rays. Kantzas et al. (2016) showed that a SN with a distance ≤ 10 Mpc and a density $> 10^{11}$ cm^{-3} could be detected by the *Fermi*-LAT telescope for energies > 100 MeV.

One such case of declining GeV emission has potentially been observed with *Fermi*-LAT in the nearby supernova, SN2004dj (Xi et al., 2020). Results show that the *Fermi*-LAT GeV emission from the host galaxy is unlike the typical cosmic ray (CR)-ISM interaction associated radiation. It is more likely caused by interactions between the SN ejecta and a high-density shell which decelerates the ejecta particles and can lead to the production of relativistic protons (needed for inelastic proton-proton collisions).

2.7 Radio interferometry

MeerKAT is an array of individual radio dishes that operates using interferometry. A detailed review of radio interferometry in practice can be found in [e.g.,Taylor et al. (1999); Thompson et al. (2017)]. To understand this concept simply, one begins with the classical Young's two-slit experiment (Monnier and Allen, 2013). Monochromatic light from a point source placed at infinity is incident on two slits separated by a distance or baseline b. The light then passes through the slit and undergoes diffraction. When the diffracted light is projected onto a screen, it is observed as an interference pattern of bright and dark fringes corresponding to constructive and destructive interference respectively.

As with any telescope, the angular resolution of a radio telescope will determine the quality of the radio observations. The angular resolution of an interferometer with baseline b and a single telescope with a circular aperture diameter D is shown in Equation 2.2 (Monnier and Allen, 2013). The larger the aperture size/effective collecting area of light, the greater the resolution of the image.

$$\begin{aligned} \Delta\theta_{\text{interferometer}} &= \frac{\lambda}{2b}\text{radians} \\ \Delta\theta_{\text{telescope}} &= 1.22 \times \frac{\lambda}{D}\text{radians} \end{aligned} \tag{2.2}$$

This interferometry technique is applied to radio astronomy in which the two slits are now two radio dishes and instead of a screen there is a beam combiner. The light will propagate through each slit or dish with different relative path lengths and it will be out of phase.

In real interferometers a geometric delay is also present due to the sidereal motion of the stars across the sky (Monnier and Allen, 2013). This can be explained by the Figure 2.26 (Thompson, 1989) in which there are two radio dishes, separated by the baseline $\vec{b}$, pointed at a source in the direction $\vec{s}$ ($|s| = 1$). The wavefront propagating from the source at light speed c is delayed in reaching the dish further away by a geometrical delay time τ_g, defined in Equation 2.3.

$$\tau_g = \vec{b} \cdot \frac{\vec{s}}{c} \tag{2.3}$$

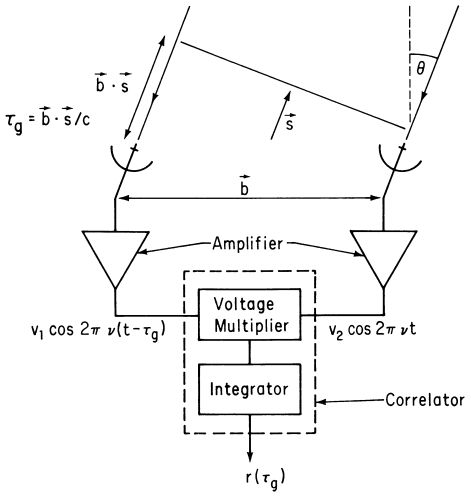

Figure 2.26: Simple two-dish interferometer setup taken from Thompson (1989).

The two signals will then pass through an amplifier which acts as a filter to allow the required bandwidth to pass through. The signals are represented as cosine functions, dependent on the central frequency ν, and are out of phase due to τ_g (shown as the outgoing signals from the amplifier in Figure 2.26). The two signals then pass through an electronic correlator system in which they are combined by being multiplied and then time-averaged.

For an extended source, a phase centre is defined at position $\vec{s_0}$ in the image plane which is used as a reference point for which the measurements are taken of a source element $d\Omega$ located at $\vec{\sigma}$ away from the centre. This setup is shown in Figure 2.27.

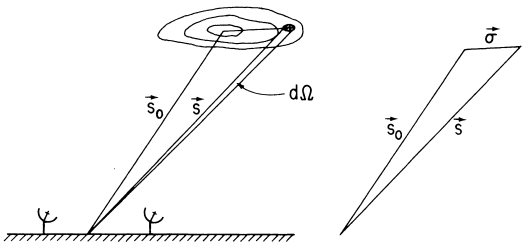

Figure 2.27: Position vectors for extended sources in a two-dish interferometer setup taken from Thompson (1989).

The explanation above describes a two-element interferometer, but it can be applied to an array of dishes. Increasing the number of dishes is equivalent to increasing the aperture size for a larger effective area to collect light, and this results in a greater resolution of the image of the source (Equation 2.2).

Ultimately, we require the brightness distribution of the source which is extracted from the correlator output through the visibility. Mathematically, the visibility V

(in the antenna plane) is the convolution of the brightness distribution of the source I (in the image plane) with the beam of the telescope in Fourier space. The 'beam' includes the main beam corresponding to the signal received from the target source and side lobes corresponding to the radio interference encountered.

Equation 2.4 (Thompson, 1989) shows V which consists of an amplitude to quantify brightness and a phase associated with the position. It is expressed in terms of the radio brightness $I(\vec{\sigma})$, the effective collecting area $A(\vec{\sigma})$ of the antenna, the central frequency ν, baseline $\vec{b}$ and source element $d\Omega$.

$$V = |V| \exp(i\phi_v) = \int_S A(\vec{\sigma}) I(\vec{\sigma}) \exp\left(\frac{-2\pi i \nu \vec{b} \cdot \vec{\sigma}}{c}\right) d\Omega \tag{2.4}$$

Each visibility measurement is taken on a particular baseline which corresponds to a point on the u-v antenna plane. The distance between this point and the origin is equal to the corresponding projected baseline length in units of λ. Thus, the visibility in Equation 2.4 can also be expressed simply in terms of the u-v antenna plane and x-y image plane shown in Equation 2.5.

$$V(u, v) = \int \int I(x, y) \exp(2\pi i(ux + vy)) dx dy \tag{2.5}$$

The visibility is sampled at points in the u-v coordinate system. The greater the u-v coverage, the greater the quality of the resultant image as the visibility at each point produces a different interference pattern and brightness distribution, collectively enabling better image reconstruction of the source.

One of the steps in the imaging processes includes Fourier transforming the visibility to the image plane to recover the measured flux. The measured flux, also referred to as the dirty image, is a convolution of the synthesized beam and the actual brightness distribution. The synthesized beam $B(x, y)$ depends on a weighting function $W(u, v)$ which controls the angular resolution and sensitivity of the final image. There are three types of weightings (Taylor et al., 1999; Briggs, 1995) :

- Natural: This weighting is inversely proportional to the variance in the noise of the (u,v) sample and produces a final image with low noise and high sensitivity. However, this favours shorter baselines that are sampled more than the larger baselines, which compromises the resolution of the image.
- Uniform: This weighting is inversely proportional to the local density of the

(u,v) points and therefore favours longer baselines providing better resolution but with more noise and lower sensitivity compared to a natural weighting.

- Robust (Briggs): This weighting depends on both the noise variance and the local density of points and is thus a combination of uniform and natural weighting. It provides a trade-off between sensitivity and resolution for a smoother image. There is an associated Briggs robustness parameter that varies between -2 (uniform weighting) and 2 (natural weighting).

Through various other deconvolution and calibration techniques, the brightness distribution of the source and thus the final image of the source can be extracted [e.g.,Thompson et al. (2017); Taylor et al. (1999)].

2.8 *Fermi*-LAT

2.8.1 Instrument

Fermi-LAT is a space-based detector of GeV γ-ray emission aboard the *Fermi* Gamma-Ray Space Telescope launched in June 2008.

Some of the γ-ray sources observed by *Fermi* include γ-ray bursts, AGNs, pulsars, and supernova remnants (garner, 2018).These observations can be used to map the γ-ray sky and study acceleration processes, γ-ray bursts, the structure of γ-ray emitting astrophysical objects, and probe the early universe (Atwood et al., 2009). Table 2.1 summarises some of its properties (Abdollahi et al., 2020).

Energy detection range	20 MeV to more than 1 TeV
Effective area	6500 cm^2 for E $>$ 1 GeV
Field of view	2.7 sr for E $>$ 1 GeV
Angular resolution	$\sim 5°$ for E=100 MeV, 0.8° for E=1 GeV and $\sim 0.1°$ for E $>$ 20 GeV
Altitude	550 km

Table 2.1: Properties of the *Fermi*-LAT instrument (Abdollahi et al., 2020).

Fermi-LAT detects γ-rays through a pair production process. The incident γ-rays initially pass through an anti-coincidence detector used to reject any charged particles like cosmic-rays that pass through. The photon then interacts with one of the sixteen layers of tungsten conversion foils to produce an electron-positron pair. Thereafter, this particle pair passes through the tracker which has thirty-six layers of silicon strip detectors to determine the trajectory of the particle. Finally, the

energy of the incident photon is determined through an eight-layer array CsI crystal calorimeter.

2.8.2 Data products and analysis

The *Fermi*-LAT data was downloaded from the LAT data server (available at `https://fermi.gsfc.nasa.gov/`) in a Flexible Image Transport System (FITS) format and was analysed using the standard *Fermi* tools software (version 1.2.23) to perform a likelihood analysis (Mirabal, 2019).

To begin this likelihood analysis, a region of interest (RoI) centered on the target source is selected in which to consider the γ-ray data. Next, the Likelihood L of obtaining the data (counts) given an ensemble of models of the γ-ray emission is found. This is calculated for the null hypothesis (L_0) and the alternate hypothesis which includes the target source (L_1). The model parameters, such as the sources' position, flux, and spectral parameters, are varied until the likelihood ratio is a maximum, where $TS = -2log\left(\frac{L_{max,0}}{L_{max,1}}\right)$. This method will eventually generate a counts map, 3D counts cube, livetime cube, exposure cube, and a model map. In addition to these maps, other useful information is produced, such as the Likelihood value, the expected and observed counts, the spectral model that best fits the data, the average photon flux, and the test statistic value for the maximum likelihood fit. By performing this analysis over defined time bins, the flux can be extracted per bin to produce a GeV light curve. This can be used to study the variability of sources.

4FGL source catalog

The 4FGL source catalog is the fourth major source catalog released by the *Fermi* collaboration based on the first eight years of *Fermi* observations (2008-2016) in the 0.05-1000 GeV energy range.

Abdollahi et al. (2020) report on the improvements in the 4FGL catalog compared to its predecessors. They use Pass 8 data which provides better angular resolution above 3 GeV. 4FGL also has a 20% larger acceptance and an improved high energy PSF. A new galactic diffuse emission model was created for this version of the catalog. They reduced the effects of systematic errors by incorporating a weighting to the maximum likelihood analysis. They also introduced an energy dispersion correction. Unlike previously, they tested each source for the following spectral fits: power-law, log-normal, and a power-law with a sub-exponential cutoff. They

explicitly modeled seventy-five sources as extended emission regions. They also tested for variability using two different time bins - one-year and two-month binning. And finally, they updated the catalogs used to associate $Fermi$ sources with their counterparts at other wavelengths.

There is a test statistic $TS > 25$ detection requirement (and $TS > 34$ for curved spectra) in 4FGL, but some candidates with high significance are still rejected because they are too close to bright sources. For variability, events up to 100 GeV are considered in 4FGL and used a threshold of $TS_{Var} > 18.48$ for the one-year intervals and $TS_{Var} > 72.44$ for the 2-month intervals.

4FGL-DR2 source catalog

4FGL-DR2 (Ballet et al., 2020) is the full fourth catalog with ten years of $Fermi$-LAT data (2008-2018) in the 0.05-1000 GeV range released in 2020. It does not include the 2-month light curves from 4FGL since this method is computationally heavy and most of the variable sources in 4FGL are found from the one-year binned light curves. It uses the same analysis methods as 4FGL and updates all spectral parameters, energy distributions, and associations for all sources. 4FGL-DR2 contains 723 new sources, most of which are just above the detection threshold, two of which have been identified and 342 have potential counterparts at other wavelengths.

Ballet et al. (2020) used the same diffuse γ-ray background model, the same extended source templates, test statistics, and spectral shapes for fitting. For detection and localisation, they began with the original 4FGL sources and relocalized them using the ten years of data. This process resulted in the positions of the sources changing but they fixed the sources to the original positions to ensure consistency with their naming convention.

2.8.3 GeV emission of Circinus with *Fermi*-LAT

Galaxies are known sources of γ-rays especially those which have an AGN at their center. Radio-loud AGNs with relativistic jets typically produce GeV emission due to doppler-boosting effects in their jets. However, GeV emission has also been observed from lobe and bubble structures which can be found in radio-quiet AGNs. There is also GeV emission found in galaxies with significant star-formation. Enhanced SNe explosions and stellar winds serve as acceleration sites for cosmic-rays which interact with the ISM to produce emission (due to the decay of the created neutral

pions) observed at GeV energies.

Circinus' γ-ray emission went undetected in the initial *Fermi*-LAT phase since it is very close to the galactic plane.

Hayashida et al. (2013) analysed Circinus using Pass 7 data which included the first four years of *Fermi*-LAT observations (2008-2012) and the 2FGL source catalog. They considered an energy range of 0.1-100 GeV in a region centered on the galaxy's position and with an RoI of 17°×17°. They performed a maximum likelihood technique to obtain the fluxes and spectra of the GeV emission and used all sources in the RoI from the 2FGL source catalog as well as the isotropic and diffuse galactic emission. This analysis yielded a 7.3 σ excess above the background, but no spatial structure was observed. Furthermore, they searched for a variable Seyfert core by dividing the 4-year period into 6-month intervals and determined the fluxes within each interval but found no significant variability.

More recently, Guo et al. (2019) studied the GeV emission from Circinus using ten years of *Fermi*-LAT data (2008-2018). They considered the energy range of 1-500 GeV with an RoI of 10°×10°. They found a flux significantly lower than Hayashida et al. (2013) compatible with an empirical relation between the γ-ray and total IR luminosity for star-forming galaxies.

They detected an additional point source located 0.43° away from Circinus' core which was not observed by Hayashida et al. (2013). This can be due to the twice longer exposure time of the data and the improvement in Pass 8 data over the Pass 7. They also found another two sources above 1 GeV not found in the source model, which have little influence on the emission from Circinus above 1 GeV, but a greater effect at lower energies. These new point sources that were not found previously meant that Guo et al. (2019) observed a lower luminosity than Hayashida et al. (2013).

In 4FGL-DR2, Circinus has an even lower flux compared to both the 4FGL source catalog and Guo et al. (2019). The positions of the new sources fall within a 95% error ellipse of two 4FGL-DR2 sources not present in 4FGL, which can partly explain the lower flux.

Chapter 3

Methodology

3.1 Radio data

MeerKAT

The MeerKAT array of radio telescopes is located in the Karoo region of South Africa and was launched in July 2018 serving as the precursor to the larger SKA project. It consists of sixty-four 13.5 m offset Gregorian dishes and can provide baselines of up to 8 km (Jonas and MeerKAT Team, 2016). The array centre is located at $30°42'47''$S latitude and $21°26'38''$E longitude. There are two radio band receivers currently installed - the UHF (0.58-1.015 GHz) and L (0.9-1.67 GHz) bands. An S-band (1.75-3.5 GHz) will be installed later on. MeerKAT covers a 5 deg^2 field of view at 0.58 GHz and 0.85 deg^2 fields of view at 1.4 GHz.

This array is capable of extended low brightness emission imaging, observations of mJy scale radio sources, pulsars and transient sources, HI studies, as well as polarization measurements to study magnetic fields (Booth et al., 2009). Higher angular resolution images could also be obtained with VLBI setups of MeerKAT if connected to other radio networks such as the Australian and European VLBI networks since MeerKAT can provide good southern u-v coverage. MeerKAT observations offer a higher sensitivity at a finer angular resolution relative to other existing ground-based radio interferometers.

In this study, 3.6 hours of MeerKAT L-band data of Circinus, taken with sixty-four dishes, from 2018 is used to analyse its continuum radio emission. These data form part of the MeerKAT telescope commissioning observations of the Circinus galaxy,

carried out by the South African Radio Astronomy Observatory (SARAO). I am in collaboration with the authors of the MeerKAT data reduction pipeline (Józsa et al., 2020), to analyse the MeerKAT observations of Circinus which will be published in Thorat et al. (in prep.). This thesis includes my analysis of the continuum images of Circinus. This analysis is done with the python routines written by myself in order to extract flux densities from various regions of the Circinus lobes.

The data is reduced using the Containerized Automated Radio Astronomy Calibration (CARACal), formerly MeerKATHI, pipeline (Józsa et al., 2020). It is platform-independent and combines multiple software required in radio interferometry imaging. CARACal has been developed for both continuum and line radio imaging of MeerKAT data and can work on data from other radio telescopes such as the VLA. The data reduction routine begins with a configuration file specifying the tasks to run on the data and how to carry them out. These tasks include the steps needed in editing, calibrating, and finally imaging the data. Some of the outputs include diagnostic plots, calibration tables, continuum images, spectral-line cubes, and spectral-line moment images.

ATCA

The ATCA instrument is located in Narrabri, New South Wales. It consists of six 22m Cassegrain antennas reaching baselines of up to 6km (Frater et al., 1992). This array is located at $30°18'47''$S latitude and $149°33'0.5''$E longitude. ATCA offers observations between 1.1 GHz and 105 GHz frequencies and is capable of $70''$ resolution at its higher frequency bands.

ATCA has been instrumental in facilitating observations of southern galaxies, extended lobe emission from radio galaxies, SNe and SNRs in the Magellanic clouds including the first image of a forming supernova remnant (SN 1987A) and observations of galactic objects such as masers, pulsars and stellar radio emission (Frater et al., 1992).

3.1.1 Flux calculations

The MeerKAT data was used to compute the flux of the lobe structure which consisted of three regions - the hotspots, lobes and shells. This was done for the MeerKAT radio maps of Circinus listed in Table 3.1.

As discussed in Section 2.7, a Briggs factor close to -2 is associated with a uniform weighting which is ideal for morphology studies in which a larger resolution is required to better observe the extended emission. The MeerKAT images used in this dissertation have Briggs factors ranging from 0 to -1.5 tending towards a uniform weighting.

For a wide-field of interferometric data from non-coplanar telescopes a two-dimensional fast Fourier transform is insufficient in accurate deconvolution. Instead a more complicated imaging algorithm is required which is computationally heavy. WSClean is the wide-field imaging technique (Offringa et al., 2014) applied to the MeerKAT data we use and compared to other techniques provides a good trade-off between not being as computationally intensive but remaining accurate enough.

Central frequency (MHz)	**Bandwidth (MHz)**	**Briggs factor**
1030	10	0
1375	10	0
1020	113	-0.4
1380	142	-0.4
1375	149	-1.0

Table 3.1: MeerKAT radio maps used in the analysis.

Flux region template selection

The template for the shell, lobe and hotspot is based on the template determined by Mingo et al. (2012). Using this template they computed the flux for each of the three regions per lobe at 6 cm (5.0 GHz), 13 cm (2.3 GHz) and 20 cm (1.5 GHz) radio wavelengths using ATCA.

Using their template in Figure 3.1, we approximated the hotspots as ellipses and the shells and lobes as truncated elliptical annuli shown in Figure 3.2. Extracting these regions was done by inserting Figure 3.1 into a data point extraction tool called XYScan. Meaningful points in (R.A., Dec.) coordinates are obtained to define an origin and inclination angle for each lobe, the semi-major and semi-minor axes of each elliptical region and the equation of the lines used as a boundary to truncate the shell and lobe regions.

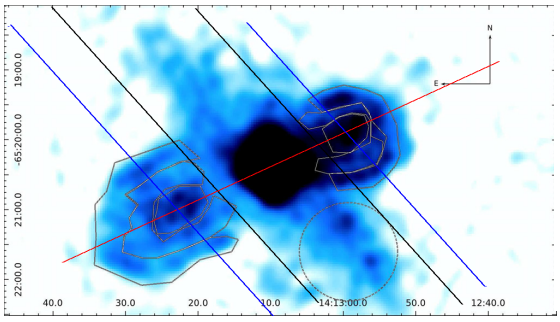

Figure 3.1: Mingo et al. (2012) template of lobes showing the truncation line used in black.

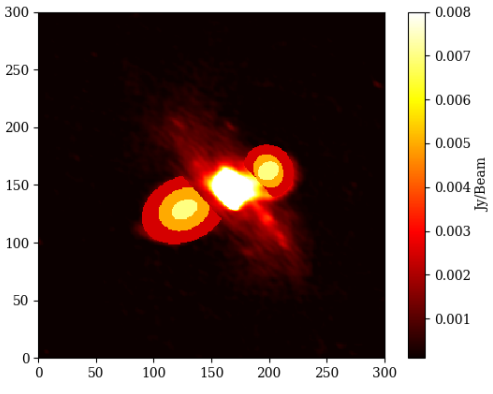

Figure 3.2: Application of Mingo et al. (2012) lobes template to the 1030 GHz MeerKAT radio map showing the hotspots (yellow), lobes (orange) and shells (red) for each lobe.

Computing total flux

The total flux density F in Jy was calculated by summing the map in units of brightness I (Jy/beam) over a number of pixels within the specified region and dividing by the number of pixels in a beam shown in Equation 3.1.

$$F = \frac{\sum_{n=0}^{n_{pixels}} I_n}{Area_{beam}/Area_{pixel}} \tag{3.1}$$

For a sample calculation we can consider the 1030 MHz map which is a 3600×3600 px^2 map with a semi-major Full width at half maximum (FWHM) and semi-minor FWHM of 16.56 arcsec (8.2611 px) and 7.92 arcsec (3.97512 px) respectively and pixel area of 4 arcsec^2 (map scale is 1 px = 2 arcsec). Equation 3.2 shows the calculation for the area of the beam which is an elliptical Gaussian beam in this case.

$$\begin{aligned} Area_{beam} &= 2\pi\sigma_{maj} \times \sigma_{min} = \frac{\pi \times FWHM_{maj} \times FWHM_{min}}{4\ln(2)} \\ &= \frac{\pi \times 16.56\,\text{arcsec} \times 7.92\,\text{arcsec}}{4\ln(2)} \\ &= 148.61\,\text{arcsec}^2 \end{aligned} \tag{3.2}$$

where $\sigma = \frac{FWHM}{2\sqrt{2\ln(2)}}$ and the FWHM corresponds to either the semi-major or

semi-minor axis of the beam.

Finally to compute the flux in a region such as a hotspot we select only the pixels contained within the ellipse that defines the hotspot in Python and sum the brightness (Jy/beam) at each pixel and then divide by the pixels per beam shown in Equation 3.3. The same process is applied to each region in the northern and southern lobe for each map.

$$F = \frac{\sum_{n=0}^{n_{pixels}} I_n}{148.61\,\text{arcsec}/4\,\text{arcsec}} \tag{3.3}$$

Flux errors

To calculate the error on the fluxes ΔF_{region} for each extended region we require the statistical error on the beam which is the root mean square (RMS) value (see Section 3.1.4). Equation 3.4 was used to calculate ΔF_{region} which depends on the computed RMS value for each map and the number of beams contained in the region $\left(N_{beams} = \frac{Area_{region}}{Area_{beam}}\right)$. To calculate $Area_{region}$ we found the number of pixels (n) contained in each region and then multiplied by the area of a pixel in arcsec^2 relative to each map (which is 2×2 arcsec^2 in the 1030 GHz map). $Area_{beam}$ is defined as the area of an ellipse πab, where a and b are the semi-major and semi-minor axis values in arcsec respectively.

$$\Delta F_{region} = RMS \times \sqrt{N_{beams}} \tag{3.4}$$

3.1.2 Beam convolution

The beam size is dependent on the frequency which influences the resolution of the image. Higher frequencies correspond to smaller beam sizes. To conduct meaningful comparisons between radio maps, a beam convolution needs to be applied to smooth the maps to the same resolution. This was applied to the 1370 MHz and 1380 MHz maps which have a higher resolution than the 1030 MHz map and 1020 MHz map.

This technique was achieved using the convolve function of the Astropy python module which applies a convolution between the data from the 1370 MHz map and a 2D elliptical Gaussian beam model with the FWHMs defined in Equation 3.5.

$$
\begin{aligned}
FWHM_{maj} &= \sqrt{(FWHM_{maj_{1030MHz}})^2 - (FWHM_{maj_{1370MHz}})^2} \\
FWHM_{min} &= \sqrt{(FWHM_{min_{1030MHz}})^2 - (FWHM_{min_{1370MHz}})^2}
\end{aligned}
\tag{3.5}
$$

The result of the beam correction is shown in Figures 3.3 and 3.4 in which we can see the 1370 MHz map before and after the convolution is applied, to compare to the original 1030 MHz map in Figure 3.5.

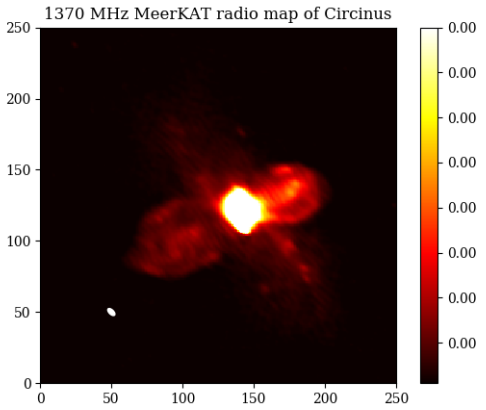

Figure 3.3: 1375 MHz MeerKAT radio image before beam correction. The image RMS is 51.12 μJy/beam and the beam is shown on the bottom left.

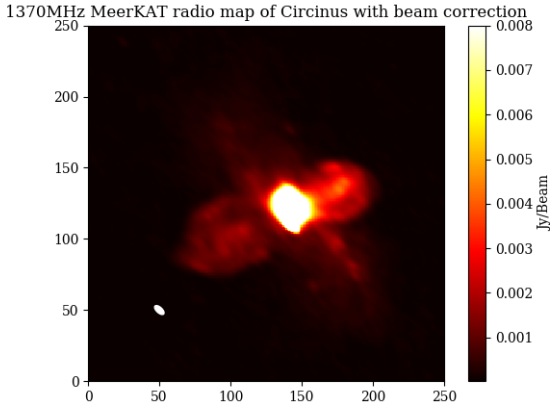

Figure 3.4: 1375 MHz MeerKAT radio image after beam correction and the beam is shown on the bottom left.

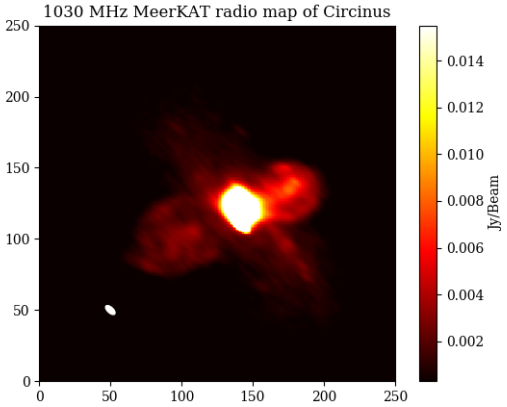

Figure 3.5: 1030 MHz MeerKAT radio image. The image RMS is 92.24 μJy/beam and the 1020 MHz beam is shown on the bottom left.

3.1.3 Spectral analysis

Using the beam correction technique discussed in Section 3.1.2 we computed the spectral indices per pixel between the 1380 MHz smooth map and the 1020 MHz map to generate the spectral index maps shown in Figures 4.6 and 4.7 in Section 4.1.4. To generate this map we used the following procedure:

1. Converted the original radio maps from Jy/beam to Jy/px by dividing by the beam area (Equation 3.2) in pixel units for each map.
2. Fit a single power-law between the flux density values at frequency ν_1 and ν_2 for each pixel to obtain the spectral index value α, shown in Equation 3.6.

$$\alpha = \frac{\log\left(\frac{F_{v_1}}{F_{v_2}}\right)}{\log\left(\frac{\nu_1}{\nu_1}\right)} \tag{3.6}$$

3. Image the spectral index distribution to obtain the spectral index map, by only considering pixels with sufficiently high brightness.

The above procedure produces a spectral index map at the spatial resolution of the 1020 MHz map (18.31×8.19 arcsec^2). Given that we are interested in the extended lobe structure we do not require such fine resolution for the spectral index analysis of the lobes. Before fitting the single power-law, we use the Gaussian2DKernel convolve function of the Astropy python module to convolve the 1020 MHz map and the smoothed 1380 MHz map with a 5×5 pixel^2 Gaussian beam. The final spectral index map after applying this convolution is shown in Figure 4.6 of Section 4.1.4.

Spectral index errors

To compute the error on the spectral index ($\Delta\alpha$) we consider the simplified form of α shown in Equation 3.7, where $a = \frac{1}{\log\left(\frac{\nu_1}{\nu_2}\right)}$ and $x = \frac{F_{\nu_1}}{F_{\nu_2}}$.

$$\alpha = a \log(x) \tag{3.7}$$

We also consider two functions $f(x)$ and $g(x, y)$ and their corresponding errors shown

in Equations 3.8 and 3.9. The last term in the error of $g(x, y)$ vanishes if x and y are independent.

$$\begin{aligned} f(x) &= a \log(bx) \\ \Delta f(x) &= a \frac{\Delta x}{x \ln(10)} \end{aligned} \tag{3.8}$$

$$\begin{aligned} g(x, y) &= \frac{x}{y} \\ \Delta g(x, y) &= |g| \sqrt{\left(\frac{\Delta x}{x}\right)^2 + \left(\frac{\Delta y}{y}\right)^2 - 2\frac{\Delta xy}{xy}} \end{aligned} \tag{3.9}$$

Equation 3.10 shows the final computation of $\Delta\alpha$ after applying Equations 3.8 and 3.9 to Equation 3.7 and assuming the errors in F_{ν_1} and F_{ν_2} are independent.

$$\begin{aligned} \Delta\alpha &= a \frac{\Delta x}{x \ln(10)} \\ &= a \frac{x \sqrt{\left(\frac{\Delta F_{\nu_1}}{F_{\nu_1}}\right)^2 + \left(\frac{\Delta F_{\nu_2}}{F_{\nu_2}}\right)^2}}{x \ln(10)} \\ &= \frac{\sqrt{\left(\frac{\Delta F_{\nu_1}}{F_{\nu_1}}\right)^2 + \left(\frac{\Delta F_{\nu_2}}{F_{\nu_2}}\right)^2}}{\log\left(\frac{\nu_1}{\nu_2}\right) \ln(10)} \end{aligned} \tag{3.10}$$

3.1.4 RMS computation

Region selection for RMS computation

The RMS was calculated by selecting 1000×1000 px^2 regions in each map. The region selection was achieved by using a histogram equalization scale on the radio maps, which enhances the contrast, and choosing a region of noise that is away from the source. For the 1375 MHz map we selected five regions as shown in Figures 3.6 & 3.7. The red, blue and green regions are 1000×1000 px^2 in size and are roughly uniform under the histogram equalization. The magenta and cyan regions are 500×500 px^2 regions to test the RMS for a decrement and increment in background levels

respectively. The regions are centered on the following coordinates:

1. Red = (14:07:56.8232, −65:28:15.969)
2. Blue = (14:16:15.4791, −64:52:48.829)
3. Green = (14:12:21.3379, −64:45:44.757)
4. Cyan = (14:10:44.7445, −65:08:03.593)
5. Magenta = (14:15:23.5737, −65:15:13.870)

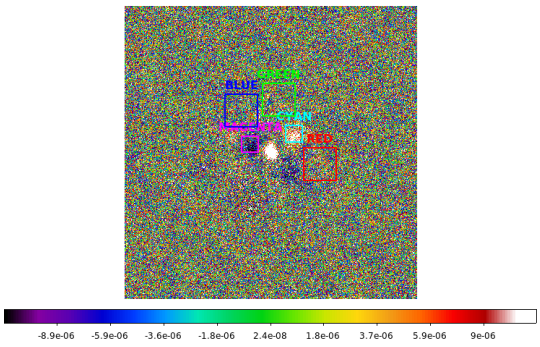

Figure 3.6: Histogram equalisation scaled 1375 MHz radio map with RMS regions outlined.



Figure 3.7: Square-root scaled 1375 MHz radio map with RMS regions outlined.

RMS value calculation

To perform the RMS calculation each region was filled with 100×100 elliptical beams (corresponding to the specifications of the actual beam) and the flux was computed for each ellipse. The RMS value was obtained by calculating the standard deviation of the 100×100 flux values. Astrophysical sources with significance greater than 5σ were excluded. σ was calculated using the relationship that the Mean Absolute Deviation (MAD) value equals the half-normal distribution median, shown in Equation 3.11.

$$MAD = \sigma\sqrt{2}erf^{-1}\left(\frac{1}{2}\right) \approx 0.67449\sigma \tag{3.11}$$

The MAD value was calculated with the astrophysical sources included and then the RMS was recalculated, but by excluding flux values where $S > 5\sigma = 5\frac{MAD}{0.67449}$.

3.2 *Fermi*-LAT data

In modern γ-ray telescopes, such as *Fermi*-LAT, the finest angular resolution is $\sim$5 arcmin which is insufficient to resolve the disk and lobes of Circinus. Instead of a spatial analysis, we perform a search for the variability of the Seyfert nucleus to partially decompose the observed γ-ray emission into the nucleus and diffuse components.

The *Fermi*-LAT γ-ray data for Circinus was obtained from NASA's publicly accessible LAT data server. The data was extracted from the server by specifying the region of interest in terms of a central coordinate and a search radius for a specific period and energy range. This data was downloaded as photon event files which contain the detected counts within the specified region of interest along with its associated energy and trajectory. The event file was accompanied by a spacecraft file which contains a record of the position, orientation, and configuration of the *Fermi* spacecraft. The analysis tools and documentation used was developed by the *Fermi* Science Support Centre (FSSC) and the LAT team (Mirabal, 2019).

3.2.1 Likelihood analysis

For this dissertation, we applied a binned likelihood technique on the Circinus data due to the long observation period of ten years. The steps involved in the analysis are outlined below (Mirabal, 2019):

1. **Sub-selections of the data**

   We performed further cuts on the downloaded events files using the *gtselect* tool (Mirabal, 2019). The specifications for the event selection in this step includes the type of event, the central coordinates (of the target source) and a search radius around it, the time range in Mission Elapsed Time (MET), energy range and the zenith angle cut-off to exclude any background γ-rays from earth:

   - Event class = 128
   - Event type = 3
   - Search center (R.A., DEC.) = (213.291, -65.339)
   - Radius = 15°
   - Start time (MET) = 239 557 418 seconds (2008-08-04)

- Stop time (MET) = 555 033 605 seconds (2018-08-04)
- Minimum energy = 100 MeV
- Maximum energy = 500 000 MeV
- Maximum zenith angle value = 90°

The *gtmktime* tool is used to select good time intervals in which the data quality was good and the spacecraft was in good working condition. We used the filter expression (DATA QUAL>0)&&(LAT CONFIG==1) to make these cuts.

2. **Counts map**

   The *gtbin* tool can be used for various tasks including generating a 2D counts map of the ROI. For our counts map we use an image scale of 0.1 °/px (as done by Guo et al. (2019)) which requires a 300×300 px^2 map for an ROI of 15° ($\frac{15°\times 2}{0.1°/\mathrm{px}} = 300\,\mathrm{px}$). The counts map is useful to check if the ROI is centred on the target source and if other sources that may affect the analysis are present.

3. **3D binned counts map**

   gtbin is also used to generate a 3D counts map to include an energy axis. The data is binned into 27 logarithmically uniform energy bins from the available energy range to create a counts cube. Generating the cube also includes specifying the size of the largest square that fits within the circular ROI of 15°. The maximum side length of the square is 21.21° corresponding to 200 pixels ($\frac{21.21°}{0.1°/\mathrm{px}}$).

4. **Diffuse model files**

   The galactic diffuse and extragalactic isotropic diffuse γ-ray backgrounds were modeled by the *gll_iem_v07.fits* and *iso_P8R3_SOURCE_V2_v1.txt* files respectively, downloaded from the LAT data server [1].

5. **Source model**

   A source model is required in the analysis which contains the positions, energies, and spectral models of all sources in the ROI and the coefficients of the galactic and extragalactic isotropic background components. A python script provided by the FSSC is used to generate the source model in Extensible Markup Language (XML) format which uses the latest *Fermi* point source catalog *gll_psc_v23.fits* and the diffuse background model files as inputs. The various parameters of all the sources and backgrounds in the XML file can be edited to free or fix as required. The FSSC documentation recommends only

[1] Available at `https://fermi.gsfc.nasa.gov/cgi-bin/ssc/LAT/LATDataQuery.cgi`

freeing all spectral parameters of sources near the target source or near bright sources in the ROI and only freeing the normalisation of sources further way. Section 3.2.2 covers our approach related to freeing parameters.

6. **Livetimes and exposure**

   To generate the exposure map in the next step, a livetime cube is created using the *gtltcube* tool. The livetime refers to the duration that the instrument observed the ROI at a given position and inclination angle (relative to the z-axis of *Fermi*-LAT). We used the default $\cos\theta$ step size of 0.025 and 1° pixel size for the cube.

7. **Exposure map**

   The livetime cube is applied to the ROI using the *gtexpcube*2 tool to create a binned exposure map of $Area \times Time$. In this step, an extra 10° is added to the ROI to account for the contributions from sources beyond the ROI at lower energies due to the large PSF. Hence the exposure map we generated was 600×600 px^2 for an image scale of 0.1°/px.

8. **Source map**

   Using the *gtsrcmaps* tool we create a map of the counts expected from the model given the total exposure.

9. **Likelihood fit**

   Steps 1-8 cover the prerequisites for the likelihood fit. *gtlike* uses the source map, exposure map, livetime cube, and input model, and varies the free parameters in the source model until the likelihood function is maximised and the observations best match the model. There are five different optimisation algorithms to choose from - DRMNGB, DRMNFB, NEWMINUIT, MINUIT, and LBFGS. The FSSC recommends using the first two to find the initial parameter estimates and then using NEWMINUIT or MINUIT to refine the results. In the ten-year binned likelihood analysis, we used NEWMINUIT and achieved convergence on the first run. For our analysis in the context of SN1996cr (Section 3.5.2) we tried different algorithms and even a combination of two to achieve convergence.

   This step outputs the best-fit spectral parameters of the sources, the observed counts, the model counts, the final value of $\log(L)$, counts versus energy graph for the observed and model counts, and a residuals graph between the model and observations.

10. **Model Map**

A model map can be created using the *gtmodel* tool using the final best-fit parameters which can be compared to the observed counts map.

3.2.2 Approach

The binned likelihood analysis was run on the ten-year data set for the cases labeled as versions 1-9 shown in Table 3.2. For all approaches except v4, we used a minimum energy of 0.1 GeV. We also considered an ROI of sources within which we freed certain spectral parameters. Also, we varied other spectral parameters of the bright pulsar 4FGL J1356.9−6432 that lies within 3° of Circinus in v7-v9. This was done because the likelihood fit output a normalisation significantly larger than the value given by the *Fermi* 4FGL-DR2 catalog for the pulsar in v1-v6 when the normalisation was the only free parameter.

Version	$\mathbf{e}_{min}$ **(GeV)**	**Galactic background normalisation**	**Isotropic background normalisation**	**Freed spectral parameters of other sources**	**Number of free parameters**
v1	0.1	Free	Free	Normalisation of sources within a 3° ROI	16
v2	0.1	Free	Free	All spectral parameters of sources within a 3° ROI	51
v3	0.1	Free	Free	Normalisation of sources within a 5° ROI	47
v4	1.0	Free	Free	Normalisation of sources within a 3° ROI	16
v5	0.1	Free	Free	Normalisation of sources within a 3° ROI	15
v6	0.1	Fixed	Free	Normalisation of sources within a 3° ROI	14
v7	0.1	Fixed	Fixed	Normalisation of sources within a 3° ROI All spectral parameters of 4FGL J1356.9−6432	18
v8	0.1	Free	Free	Normalisation of sources within a 3° ROI All spectral parameters of 4FGL J1356.9−6432	20
v9	0.1	Free	Free	Normalisation of sources within a 3° ROI Normalisation, index1 and expfactor of 4FGL J1356.9−6432	18

Table 3.2: Summary of all nine approaches of the binned likelihood analysis over the full ten years.

3.3 Broadband emission modelling

We modeled the broadband emission of the lobes of Circinus by producing its spectral energy distribution (SED) which is used to make predictions for its TeV emission. The model assumes a leptonic scenario with a broken power-law electron distribution $f(\gamma)$, where γ is the Lorentz factor[2], shown in Equation 3.12 and an equipartition between the electron energy and magnetic field energy $\left(\frac{U_e}{U_B} = 1\right)$.

[2] $\gamma = \frac{E}{m_e c^2}$, where E is the total energy of the relativistic electron of rest mass m_e and c is the speed of light in a vaccuum.

$$f(\gamma) = \begin{cases} \gamma^{-2.2}, & \text{if } \gamma \leq \gamma_{break} \\ \gamma^{-3.2}, & \text{if } \gamma > \gamma_{break} \end{cases} \tag{3.12}$$

In this model, the γ-ray emission is produced via the IC scattering of the CMB photons by high-energy electrons. The low-energy electrons of the same electron power-law population are responsible for synchrotron emission which is detected in the radio band.

To begin the modelling we use a similar approach taken by Hayashida et al. (2013). Using their input parameters as a guide we attempted to reproduce their SED model shown in Figure 2.17.

3.3.1 Input parameters

We will begin with a discussion on what the required parameters are and how we obtained them.

Radius calculation

To obtain the model we require information about the emitting region starting with its size. We use the Hayashida et al. (2013) lobes+plumes template which they define as follows:

- North West (NW) lobe: a circle of radius 44.6 arcsec.
- South East (SE) lobe: an ellipsoid with radii of 70 arcsec and 55 arcsec.

Using these specifications and assuming axial symmetry the effective volume of the emitting region is calculated from which the effective radius in cm is extracted. For this calculation the following relations were used:

1. Volume of an ellipse: $V = \frac{4}{3}\pi abc$, where a, b & c correspond to the semi-major axis, semi-minor axis, and height of the ellipse respectively.
2. To find the scale relation between 1 arcsecond and the distance d to Circinus

in kpc we consider a source diameter D of 1 kpc shown in Equation 3.13.

$$\begin{aligned} \theta = \frac{D}{d} = \frac{1\,\mathrm{kpc}}{4000\,\mathrm{kpc}} \times \frac{180\,\mathrm{deg}}{\pi}\frac{3600''}{1\,\mathrm{deg}} = 51.6'' \\ \text{Hence } 1\,\mathrm{kpc} = 51.6'' \Rightarrow 1'' = 0.019\,\mathrm{kpc} \end{aligned} \tag{3.13}$$

3. 1 kpc = 3.086×10^{21} cm

The volume of the lobes are calculated in Equations 3.14 and 3.15 to obtain the effective volume and radius shown in Equations 3.16 and 3.17 respectively.

$$\begin{aligned} V_{NWlobe} &= \frac{4}{3}\pi(70.0'' \times 55.0'' \times 55.0'')\left(0.019\frac{\mathrm{kpc}}{1''}\right)^3\left(3.0\times10^{21}\frac{\mathrm{cm}}{\mathrm{kpc}}\right)^3 \\ &= 1.75\times10^{65}\,\mathrm{cm}^3 \end{aligned} \tag{3.14}$$

$$\begin{aligned} V_{SElobe} &= \frac{4}{3}\pi(44.6'' \times 44.6'' \times 44.6'')\left(0.019\frac{\mathrm{kpc}}{1''}\right)^3\left(3.0\times10^{21}\frac{\mathrm{cm}}{\mathrm{kpc}}\right)^3 \\ &= 7.33\times10^{64}\,\mathrm{cm}^3 \end{aligned} \tag{3.15}$$

$$V_{eff} = \left(1.75\times10^{65}\right)\,\mathrm{cm}^3 + \left(7.33\times10^{64}\right)\,\mathrm{cm}^3 = 2.48\times10^{65}\,\mathrm{cm}^3 \tag{3.16}$$

$$R_{eff} = \left(\frac{3V_{eff}}{4\pi}\right)^{\frac{1}{3}} = 3.90\times10^{21}\,\mathrm{cm} \tag{3.17}$$

Magnetic field

The commonly accepted magnetic field strength of lobes is between 1.0-10.0 μG. Hayashida et al. (2013) varied the magnetic field between 5-10 μG to find the best fit for their SED. Kataoka et al. (2018) used a magnetic field strength of 12 μG in their SED model of the Fermi bubbles. We varied the magnetic field to find the best fit.

Electron distribution

We assumed a broken power-law for the electron distribution consistent with Hayashida et al. (2013) shown in Equation 3.12. The spectral indices and electron energy range used in the model are shown in Table 3.3 compared with the values used by Hayashida et al. (2013).

We choose a γ_{min} and γ_{max} equal to the value used by kataoka2018 in their SED model of the Fermi bubbles. Their SED model, with this same value for γ_{min} and

Parameter	Our model	Hayashida et al. (2013)
α_1 (Spectral index 1)	2.2	2.0
α_2 (Spectral index 2)	3.2	3.0
γ_{min} (Electron energy minimum)	2.0×10^3	1.0
γ_{max} (Electron energy maximum)	1.0×10^8	1.0×10^6

Table 3.3: Fixed parameters of the broken power-law electron distribution used in the SED model of the lobes of Circinus compared with Hayashida et al. (2013) .

γ_{max}, is consistent with *Fermi*-LAT GeV observations, WMAP radio observations, and within the upper limit set by Suzaku X-ray data for the Fermi bubbles (Figure 3.8 (Kataoka et al., 2018)). The model by Hayashida et al. (2013) for the Circinus lobes describes only the radio band points and is not as well-constrained in the γ-rays. The spectral index of the electron distribution α is motivated by the derived spectral radio index r from the MeerKAT observations which is ~ 0.6 (See Table 4.6 in Chapter 4). For $r = 0.6$ we expect $\alpha = 2.2$ since $\alpha = 2r + 1$.

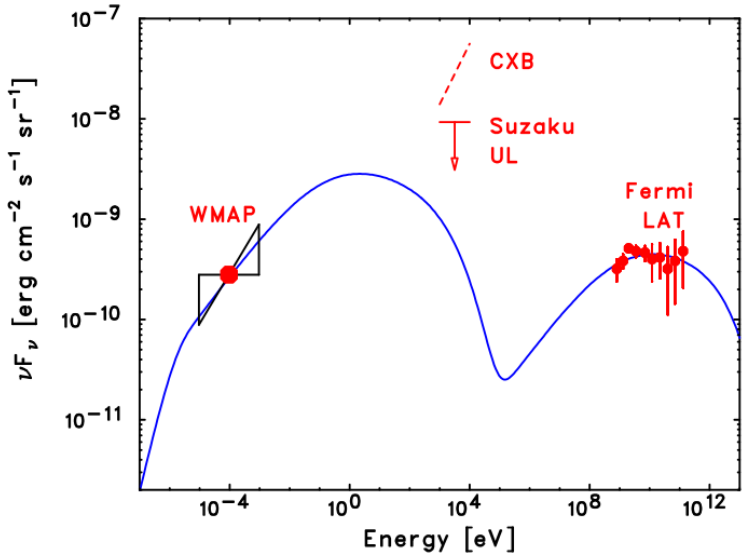

Figure 3.8: Broadband SED of the Fermi bubbles by Kataoka et al. (2018).

The energy at which the spectral index of the power-law changes γ_{break} and the amplitude N (number of electrons per unit volume) is varied to find the best fit.

Assumptions on emission

For the modelling, we considered synchrotron emission and inverse Compton emission. Initially, we only considered CMB seed photons for the inverse Compton, but we later extended this to external radiation fields which we discuss in Section 3.3.5.

3.3.2 Broadband emission data

Radio data

To constrain the model we used radio flux data from ATCA and MeerKAT. The ATCA data was taken from Mingo et al. (2012). Equation 3.18 shows the computation of the MeerKAT flux data point (in Equation 3.19) as the sum of the measured flux density values of the lobes, hotspots, and shells at $\nu = 1.375$ GHz from Table 4.5 in Chapter 4.

$$F_{1.375\,\mathrm{GHz}} = (21.42+37.16+47.56+40.86+61.03+50.01)\,\mathrm{mJy} = 258.04\,\mathrm{mJy} \quad (3.18)$$

$$\begin{aligned}\nu \times F_{1.375\,\mathrm{GHz}} &= 1.375\,\mathrm{GHz} \times 258.04\,\mathrm{mJy} \times \left(\frac{1.0 \times 10^{-23}\,\mathrm{erg\,s^{-1}\,cm^{-2}\,Hz^{-1}}}{1\,\mathrm{Jy}}\right) \\ &= 3.55 \times 10^{-15}\,\mathrm{erg\,s^{-1}\,cm^{-2}}\end{aligned} \quad (3.19)$$

where $1\,\mathrm{Jy} = 10^{-23}\,\mathrm{erg\,s^{-1}\,cm^{-2}\,Hz^{-1}}$. The ATCA radio flux was calculated using the reported fluxes of the lobe structure by Mingo et al. (2012) (Table 4.5 of Chapter 4).

X-ray data

Mingo et al. (2012) considered that the total X-ray emission from the Circinus lobes is due to thermal free-free emission and provided the best-fit values of their model. The X-ray flux density (in the soft X-ray band) is roughly estimated using thermal free-free emission and can thus be used as an upper limit on non-thermal emission shown in Equation 3.20.

$$\nu \times F_{2.4\times10^{17}\,\mathrm{Hz}} = 1.8 \times 10^{-14}\,\mathrm{erg\,s^{-1}\,cm^{-2}} \quad (3.20)$$

3.3.3 Sensitivity curves for γ-ray observations

To study the γ-ray emission we compared our model to what we expect to see with γ-ray telescopes like CTA and *Fermi*-LAT.

The proposed setup for the CTA southern site (CTA-South) includes 4 large telescopes, 25 medium ones and 70 smaller ones (CTA Consortium and Observatory, b). For CTA-South we considered the minimum differential flux sensitivity curve for an observation time of 50 hours (see Figure 3.9 (CTA Consortium and Observatory, a)). The differential sensitivity for CTA is defined as the minimum flux needed to obtain a 5σ detection of a point-like source. Other factors determine the detection possibility such as a requirement of at least ten detected γ-rays per energy bin and a signal to background ratio of at least 1:20.

Similarly, for *Fermi*-LAT we considered the minimum differential flux sensitivity for a ten-year observational period which is at the position of (b,l)=(45 deg, 120 deg) (see Figure 3.10 (Maldera et al., 2019)).

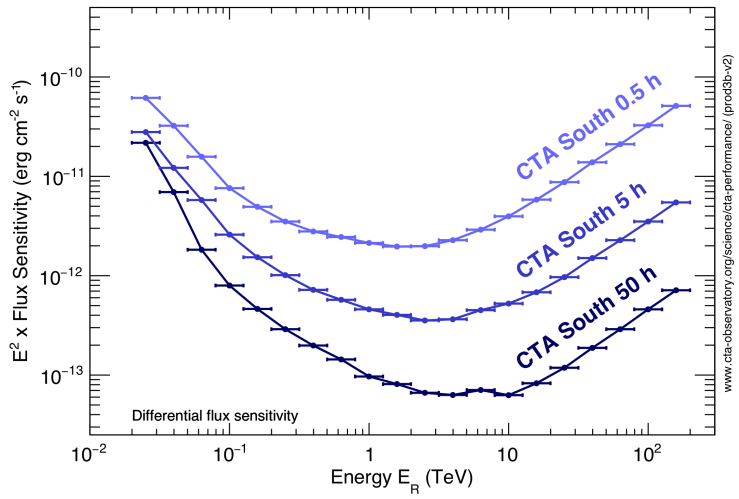

Figure 3.9: CTA-South differential flux sensitivity curves (CTA Consortium and Observatory, a).

3.3.4 Case 1

As a starting point for the SED modelling, we used the SSC/EC Simulator, an online AGN SED tool, created by Andrea Tramacere (Tramacere et al., 2009, 2011; Massaro et al., 2006). This tool reproduces the radiative and accelerative processes in the jets of Blazars. We applied this to the lobes of Circinus by assuming an

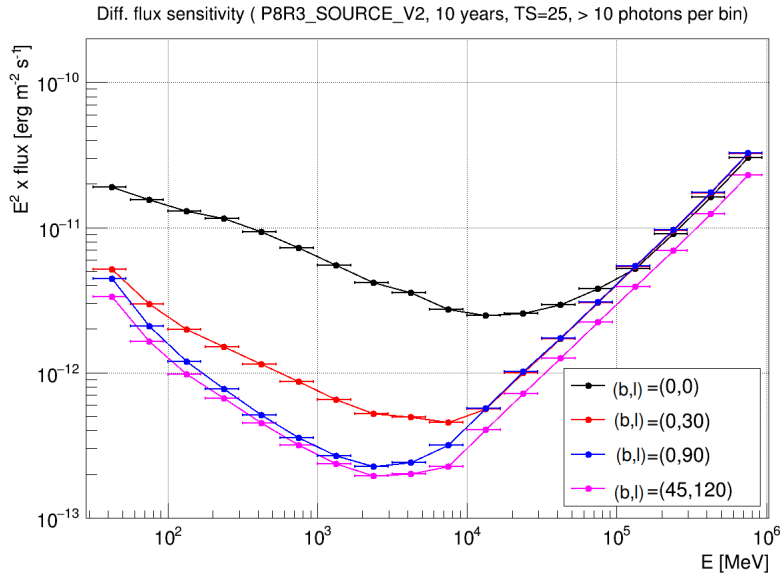

Figure 3.10: *Fermi*-LAT differential flux sensitivity curves (Maldera et al., 2019).

external inverse Compton model. A bulk Lorentz factor of the jet $\Gamma = 1$ is assumed which is the case for a stationary region like the lobes of Circinus.

Using the input parameters discussed in Section 3.3.1 the simulator generates a SED plot and the model data, in which we varied the free parameters each time. When choosing the parameters we considered those used by Hayashida et al. (2013) and also those used by Kataoka et al. (2018) in their SED modelling procedure of the Fermi bubbles shown in Figure 3.8.

3.3.5 Case 2

We then considered the case in which the electrons interact with the CMB and ISRF including the FIR and NIR photon fields via the inverse Compton mechanism. For this we modeled the SED using the Python module Naima using the same parameters and energy equipartition, but with energies specified in eV as opposed to Lorentz factors[3]:

- $\alpha_1 = 2.2$ & $\alpha_2 = 3.2$
- $\gamma_{min} = 2.0 \times 10^3 \leftrightarrow E_{\gamma_{min}} = 1$ GeV
- $\gamma_{max} = 1.0 \times 10^8 \leftrightarrow E_{\gamma_{max}} = 51$ TeV

[3] $\gamma = \frac{E}{E_e}$ where E = total energy and E_e = rest mass energy of an electron = 0.511 MeV.

- $\gamma_{break} = 5.0 \times 10^6 \leftrightarrow E_{\gamma_{break}} = 2.55 \times 10^3$ GeV
- $Amplitude = 1.427 \times 10^{46}\,\mathrm{eV}^{-1}$
- $B = 3.5\,\mu\mathrm{G}$
- $r = 3.90 \times 10^{21}\,\mathrm{cm} = 1.3 \times 10^3$ pc

Modelling the ISRFs

Hayashida et al. (2013) considered the inverse Compton seed photons to come from the CMB, the observed IR-to-optical emission of the galactic disk (dominant starlight and dust emission), and the UV-to-hard X-ray photons due to the AGN. In their SED in Figure 2.17 in Chapter 2, they display the ISRF used as the grey curve obtained from the GALPROP models for the Milky Way applied at the distance of Circinus. This technique can be applied given that the total IR luminosity of Circinus and the Milky Way are similar. This can be seen in the plot by Tang et al. (2014) shown in Figure 3.11.

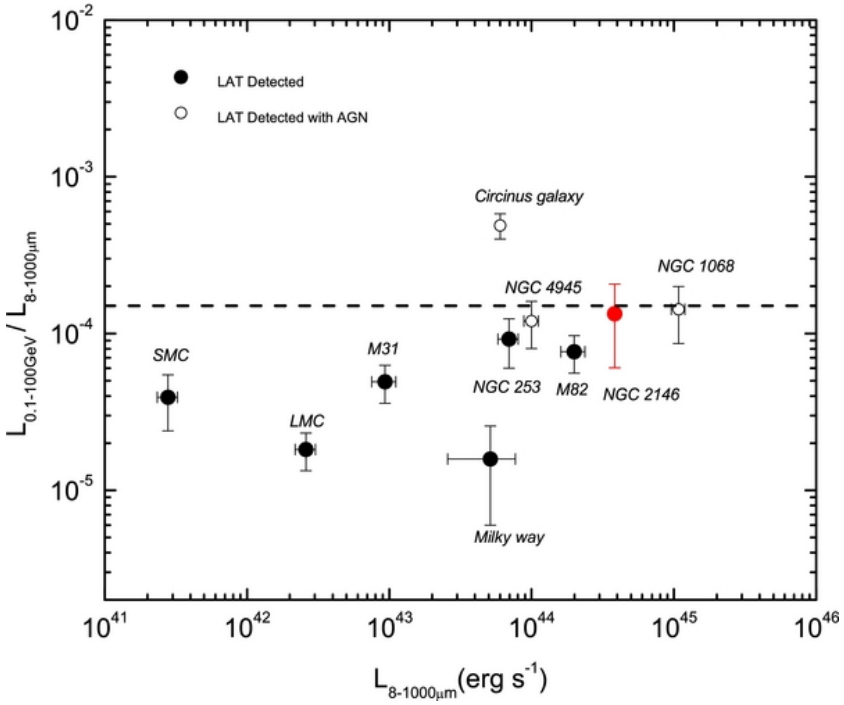

Figure 3.11: Ratio between the γ-ray luminosities (0.1-100 GeV) and total IR luminosities (8-1000 μm) for a sample of Seyferts and star-forming galaxies detected by *Fermi*-LAT (Tang et al., 2014).

Modelling the thermal photon fields requires their temperature and energy densities at the positions of the radio lobes in the Circinus galaxy to use as inputs in Naima

to generate the SED. Typically in Naima for the CMB, NIR, and FIR, the radiation field temperatures are 2.72 K, 30 K, and 3000 K, and the energy densities are 0.261 eV/cm^3, 0.5 eV/cm^3, and 1 eV/cm^3 respectively for the Milky Way's ISRF fields 6.5 kpc away. In our case, we generated the same ISRF model of the Milky Way at the position of the Circinus lobes, used in the GALPROP code [e.g., (Porter et al., 2006)] and used by Hayashida et al. (2013), and extracted the best-fit temperature and energy densities.

The ISRF model is a FITS file in cylindrical coordinates in units of μm eV cm^{-3} μm^{-1}. It is a cube with four axes:

1. Radius in px
2. Height in px
3. Frequencies
4. Components

The radius and height axes define the three-dimensional region for which to calculate the field and the component axis refers to the three photon fields included in this model, i.e. optical, infrared, and the CMB. Using this data, we can plot the radiation $\left(\lambda \frac{du}{d\lambda}\right)$ as a function of wavelength for the ISRF and given that these are thermal photon fields we can fit a blackbody spectrum to the radiation curve. From this fit, we can extract the peak wavelength λ_{peak} and compute the corresponding blackbody temperature T from Wien's displacement law shown in Equation 3.21.

$$T = \frac{b}{\lambda_{peak}} = \frac{3000\,\mu\mathrm{m\,K}}{\lambda_{peak}} \tag{3.21}$$

To obtain the energy density u we integrate the radiation over wavelength shown in Equation 3.22.

$$u = \int \frac{du}{d\lambda} d\lambda \tag{3.22}$$

The T and u from Equations 3.21 and 3.22 respectively can then be used as inputs for Naima to specify the parameters of the ISRF for each component. For the remainder of this dissertation, we will refer to the FIR component as the low-temperature component and NIR as the high-temperature component. For the lobes of Circinus we use the minimum radius in the model which is $R = 0.25$ kpc and a height $z = 0.5$ kpc given that the lobes extend to about 1 kpc.

3.3.6 NGC 1068

To test our VHE emission modelling technique, we also applied it to another Seyfert lobed galaxy - NGC 1068. Wilson and Ulvestad (1987) report a 13 arcsec (∼1 kpc) linear radio source at the centre of NGC 1068 from 12 cm VLA radio maps. The NE lobe extends 400 pc beyond the nucleus (Wilson and Ulvestad, 1987), making the lobes roughly 0.5 kpc each.

Using the observations reported by Wilson & Ulvestad (1987) and a similar method used above for the lobes of Circinus, we determined the best-fit parameters to model the SED.

For the blackbody spectrum fit of the low-temperature ISRF component, we scale the normalisation by a factor of ten given that NGC 1068 is ten times more luminous in the FIR (8-1000 μm) band compared to the Milky Way and Circinus also shown in Figure 3.11 (Tang et al., 2014). Applying this normalisation we computed the ISRF for the same radius $R = 0.25$ kpc, but a height $z = 0.2$ kpc and obtained the corresponding blackbody spectra and thus temperature and energy densities for each component.

Once we obtained the SED model, we constrained it further using the radio flux densities of each lobe reported by Wilson and Ulvestad (1987) at 4.885 GHz and 14.965 GHz:

- **4.885 GHz**: $F_{NE\,lobe} = 0.58$ Jy & $F_{SW\,lobe} = 0.28$ Jy $\Rightarrow F_{total} = 0.86$ Jy

$$\begin{aligned}\nu \times F_{4.885\,\mathrm{GHz}} &= (4.885 \times 10^{9}\,\mathrm{Hz}) \times (0.86\,\mathrm{Jy}) \times (1.0 \times 10^{-23}\,\mathrm{erg\,s^{-1}\,cm^{-2}\,Hz^{-1}\,Jy^{-1}}) \\ &= 4.2 \times 10^{-14}\,\mathrm{erg\,s^{-1}\,cm^{-2}}\end{aligned}$$

- **14.965 GHz**: $F_{NE\,lobe} = 0.18$ Jy & $F_{SW\,lobe} = 0.07$ Jy $\Rightarrow F_{total} = 0.25$ Jy

$$\begin{aligned}\nu \times F_{14.965\,\mathrm{GHz}} &= (14.965 \times 10^{9}\,\mathrm{Hz}) \times (0.25\,\mathrm{Jy}) \times (1.0 \times 10^{-23}\,\mathrm{erg\,s^{-1}\,cm^{-2}\,Hz^{-1}\,Jy^{-1}}) \\ &= 3.7 \times 10^{-14}\,\mathrm{erg\,s^{-1}\,cm^{-2}}\end{aligned}$$

Modelling the lobes

In Wilson and Ulvestad (1982) they describe the NE lobe to be a cone with its apex 5.6 arcsec from the nucleus and a half apex opening angle $\theta = 20°$. They describe the SW lobe as a diffuse radio lobe of diameter 6 arcsec. Given that the SW lobe is much larger than the NE lobe, we model them separately.

For the NE lobe, we calculate a radius r (Equation 3.23) assuming a conical shape of height h for the NE lobe to obtain its volume $V_{NE\,lobe}$ (Equation 3.24). From this volume, the effective radius r_{NE} can be extracted assuming a spherical emitting region shown in Equation 3.25.

$$r = h \times tan(\theta) = 5.6\,\mathrm{arcsec} \times \tan(20°) = 2.04\,\mathrm{arcsec} \tag{3.23}$$

$$V_{NE\,lobe} = \frac{\pi}{3} r^2 h = 24.40\,\mathrm{arcsec}^3 \tag{3.24}$$

$$\begin{aligned} r_{NE} &= \left(\frac{3V_{NE\,Lobe}}{4\pi}\right)^{\frac{1}{3}} = \left(\frac{3 \times 24.40\,\mathrm{arcsec}^3}{4\pi}\right)^{\frac{1}{3}} \\ &= 1.8\,\mathrm{arcsec} \times \frac{73\,\mathrm{pc}}{1\,\mathrm{arcsec}} \times \frac{3.086 \times 10^{21}\,\mathrm{cm}}{1000\,\mathrm{pc}} = 4.06 \times 10^{20}\,\mathrm{cm} \end{aligned} \tag{3.25}$$

For the SW lobe, we considered a spherical lobe of radius $r_{SW} = 3$ arcsec given in cm as shown in Equation 3.26.

$$r_{SW} = 3.0\,\mathrm{arcsec} \times \frac{73\,\mathrm{pc}}{1\,\mathrm{arcsec}} \times \frac{3.086 \times 10^{21}\,\mathrm{cm}}{1000\,\mathrm{pc}} = 6.76 \times 10^{20}\,\mathrm{cm} \tag{3.26}$$

We modeled the NE and SW lobes separately, using a broken power-law electron distribution identical to the Circinus lobes, by varying B and N such that we maintain energy equipartition and without exceeding the radio data points. Thereafter, we summed the SEDs of each lobe to obtain the final broadband emission model for the lobes of NGC 1068 shown in Figure 4.16 in Chapter 4.

3.4 Origin of the emission from the shocked region

One feature of the lobes of Circinus is the shocked regions or shells, similar to those found in SNRs. In SNRs, this emission is due to synchrotron emission. The typical width to radius ratio of SNR shocks is 0.1. In the case of Circinus, the observations show a 0.3 width to radius ratio (Mingo et al., 2012) which is similar to the SNR case.

We thus investigated the origin of this emission by testing if the expected width of the shocked lobe region due to synchrotron emission is consistent with the radio observations.

3.4.1 Width of the shocked region

The calculation of the width L of the shocked region of the lobes requires the electron energy E producing the synchrotron emission and the synchrotron loss time scale τ_{syn}.

Using Equation 3.27 (Ginzburg and Syrovatskii, 1965) we can estimate the characteristic frequency ν_{ch} of the maximum synchrotron emission from a relativistic electron with energy E in the presence of a magnetic field with strength B.

$$\nu_{ch} = 1.8 \times 10^{18} B_{\perp} \left(\frac{E}{1\,\mathrm{erg}} \right)^2 \mathrm{Hz} \tag{3.27}$$

where it can be estimated that $B_{\perp} \approx \sqrt{\frac{2}{3}} B$.

For this calculation, we use the best-fit magnetic field from the broadband emission modelling in Figure 4.14 in Chapter 4 to obtain $B_{\perp}$. We use a MeerKAT characteristic frequency $\nu_{meerkat} = 1$ GHz since non-thermal synchrotron emission dominates the radio spectrum at this frequency.

Using Equation 3.28 (Vink, 2012) we can estimate the radiative timescale τ_{syn}. The effective magnetic field in Equation 3.29 is considered to account for inverse Compton losses with $B_{rad} = 3.3\,\mu$G which is the magnetic field strength at which the magnetic field energy density is equal to the CMB radiation energy density. However in our model we account for contributions due to the ISRF (which included a high temperature u_{high} and low temperature component u_{low}) which has a significantly larger energy density compared to the CMB ($u_{cmb} = 0.24$ eV cm^{-3}). Hence we calculate B_{rad} from Equation 3.30 to account for losses due to the ISRF. Using the best-fit values of u_{low} and u_{high}, we obtain a value for B_{rad} and thus B_{eff}.

$$\tau_{syn} = 12.5 \left(\frac{E}{100\,\mathrm{TeV}} \right)^{-1} \left(\frac{B_{eff}}{100\,\mu\mathrm{G}} \right)^{-2} \mathrm{yr} \tag{3.28}$$

$$B_{eff}^2 = B_{rad}^2 + B_{\perp}^2 \tag{3.29}$$

$$\frac{B_{rad}^2}{8\pi} = u_{low} + u_{high} \tag{3.30}$$

Finally, once we obtain τ_{syn} from Equation 3.28 we can estimate the width of the shocked region by using $L = v \times \tau_{syn}$ where v is the speed of gas in the lobe edges. Mingo et al. (2012) report an expansion velocity of the gas in the lobes of Circinus of 900-950 km s^{-1}. The final results are shown in Equation 4.6 in Chapter 4.

3.5 Multi-wavelength analysis of SN1996cr

We also investigated the light curves of SN1996cr from MeerKAT radio and *Fermi*-LAT γ-ray observations.

3.5.1 Modelling the radio light curve

The radio light curve of SN1996cr can be used to study the stage at which the radio emission fades as the blastwave of the SN decelerates and the CSM density decreases.

We generated the light curve using the Chevalier model (Equation 2.1) discussed in Section 2.6.1. We take a similar approach to Meunier et al. (2013) using the same 1.4 GHz archival ATCA data from 1996 to 2011 but add on the MeerKAT flux of SN1996cr from 2018 to constrain the flux decline.

MeerKAT radio flux of SN1996cr

To obtain the MeerKAT radio flux of SN1996cr, we found the flux in the same manner as the lobe substructure of the elliptical beam enclosing SN1996cr in the 1375 MHz map. The small angular size of the SN relative to the angular resolution of MeerKAT meant we could consider it to be a point source. We then created an annulus region centred on the coordinates of Circinus and enclosing the elliptical regions to do an estimation of the background flux. The flux and background regions can be seen in Figure 3.12. The flux error is equal to the RMS since only a single beam was considered.

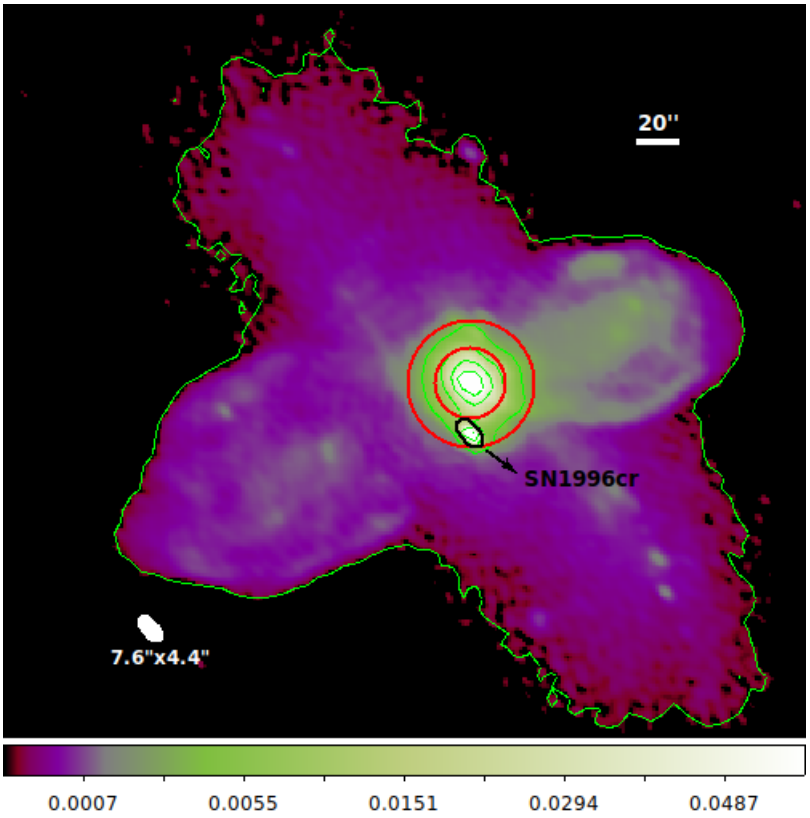

Figure 3.12: SN1996cr elliptical flux and annulus background regions outlined in the 1375±74.5 MHz MeerKAT radio map. The beam FWHM is shown in the bottom left of the image by the filled white circle. The image RMS is 9.03 μJy/beam. The contour levels are 0.0001, 0.0038, 0.0151, 0.0338, 0.06 μJy/beam.

$a(p,m)$ & $b(p,m)$ dependencies

In order to use the Chevalier model we require the forms of the temporal indices $a(p,m)$ and $b(p,m)$ of the radio flux density F in the early optically thick absorption phase and later optically thin emission phase respectively from Equation 3.31 (Nayana A. et al., 2018). Using the relations in Equation 3.32 (Chevalier, 1998) and the dependencies of R (radius of the forward shock), B (magnetic field strength) and N_0 (normalisation of the power-law energy distribution) on time for the four different models given by Chevalier (1996), we derived the forms of $a(p,m)$ & $b(p,m)$ shown in Table 3.4. In all four models it is assumed that $R \propto t^m$.

$$\begin{aligned} F &\propto t^{a} \text{ (optically thick medium)} \\ F &\propto t^{-b} \text{ (optically thin medium)} \end{aligned} \tag{3.31}$$

$$F \propto R^2 B^{-\frac{1}{2}} \text{ (optically thick medium)}$$
$$F \propto R^3 N_0 B^{\frac{p+1}{2}} \text{ (optically thin medium)} \tag{3.32}$$

Model	**Time dependencies**	$a(p,m)$	$b(p,m)$
1	$N_0 \propto t^{-2}$ $B \propto t^{-1}$	$F \propto R^2 B^{-\frac{1}{2}} \propto t^{2m} t^{\frac{1}{2}}$ $\Rightarrow a = 2m + \frac{1}{2}$	$F \propto R^3 N_0 B^{\frac{p+1}{2}} \propto t^{3m} t^{-2} t^{-\frac{p+1}{2}}$ $\Rightarrow b = \frac{p+5-6m}{2}$
2	$N_0 \propto t^{-2}$ $B \propto R^{-1} \propto t^{-1m}$	$F \propto R^2 B^{-\frac{1}{2}} \propto t^{2m} t^{\frac{m}{2}}$ $\Rightarrow a = \frac{5m}{2}$	$F \propto R^3 N_0 B^{\frac{p+1}{2}} \propto t^{3m} t^{-2} t^{-\frac{(p+1)m}{2}}$ $\Rightarrow b = \frac{4-(5-p)m}{2}$
3	$N_0 \propto R^{-2} \propto t^{-2m}$ $B \propto t^{-1}$	$F \propto R^2 B^{-\frac{1}{2}} \propto t^{2m} t^{\frac{1}{2}}$ $\Rightarrow a = 2m + 0.5$	$F \propto R^3 N_0 B^{\frac{p+1}{2}} \propto t^{3m} t^{-2m} t^{-\frac{p+1}{2}}$ $\Rightarrow b = \frac{p+1-2m}{2}$
4	$N_0 \propto R^{-2} \propto t^{-2m}$ $B \propto R^{-1} \propto t^{-m}$	$F \propto R^2 B^{-\frac{1}{2}} \propto t^{2m} t^{\frac{m}{2}}$ $\Rightarrow a = \frac{5m}{2}$	$F \propto R^3 N_0 B^{\frac{p+1}{2}} \propto t^{3m} t^{-2m} t^{-\frac{(p+1)m}{2}}$ $\Rightarrow b = \frac{(p-1)m}{2}$

Table 3.4: Derivation of $a(p,m)$ & $b(p,m)$ using the time dependencies by Chevalier (1996).

Next, we fit the Chevalier model (F_{model}) in Equation 2.1 to the ATCA and MeerKAT radio flux densities of SN1996cr (F_{data}) for all four forms of the temporal indices to find the best-fit $K1$, $K2$, p and m for each model. We test the model for two fitting methods:

1. χ^2 fit in which we minimise the function $\chi^2 = \dfrac{(F_{model} - F_{data})^2}{\sigma^2_{F_{data}}}$.
2. Least-squares fit in which we minimise the function $LS = (F_{model} - F_{data})^2$.

The χ^2 fit is thus weighted by the statistical uncertainty of the observed flux considered in the analysis. We initially performed these fits by freeing $K1$ & $K2$ and fixing p =3.1 and m =2/3, and thereafter freeing all four parameters. The typical range of m is between 2/3 and 1 (Chevalier, 1996) derived from models of the expansion of the blast wave. The range of p is between 2.4 and 3 derived from the typical spectral index range in synchrotron emission theory.

3.5.2 Modelling the γ-ray light curve

Modelling the γ-ray light curve is achieved using the results of the ten-year *Fermi*-LAT likelihood analysis of Circinus. This investigation into the GeV emission of

SN1996cr is motivated by the case of SN2004dj (Xi et al., 2020) in which its GeV light curve shows a flux decline with time, possibly corresponding to a dimming of the emission from the SN.

A possible flux decline with time is also observed in the GeV observations of Circinus. Guo and Mathews (2012) who used more data and an updated source model, reported a lower γ-ray luminosity compared to Hayashida et al. (2013). This behaviour could originate from the potential decline of the GeV flux of SN1996cr. However, in the 4FGL-DR2 source catalog and *Fermi*-LAT analyses of Circinus by other authors (Hayashida et al., 2013; Guo et al., 2019), the GeV light curve is assumed to be constant with time. We will thus test if the GeV *Fermi*-LAT data favours a flux decline model over a constant one.

To generate the GeV light curve, we performed a binned likelihood analysis of two-year time bins for the full ten years of data - totaling five intervals. The same likelihood routine was used as the ten-year run in each interval but with a new source model. The source model was set up such that 16 parameters were fixed at the global best-fit values from the ten-year run and the other fixed parameters were set at their values from the 4FGL-DR2 catalog. A total of 20 spectral parameters were freed such that:

- The normalisation value of all sources within 3° of Circinus was fixed at the output of v9 (Section 3.2.2) along width the Index1 and Expfactor parameter of the pulsar 4FGL J1356.9-6432 and the galactic background.
- The normalisations of all variable sources (sources with $TS_{Var} > 21.67$ consistent with 4FGL-DR2) within the ROI (15°) were freed.
- The normalisation of Circinus was freed.
- The normalisation of the isotropic background was freed.

Given that *Fermi*-LAT has a differential sensitivity peak in the 1 to 10 GeV range, we decided to increase the minimum energy to 1 GeV to compute the light curve. Convergence was achieved when using the NEWMINUIT fit algorithm applied above 1 GeV for the 20 free parameters explained above.

Using the flux value (above 1 GeV) output from each time interval of the likelihood analysis, we obtained the GeV light curve of Circinus (Figure 4.29 in Chapter 4). We then fitted this data to a constant ($F(t) = C1$) and a decline ($F(t) = C2/t$) model and evaluated the models with a χ^2 test to see if the decline model is favoured.

A decline model would support the hypothesis that the *Fermi* GeV emission of Circinus originates from SN1996cr.

Chapter 4

Results

4.1 Results of MeerKAT observations

4.1.1 Spatial analysis

In this section, we report a spatial analysis identifying structures from the MeerKAT image of Circinus and we compare it with data at other wavebands. For this spatial analysis, we used the 1.375 GHz WSClean radio image from a 149 MHz band shown in Figure 4.1.

Comparisons between MeerKAT and ATCA observations of Circinus

The proposed geometry of Circinus by Elmouttie et al. (1998a) from ATCA observations (Figure 2.10 in Chapter 2) includes an unresolved core surrounded by a diffuse radio starburst ring and radio lobes which are approximately 1.5 kpc in length. In this picture, the lobes consist of a plume or 'cocoon' surrounded by a brightened edge. The same structures appear in the ATCA radio map (Figure 3.1 in Chapter 3) produced by Mingo et al. (2012). The morphology extracted from the MeerKAT image and the ATCA images is similar with both observations showing a bright core region, a visible radio galactic disk, radio lobes oriented in the north-western and south-eastern direction and bright star-forming regions at similar locations such as those observed in the southern part of the disk. The diffuse radio starburst ring is not detected at this central frequency with MeerKAT.

There are no significant new features observed with MeerKAT. However, MeerKAT

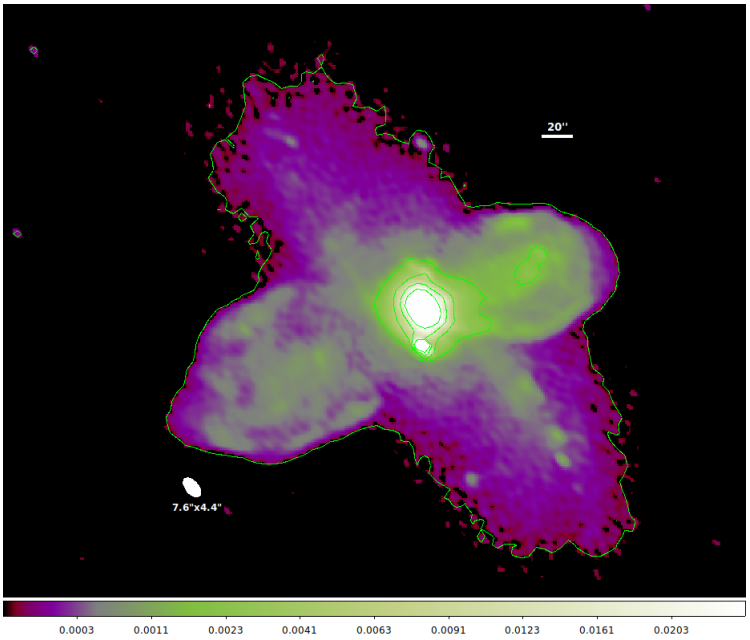

Figure 4.1: 1.375 GHz MeerKAT radio map of Circinus at a 149 MHz bandwidth with a 7.6×4.4 arcsec^2 beam (shown in the bottom left of the image) obtained using 60 antennas. The map is in units of Jy/beam with a scale of 1 px $\sim$ 1.3 arcsec. The image RMS is 9.03 μJy/beam. The contour levels are 0.0001, 0.0017, 0.0063, 0.1411, 0.0250 μJy/beam.

provides deeper and more sensitive images compared to the ATCA ones. The superiority of the MeerKAT images enables more clear identification of the regions of different brightness. To demonstrate this we can consider the ATCA radio contour maps of Circinus in Figures 4.2 and 4.3 from Elmouttie et al. (1998a). These maps are in the same radio band as the MeerKAT observations. The ATCA map in Figure 4.2 shows large scale emission, but this image is at a lower resolution compared to the MeerKAT image. The map with the smaller beam size (Figure 4.3) has a higher resolution than the first, but the larger scale emission is not visible and the sensitivity to fainter emission is reduced. Hence the MeerKAT observations provide the full extent of the radio lobe emission and at a higher resolution.

Similarities between the lobes of Circinus and the Fermi bubbles

From the MeerKAT image in Figure 4.4 we identified the bright, thin regions along the edges of the lobes, to demonstrate the edge brightening effect. The localisation of these regions is more precise compared to previous ATCA observations of Circinus such as the ATCA image in Figure 3.1 (Mingo et al., 2012) (Chapter 2) since MeerKAT observations offer a higher sensitivity at a finer angular resolution to produce sharper images.

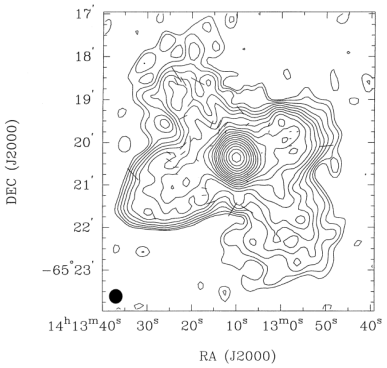

Figure 4.2: 1.499 GHz ATCA radio contour map with a 20×19 arcsec^2 spatial resolution (Elmouttie et al., 1998a).

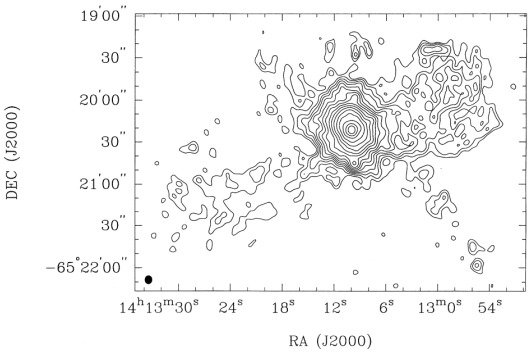

Figure 4.3: 1.499 GHz ATCA radio contour map with a 6.0×5.4 arcsec^2 spatial resolution (Elmouttie et al., 1998a).

This edge-brightening effect has also been observed in the Fermi bubbles [e.g., Jones et al. (2012)]. This can be seen in Figure 2.20 in Chapter 2 which shows the ROSAT X-ray image superimposed over a γ-ray map featuring the Fermi bubbles. The edges of the bubbles line up with features in the X-ray maps and are usually interpreted as shock waves. Chandra observations of Circinus by Mingo et al. (2012) also confirm the presence of the X-ray counterpart to the brightened radio edges observed with ATCA.

We identified the plume structures as the brightest regions inside each lobe from the MeerKAT image in Figure 4.5. These plumes can be compared to similar regions of enhanced γ-ray emission found in the Fermi bubbles, identified as 'cocoons' by Ackermann et al. (2014) shown in Figure 2.18 in Chapter 2. This γ-ray excess is more pronounced in the south-east region of the bubbles. They did investigate the possibility of a jet origin for the cocoons but did not find sufficient supporting evidence (Su and Finkbeiner, 2012).

4.1.2 RMS results

Table 4.1 shows the primary-beam uncorrected RMS and MAD values for the 1375±74.5 MHz map of the selected regions, discussed in Section 3.1.4 in Chapter 3, after exclusion of sources with a significance greater than 5σ. The RMS values shown in the last column of Table 4.2 is an average of the RMS of the red, blue and green regions for each MeerKAT radio map.

The smallest RMS value (9.03 μJy/beam) is for the 1375±74.5 MHz, which has the largest bandwidth.

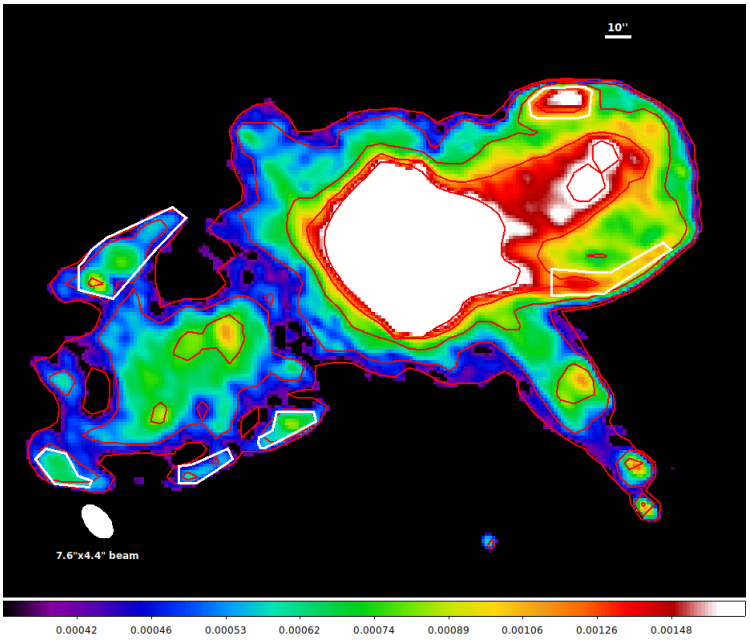

Figure 4.4: 1.375 GHz MeerKAT radio map of Circinus with edge-brigthened regions outlined (white). The image RMS is 9.03 μJy/beam with a 7.6×4.4 arcsec^2 beam (shown in the bottom left of the image). The contour levels are 0.00041, 0.00049, 0.00074, 0.0012, 0.0017 μJy/beam.

Region	**RMS (μJy/beam)**	**MAD (μJy/beam)**
Red	9.1	5.8
Blue	9.3	6.1
Green	8.7	5.6
Cyan	12.0	8.1
Magenta	13.4	8.2

Table 4.1: RMS and MAD values for the five regions in the WSClean 1375 MHz radio map.

4.1.3 Flux results

The flux density values obtained from the MeerKAT observations for each region within each lobe of Circinus are shown in Table 4.3. I calculated the associated errors of the flux density for the MeerKAT radio maps using the procedure described in Section 3.1.4 in Chapter 3. The flux density error calculation is demonstrated for the 1375±74.5 MHz map in Table 4.4.

From these results, we notice a general drop in flux with an increase in central frequency as expected. The RMS value is inversely proportional to the bandwidth ($\propto \frac{1}{\sqrt{\Delta\nu}}$). We thus expect the 10 MHz bandwidth errors to be 3.9 times larger than the 149 MHz bandwidth map ($\frac{1}{\sqrt{10\text{MHz}}}/\frac{1}{\sqrt{149\text{MHz}}} = 3.90$) which is similar to what we see when comparing the flux errors between the two 1375 MHz maps.

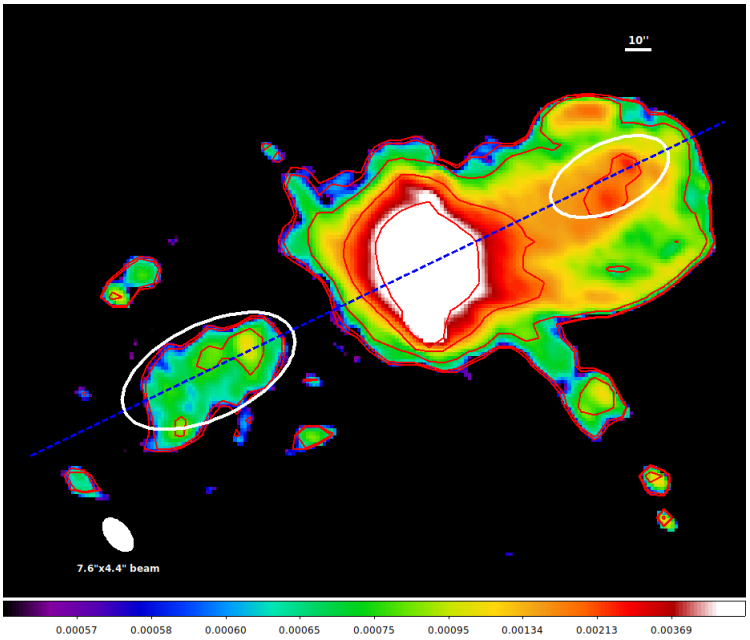

Figure 4.5: 1.375 GHz MeerKAT radio map of Circinus with plumes outlined (white). The image RMS is 9.03 μJy/beam with a 7.6×4.4 arcsec^2 beam (shown in the bottom left of the image). The contour levels are 0.00056, 0.00059, 0.00075, 0.0017, 0.0068 μJy/beam.

Map frequency (MHz)	**RMS (μJy/beam)**
1030 ± 5	92.24
1375 ± 5	51.12
1020 ± 56.5	43.62
1380 ± 71	18.21
1375 ± 74.5	9.03

Table 4.2: RMS values for the MeerKAT radio maps.

MeerKAT results compared to ATCA results

Table 4.5 compares our higher frequency MeerKAT flux density measurements of the lobe substructure to the 20cm (1 499 MHz) ATCA observations (Mingo et al., 2012). The MeerKAT measurements are compatible with the ATCA observations and the drop in flux with frequency is still observed. The only exception is the southern hotspot which remains fairly constant across these frequencies. It is also clear that the errors on the MeerKAT flux measurements are between one to two orders of magnitude smaller than the ATCA observations demonstrating the superiority of the MeerKAT observations of Circinus. The MeerKAT measurements of the flux of the shells are larger than the lobes and this is different to the ATCA measurements in which the lobes and shells are very similar in flux. This difference in flux can

Region		1020±56.5 MHz (mJy)	1030±5 MHz (mJy)	1375±74.5 MHz (mJy)	1375±5 MHz (mJy)	1380±71 MHz (mJy)
Hotspots	South	24.398 ± 0.069	23.759 ± 0.155	21.417 ± 0.030	20.227 ± 0.109	20.135 ± 0.039
	North	41.138 ± 0.061	40.607 ± 0.137	37.161 ± 0.026	34.775 ± 0.096	35.182 ± 0.034
Lobes	South	56.090 ± 0.123	53.902 ± 0.278	47.558 ± 0.053	45.755 ± 0.196	45.978 ± 0.069
	North	48.177 ± 0.076	48.218 ± 0.174	40.862 ± 0.033	40.69 ± 0.122	39.203 ± 0.043
Shells	South	67.296 ± 0.155	66.563 ± 0.350	61.029 ± 0.067	58.677 ± 0.246	57.746 ± 0.087
	North	57.497 ± 0.109	55.254 ± 0.247	50.013 ± 0.047	46.129 ± 0.173	48.162 ± 0.061

Table 4.3: MeerKAT flux density measurements at different central frequencies and bandwidths for the lobe structure of Circinus.

Region		n (number of pixels)	$Area_{region}$ (arcsec^2)	N (number of beams)	$\Delta Flux$ (μJy/beam)
Hotspots	South	697	1177.93	11.05	30.02
	North	538	909.22	8.52	26.36
Lobes	South	2207	3729.83	34.98	53.41
	North	856	1446.64	13.56	33.25
Shells	South	3513	5396.97	55.68	67.38
	North	1744	2947.36	27.64	47.47

Table 4.4: Quantities required to compute the flux errors of each region demonstrated for the 1375±74.5 MHz map.

be accounted for by MeerKAT's ability to distinguish the differences in brightness between these two regions more clearly than ATCA does.

Region		1375±74.5 MHz (mJy)	1375±5 MHz (mJy)	1380±71 MHz (mJy)	1 499 MHz ATCA (mJy)
Hotspots	South	21.417 ± 0.030	20.227 ± 0.109	20.135 ± 0.039	20.9 ± 3.3
	North	37.161 ± 0.026	34.775 ± 0.096	35.182 ± 0.034	29.0 ± 2.0
Lobes	South	47.558 ± 0.053	45.755 ± 0.196	45.978 ± 0.069	37.2 ± 3.9
	North	40.862 ± 0.033	40.69 ± 0.122	39.203 ± 0.043	35.3 ± 2.6
Shells	South	61.029 ± 0.067	58.677 ± 0.246	57.746 ± 0.087	37.6 ± 4.8
	North	50.013 ± 0.047	46.129 ± 0.173	48.162 ± 0.061	36.9 ± 3.3

Table 4.5: Higher frequency MeerKAT flux measurements for the lobe structure of Circinus compared to 20cm (1 499 MHz) ATCA observations by Mingo et al. (2012).

4.1.4 Spectral analysis

The final spectral index map using the 1020 MHz and 1380 MHz MeerKAT data is shown in Figure 4.6 in which the maps are colvolved with a 5×5 pixel^2 Gaussian beam to observed the extended structure better. Figure 4.7 shows the spectral index map at the maximum spatial resolution (resolution equivalent to the beam of the 1020 MHz map without any convolution applied.)

We also computed the 1030-1375 MHz and 1020-1380 MHz spectral index of the hotspots, lobes and shells using the same Mingo et al. (2012) templates to compare to their spectral index analysis shown in Table 4.6.

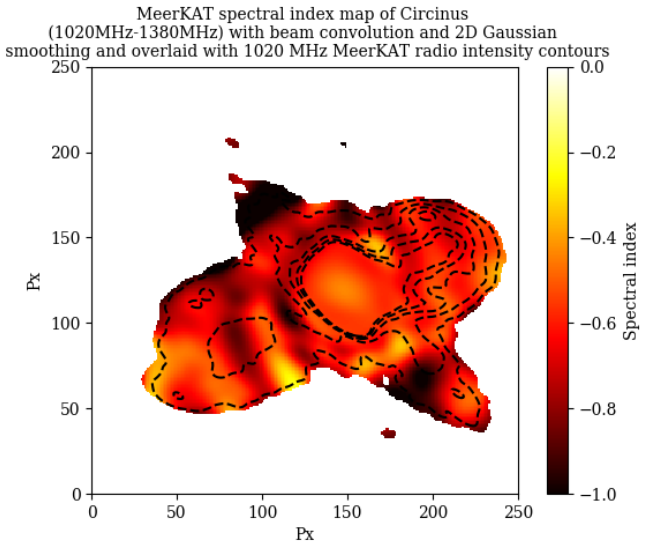

Figure 4.6: Two-point spectral index map of Circinus using the 1020 MHz and smoothed 1380 MHz MeerKAT data with a 2D Gaussian convolution overlaid with 1020 MHz MeerKAT radio intensity contours (0.0001, 0.0037, 0.0050, 0.0072, 0.0090 μJy/beam).The image RMS is 43.62 μJy/beam.

Region		**1030 MHz - 1375 MHz**	**1020 MHz - 1380 MHz**	**1499 MHz - 2300 MHz (Mingo et al. (2012))**	**2300 MHz - 5000 MHz (Mingo et al. (2012))**
Hotspots	SE	0.56 ± 0.03	0.64 ± 0.01	0.60±0.13	0.96±0.07
	NW	0.54 ± 0.02	0.52 ± 0.01	0.62±0.09	0.59±0.05
Lobes	SE	0.57 ± 0.02	0.66 ± 0.01	0.78±0.16	0.97±0.09
	NW	0.60 ± 0.02	0.68 ± 0.01	0.71±0.06	0.77±0.11
Shells	SE	0.44 ± 0.02	0.51 ± 0.01	0.84±0.20	1.12±0.12
	NW	0.63 ± 0.02	0.59 ± 0.01	0.70±0.13	0.94±0.08

Table 4.6: MeerKAT spectral index measurements for the lobe structure of Circinus compared to the ATCA spectral indices by Mingo et al. (2012).

In Mingo et al. (2012) the spectral indices are reported from the 2300 & 1499 MHz (13 & 20 cm) and 5000 & 2300 MHz (6 & 13 cm) data. We compare our results to their spectral indices for the 2300 & 1499 MHz ATCA data since their other two-point spectral indices are at much higher frequencies than the MeerKAT measurements. Their index values are softer for the lobes and shells. The MeerKAT observations show a fairly uniform spectral index distribution within each lobe in both sets of maps, relative to ATCA. This unformity in spectral index across the lobe is also reflected in the spectral index map in Figure 4.6, but with a possible soft index in the region of the southern hotspot.

Combining the ATCA and MeerKAT results, we note that there is a spectral steepening of the lobes and shells with frequency. The spectral indices of the hotspots do not seem to follow this trend, with the northern hotspot not changing significantly in value across the frequencies.

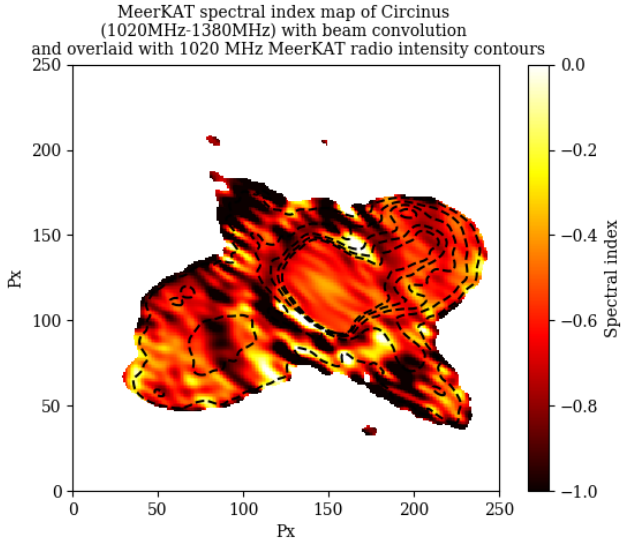

Figure 4.7: Two-point spectral index map of Circinus using the 1020 MHz and smoothed 1380 MHz MeerKAT data overlaid with 1020 MHz MeerKAT radio intensity contours (0.0001, 0.0037, 0.0050, 0.0072, 0.0090 μJy/beam).The image RMS is 43.62 μJy/beam.

4.2 *Fermi*-LAT likelihood analysis - 10 years

In Section 3.2.2 we discussed the different iterations of the likelihood analysis we performed on the full ten-year data set, shown in Table 3.2. We analyse each approach by considering the following:

- The effect of the number of free parameters on the results (column 2 of Table 4.7).
- The minimum energy as e_{min} (column 3 of Table 4.7).
- How the best-fit flux of Circinus (F_{output}) compares to the value obtained by Guo et al. (2019) (F_{Guo}) as $\sigma_{flux} = \frac{|F_{Guo} - F_{output}|}{\Delta F_{output}}$ (column 4 of Table 4.7).
- The TS value for the best-fit flux of Circinus (column 5 of Table 4.7).
- The relative difference between the observed and model counts as $\sigma_{Counts_{model}} = \frac{|\sigma_{Counts_{observed}} - \sigma_{Counts_{model}}|}{\sigma_{Counts_{observed}}}$ (column 6 of Table 4.7).
- Comparing the free parameter output values to their values in the 4FGL-DR2 catalog including the best-fit normalisations of the galactic background and isotropic backgrounds.

Version	**Number of free parameters**	e_{min} (GeV)	σ_{flux}	**TS**$_{flux}$	$\sigma_{Counts_{model}}$
v1	16	0.1	0.30	83.15	6.26×10^{-4}
v2	51	0.1	0.77	91.15	6.70×10^{-4}
v3	47	0.1	0.31	82.56	1.58×10^{-4}
v4	16	1.0	0.39	78.25	3.40×10^{-4}
v5	15	0.1	3.34	35.92	3.38×10^{-2}
v6	14	0.1	9.38	6.50	6.89×10^{-2}
v7	18	0.1	2.89	7.03	6.87×10^{-2}
v8	20	0.1	0.03	78.40	6.56×10^{-4}
v9	18	0.1	0.04	78.41	6.54×10^{-4}

Table 4.7: Summary of results from all nine approaches of the binned likelihood analysis over the full ten years.

We summarise our assessment of all the binned likelihoods below:

- Comparing v1 and v2 we found that increasing the number of free parameters for the same sources produces fits that are closer to the 4FGL-DR2 catalog.

- In v3 we freed the normalisation parameter within 5 degrees of Circinus (as opposed to 3 degrees in v1 and v2) and found that this produces fits closer to the 4FGL-DR2 catalog and reduces the discrepancy between the observed and model counts significantly.
- The consideration of a higher e_{min} in v4 produces the closest fits to the 4FGL-DR2 catalog including the normalisations of the two diffuse backgrounds.
- Fixing the normalisation of the diffuse backgrounds to a value of 1.0 (as given by the 4FGL-DR2 catalog) results in a significant overproduction of counts in the model compared to what is observed, evident in v5, v6 and v7.
- The normalisation of the galactic background drops from 1.0 to ∼0.89 when left free, and the normalisation of the isotropic background increases from 1.0 to ∼1.3-1.4 when left free in all cases.
- Freeing the parameters of the pulsar 4FGL J1356.9-6432 in v8 and v9 produces the closest match in flux to Guo et al. (2019).

Based on this assessment, we identified v9 as one of the best approaches given the relatively small number of free parameters and the consistency between the numbers of observed and modeled gamma-ray counts.

The v9 binned likelihood outputs the values in Table 4.8 for Circinus identified as 4FGL J1413.1-6519 in the catalog.

Normalisation	1.20 ± 0.18
Index	2.26
Scale	3106.58
TS value	78.41
Flux (>0.1 GeV)	$(9.45 \pm 1.40) \times 10^{-9}$ photons/cm^2/s

Table 4.8: v9 binned likelihood output for Circinus.

The flux is obtained for a minimum energy of 0.1 GeV. Assuming a photon index of 2.26 as fixed in the analysis we calculate the flux above 1 GeV in Equation 4.1 by extrapolating the power-law.

$$F(>1\,\mathrm{GeV}) = F(>0.1\,\mathrm{GeV}) \times \left(\frac{0.1\,\mathrm{GeV}}{1.0\,\mathrm{GeV}}\right)^{2.26-1.0} = (5.19 \pm 0.77) \times 10^{-10}\,\mathrm{photons/cm^2/s} \tag{4.1}$$

This value is compatible with the 4FGL-DR2 flux of (5.65±0.76) $\times 10^{-10}$ photons/cm^2/s and the Guo et al. (2019) flux of (5.90±1.04) $\times 10^{-10}$ photons/cm^2/s.

4.3 Broadband emission modelling

4.3.1 Case 1

In the first case of the broadband emission modelling of the Circinus lobes, we only considered contributions from the CMB for the IC emission. Table 4.9 shows how the parameters used in our broadband emission model compares to the broadband emission modelling of the Circinus lobes by Hayashida et al. (2013) and the Fermi bubbles by Kataoka et al. (2018). Our choice of γ_{break} is based on the age of the lobes (Mingo et al., 2012) assuming the age of the lobes is equal to the lifetime of synchrotron electrons. This value is similar to the value used by Kataoka et al. (2018). Using the values reported in Table 4.9 with a best-fit N value of 1.5×10^{-10} cm^{-3} and maintaining energy equipartition, we get a final SED model shown as the green curve in Figure 4.8.

Parameter	**Our model**	**Hayashida et al. (2013)**	**Kataoka et al. (2018)**
B (μG)	3.5	5.0 - 10.0	12.0
γ_{min}	2.0 $\times 10^3$	1.0	2.0×10^3
γ_{max}	1.0×10^8	1.0×10^6	1.0×10^8
γ_{break}	5.0×10^6	-	1.0×10^6

Table 4.9: Comparison of input parameters used in the broadband emission modelling of the lobes of Circinus and the Fermi bubbles.

Our curve differs from the one by Hayashida et al. (2013) for two reasons:
a) The synchrotron peak is higher than the inverse Compton one.
b) Our peaks are sharper.

For case (a) further raising the inverse Compton peak relative to the synchrotron peak involves increasing the number of electrons (N) or decreasing the magnetic field strength (B). Both these operations will lead to a higher $\frac{U_e}{U_B}$ ratio and thus a non-equilibrium state. Further, the B value we use is already smaller than the minimum value used by Hayashida et al. (2013) . Therefore, we cannot decrease B any further.

For case (b) we suspect that the curves by Hayashida et al. (2013) are rounded most likely because the authors used a smooth broken power-law electron distribution

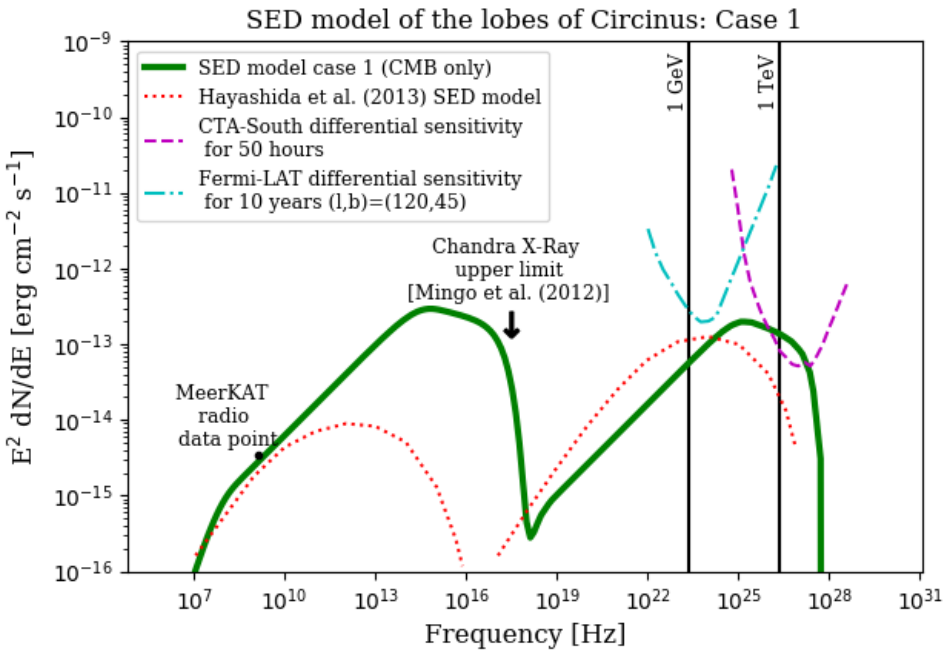

Figure 4.8: Case 1 SED model (green curve) compared with Hayashida et al. (2013) (red curve).

(also done by Kataoka et al. (2018)). Given that the SSC/EC simulator defines the broken power-law distribution with a sharp break and a sharp cut-off as in Equation 3.12 in Chapter 3, it is clear that the results from the SSC/EC simulator show relatively sharp spectral features.

Enhancing VHE emission

We then investigated enhancing the VHE flux to increase the chances of detection by the VHE instruments. The approach we took included fixing B=3.5 μG & N=1.5 $\times$ 10^{-10} cm^{-3} and varying γ_{break} between 4.0$\times$10^6 and 7.0$\times$10^6 shown in Figure 4.9. We found that increasing γ_{break} enhances the VHE flux, but all values beyond 4.0$\times$10^6 (green dotted curve) produce curves that exceed the Chandra X-ray upper limit.

To study this enhancement further we considered the effect an increasing γ_{break} has on the H.E.S.S. exposure time required for a 5σ detection. Using the SED models from Figure 4.9 for each γ_{break} the corresponding photon index and normalisation at 1 TeV is extracted from the power-law fit. The index and normalisation are used

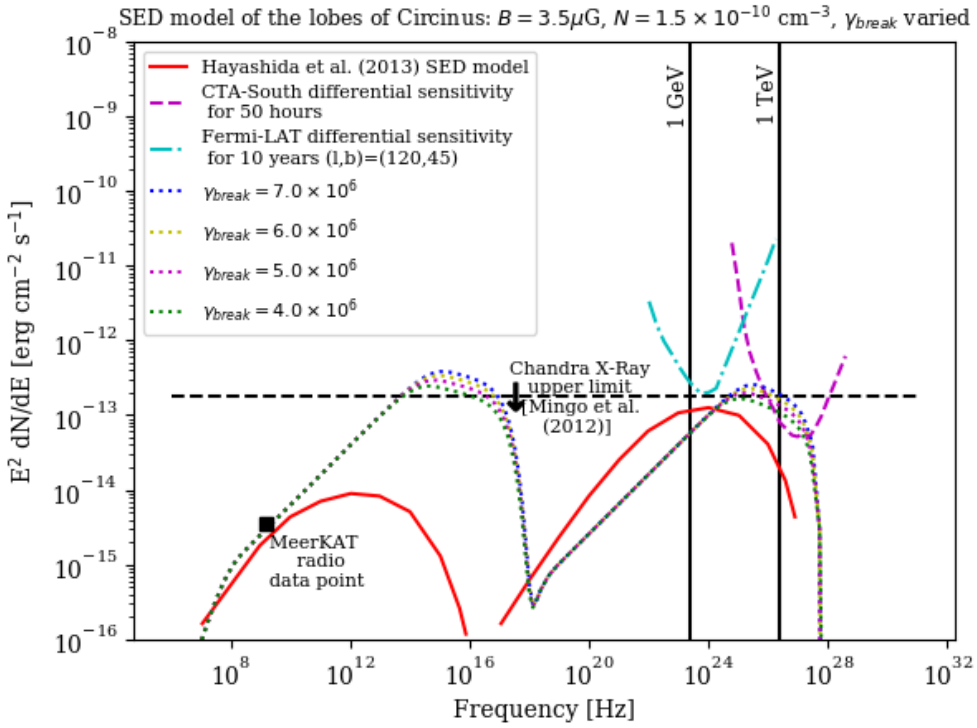

Figure 4.9: SED model with γ_{break} varied and B=3.5 μG & N=1.5×10^{-10} cm^{-3}.

as inputs into the HESSII_neededTime_new code [1] which outputs the observation time needed by H.E.S.S. for a 5σ detection. The result can be seen in Figure 4.10 which shows that at larger γ_{break} values less observation time is required to make a detection due to an enhanced VHE signal. H.E.S.S. observations can thus be used to constrain the break in the electron spectrum. Section 4.6.4 discusses the scientific case for H.E.S.S. observations further.

Power-law fit

We also performed a power-law fit on the γ-ray SED, in the 0.3-3.0 TeV range for the case: B=3.5μ G, γ_{break}=7.0×10^6 (in which the VHE flux was a maximum) and N=1.5×10^{-10} cm^{-3}. This yielded a fit of dN/dE=1.18×10^{-25} eV^{-1} cm^{-2} s^{-1}(E/TeV)$^{-2.22}$ which is shown as the red line in Figure 4.11.

[1] Created by Carlo Romoli and available on the H.E.S.S. confluence pages

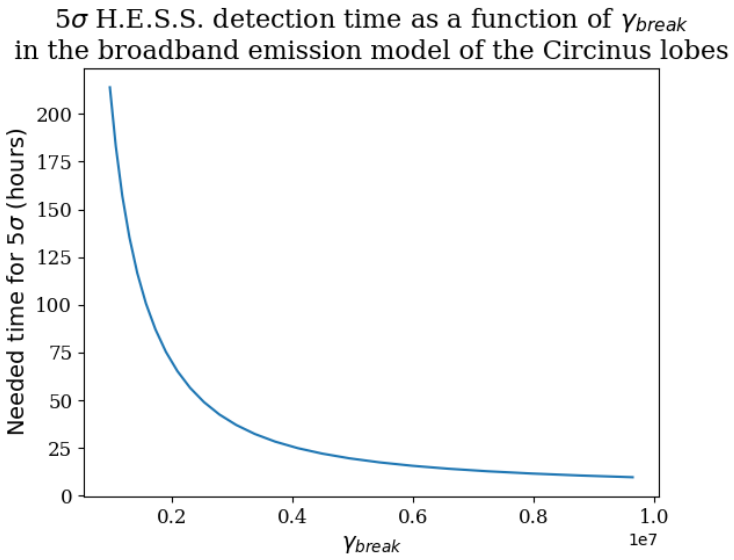

Figure 4.10: 5σ H.E.S.S. detection time as a function of γ_{break}.

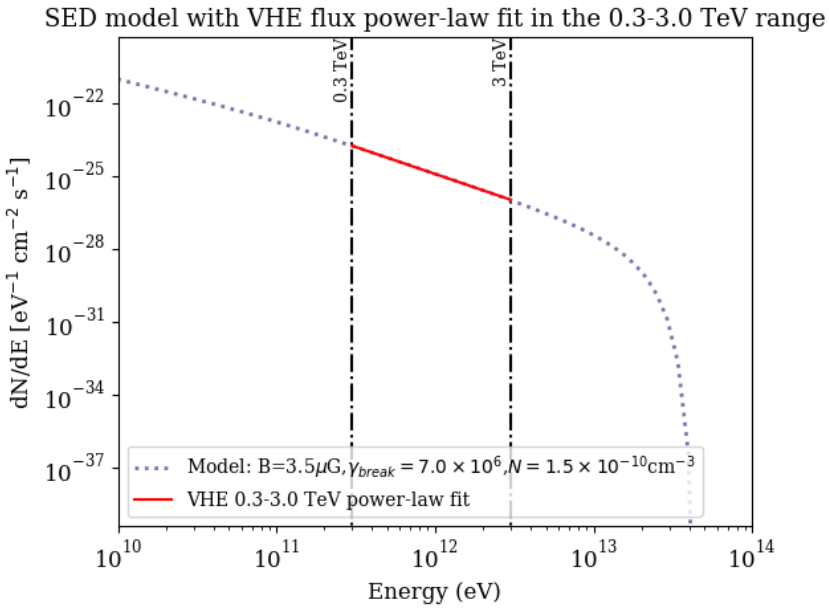

Figure 4.11: SED model (B=3.5 μG, γ_{break}=7.0×10^6 & N=1.5×10^{-10} cm^{-3}) of the VHE flux with a power-law fit (red curve) between 0.3-3.0 TeV.

4.3.2 Case 2

In the second case, we considered contributions from the external photon fields for the inverse Compton emission. Table 4.10 shows the best-fit parameters between the ISRF at the positions of the radio lobes in the Circinus galaxy, as discussed in Section 3.3.5, and how it compares to the values at position of the solar system ($R = 6.25$ kpc, $z = 0.0$ kpc).

Parameter	**Lobes of Circinus**	**Solar system**
T_{low} (K)	43.56	32.44
u_{low} (eV cm^{-3})	0.90	0.80
T_{high} (K)	5.69 $\times 10^3$	3.86 $\times 10^3$
u_{high} (eV cm^{-3})	8.70	0.68

Table 4.10: Best-fit temperature and energy density for the ISRF components for the lobes of the Circinus and the solar system.

Figures 4.12 and 4.13 show the blackbody spectrum fit (blue) of the GALPROP ISRF model (red) for the high-temperature and low-temperature component respectively from which the best-fit temperature and energy density was obtained.

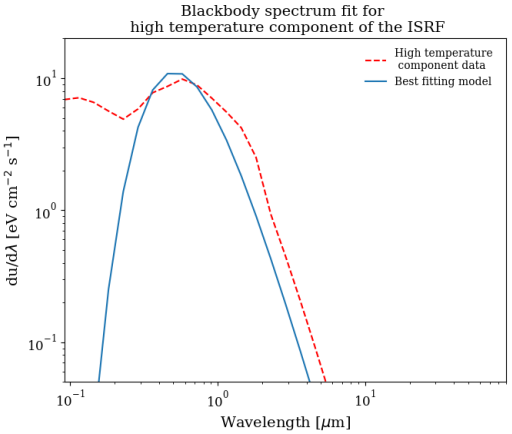

Figure 4.12: Blackbody spectrum fit for the high-temperature radiation field.

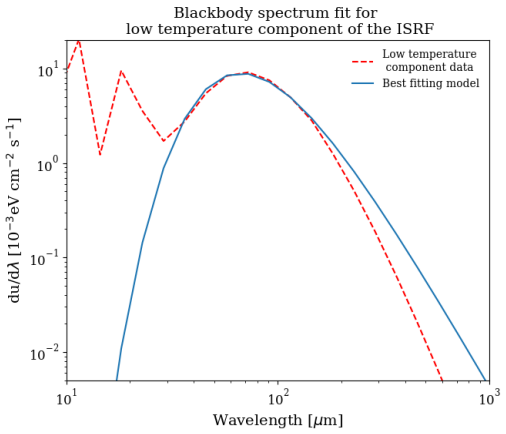

Figure 4.13: Blackbody spectrum fit for the low-temperature radiation field.

From these results, we notice that the energy density of the lower temperature component is similar ($\sim$1 eV cm^{-3}) for both the Circinus lobes and the solar system. However, the energy density of the higher temperature component is larger by at least a factor of 10 at the positions of the radio lobes in the Circinus galaxy compared to the solar system.

We used these values as inputs for the Naima code to output the resultant SED shown as the green curve in Figure 4.14. Including these external fields significantly enhances the VHE emission. In both case 1 and case 2 the lobes are unlikely to

be detected by Fermi-LAT, but there is significant potential for detection by CTA-South in the second case. The preliminary H.E.S.S. upper limit has been added to the SED for comparison and is discussed in Section 4.6.4.

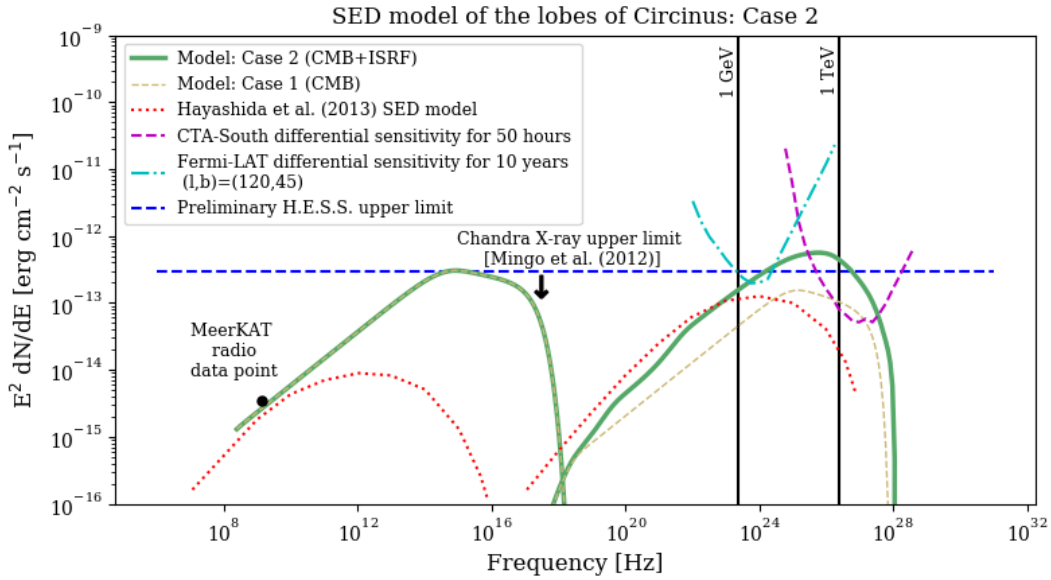

Figure 4.14: SED of the case 2 model which includes the CMB and ISRF seed photons for inverse Compton emission.

Power-law fit

We also found the power-law fit for dN/dE in the energy range of 0.2-5.0 TeV. This energy range is determined by the upper and lower energy bounds for Circinus to be detected by the High Energy Stereoscopic System (H.E.S.S.) - an array of Cherenkov telescopes. The lower energy bound of H.E.S.S. is $\sim$ 0.35 TeV and is calculated assuming a zenith angle of Circinus $\sim 40°$ (equal to the difference between the declination of Circinus (65° south) and the latitude of the telescope (23° south)). The upper bound is calculated using the fact that Circinus is a faint source and the statistics are probably small beyond 5.0 TeV. The power-law fit we get is given by Equation 4.2 and is shown in Figure 4.15.

$$\left.\frac{dN}{dE}\right|_{0.2\,\mathrm{TeV}}^{5.0\,\mathrm{TeV}} = 2.5 \times 10^{-25}\,\mathrm{cm}^{-2}\,\mathrm{s}^{-1}\,\mathrm{eV}^{-1} \times \left(\frac{E}{\mathrm{TeV}}\right)^{-2.34} \tag{4.2}$$

$$\frac{dN}{dE}(@E = 1\,\mathrm{TeV}) = 2.5 \times 10^{-25}\,\mathrm{cm}^{-2}\,\mathrm{s}^{-1}\,\mathrm{eV}^{-1} \times \left(\frac{1\,\mathrm{TeV}}{\mathrm{TeV}}\right)^{-2.34} = 2.5 \times 10^{-25}\,\mathrm{cm}^{-2}\,\mathrm{s}^{-1}\,\mathrm{eV}^{-1}$$
$$\approx 2.5 \times 10^{-13}\,\mathrm{cm}^{-2}\,\mathrm{s}^{-1}\,\mathrm{TeV}^{-1} \tag{4.3}$$

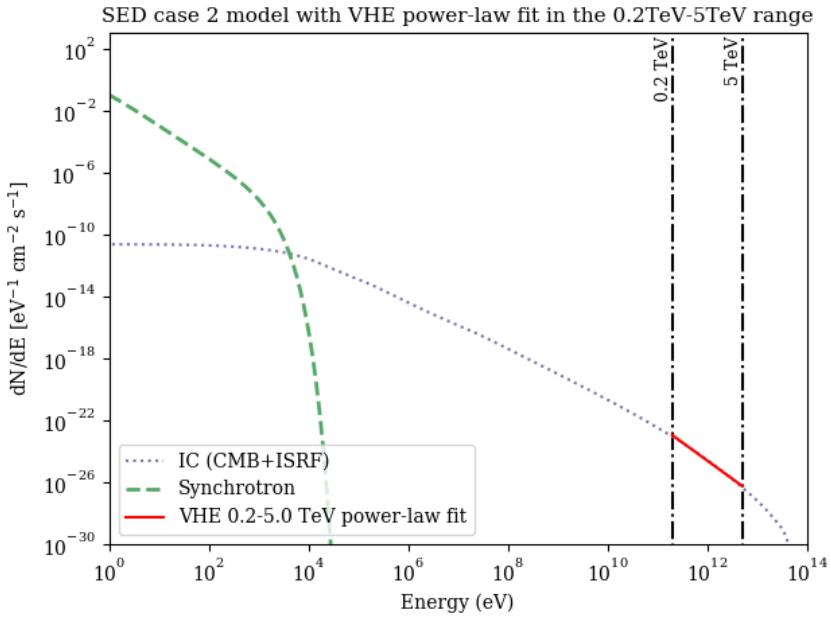

Figure 4.15: Case 2 power-law fit in the 0.2-5.0 TeV range.

Modern imaging atmospheric telescope arrays, such as H.E.S.S., can test the very high energy γ-ray signals with fluxes similar to those estimated in this MSc thesis. However, deep observations with an exposure >100 hours will be needed, such as those which were required for a detection of NGC 253 (H. E. S. S. Collaboration et al., 2018).

Both cases considered for the Circinus lobes show an unlikely detection by *Fermi*-LAT but significant potential for detection by CTA-South. CTA-South will be capable of close to 1 arcmin angular resolution for energies above 1 TeV (Cherenkov Telescope Array Consortium et al., 2019). This resolution could facilitate in locating where exactly the VHE γ-ray emission of Circinus is coming from and possibly better understand the nature of its lobes.

4.3.3 NGC 1068

Applying a similar technique to the lobes of NGC 1068 we obtained the following ISRF parameters:

- T_{low} = 45.3 K
- u_{low} = 13.2 eV cm^{-3}
- T_{high} = 5.51 $\times 10^3$ K
- u_{high} = 11.9 eV cm^{-3}

Modelling the lobes

The following best-fit parameters were found for each lobe in the SED modelling:

1. NE Lobe: B=87 μG, N=1.285$\times 10^{46}$ cm^{-3} 1/eV, $\frac{u_e}{u_B} = 1.01$
2. SW Lobe: B=44 μG, N=1.510$\times 10^{46}$ cm^{-3} 1/eV, $\frac{u_e}{u_B} = 1.00$

The final SED, equal to the sum of the SEDs of both lobes, is shown as the green curve in Figure 4.16. In this case, we also notice a significant increase in VHE emission by including the ISRF contributions.

Power-law fit

We also performed a power-law fit in the 0.25-5.0 TeV range for the combined SED of both lobes shown in Figure 4.17 and obtained the fit shown in Equation 4.4:

$$\left.\frac{dN}{dE}\right|_{0.25\,\mathrm{TeV}}^{5.0\,\mathrm{TeV}} = 1.55 \times 10^{-25}\,\mathrm{cm^{-2}\,s^{-1}\,eV^{-1}} \times \left(\frac{E}{\mathrm{TeV}}\right)^{-2.36} \tag{4.4}$$

$$\begin{aligned}\frac{dN}{dE}(@E = 1\,\mathrm{TeV}) &= 1.55 \times 10^{-25}\,\mathrm{cm^{-2}\,s^{-1}\,eV^{-1}} \times \left(\frac{1\,\mathrm{TeV}}{\mathrm{TeV}}\right)^{-2.36} = 1.55 \times 10^{-25}\,\mathrm{cm^{-2}\,s^{-1}\,eV^{-1}} \\ &\approx 1.55 \times 10^{-13}\,\mathrm{cm^{-2}\,s^{-1}\,TeV^{-1}}\end{aligned} \tag{4.5}$$

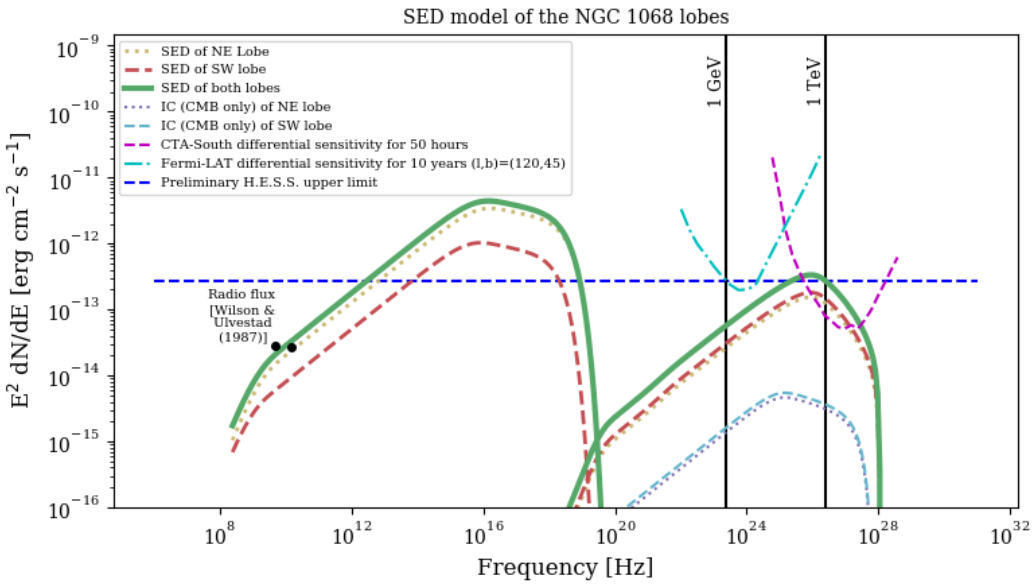

Figure 4.16: Case 2 SED model for the NGC 1068 lobes.

4.4 Origin of the emission from the shocked region

4.4.1 Synchrotron cooling timescale approach

We calculate the width of the shocked region or "shell" due to synchrotron radiation using the method outlined in Section 3.4. We begin by obtaining a $B_{\perp} = 3.67\,\mu$G derived from the best-fit magnetic field $B = 4.5\,\mu$G (from the broadband emission modelling in Figure 4.14). For this $B_{\perp}$ and the characteristic MeerKAT frequency $\nu_{meerkat} = 1$ GHz, using Equation 3.27 in Chapter 3 we get a characteristic electron energy $E_{meerkat} = 7.67 \times 10^{-3}$ TeV.

Using the best-fit values of $u_{low} = 0.9$ eV cm^{-3} and $u_{high} = 8.7$ eV cm^{-3} (from Section 4.3), we obtain a $B_{rad} = 19.667\,\mu$G and $B_{eff} = 20.007\,\mu$G to obtain a synchrotron cooling time τ_{syn} from Equation 3.28 in Chapter 3. Taking into account the expansion velocity of the gas in the lobes of Circinus, 900-950 km s^{-1} (Mingo et al., 2012), we obtain the final results shown in Equation 4.6. The range of L values is a consequence of the range of expansion velocities (Mingo et al., 2012) used.

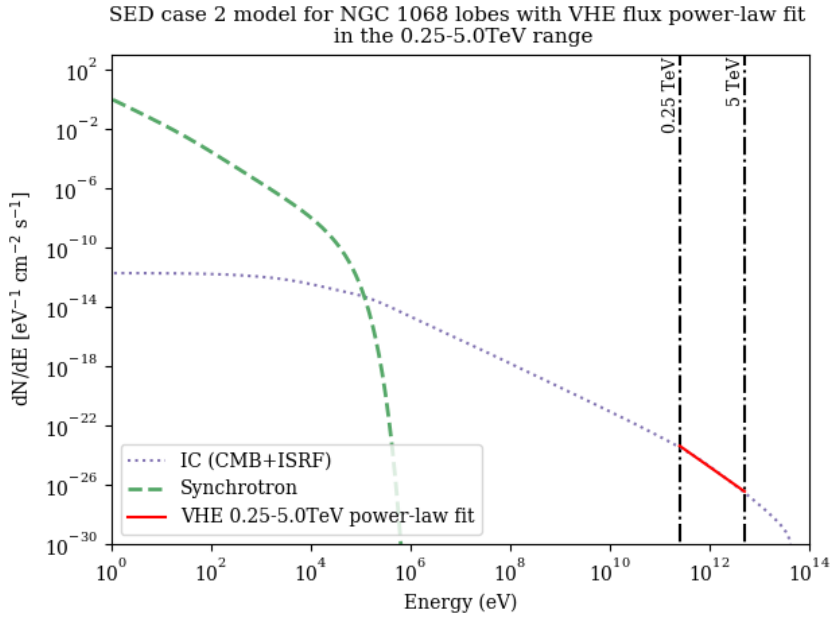

Figure 4.17: NGC 1068 lobes case 2 power-law fit in the 0.25-5.0 TeV range.

$$
\begin{aligned}
&E_{meerkat} = 7.675 \times 10^{-3}\,\text{TeV} \\
&\tau_{syn} = 4.07 \times 10^{6}\,\text{yr} = 128.41 \times 10^{12}\,\text{s} \\
&1.156 \times 10^{20}\,\text{m} \leq L \leq 1.220 \times 10^{20}\,\text{m} \Rightarrow 3.745\,\text{kpc} \leq L \leq 3.953\,\text{kpc}
\end{aligned}
\tag{4.6}
$$

The width produced is at least three times the size of the lobes of Circinus and an order of magnitude larger than the observed width of the shocked region.

Producing 1:10 width to radius ratio

In SNR's the typical width to radius ratio of a shock is 1:10. For a lobe radius of 1 kpc (like the Circinus lobes) to produce a 0.1 kpc width the magnetic field needs to increase. There are two ways to produce $L = 0.1$ kpc:

1. Increase B_{rad} and fix $B_{\perp}$ at 3.67 μG.
2. Increase $B_{\perp}$ and fix B_{rad} at 19.667 μG.

In the first case, only B_{eff} is affected by this change and since $L \propto \tau_{syn} \propto B^{-2}$ to decrease L to 0.1 kpc we need to increase B by a factor of 6.28 $\left(\sqrt{\frac{3.953\,\text{kpc}}{0.1\,\text{kpc}}}\right)$. This produces a $B_{eff} = 125.64\,\mu\text{G}\,(6.28 \times 20.007\,\mu\text{G})$ and a $B_{rad} = 125.59\,\mu G$. This

suggests that the infrared photon field inverse Compton losses are insufficient to produce 0.1 kpc width shells and thus a stronger magnetic field is required to produce this radiation.

In the second case, increasing $B_\perp$ with B_{rad} fixed affects the energy term as well in Equation 3.27. Combining Equations 3.27 and 3.28 and substituting for B_{eff} gives Equation 4.7. Equation 4.7 reduces to Equation 4.8 assuming $L = 0.1$ kpc and $B_{rad} = a$, combining all constants in the factor $b = 2.74613 \times 10^{-7}\,\mathrm{G}^{\frac{3}{2}}\,\mathrm{s}^{\frac{1}{2}}\,\mathrm{m}^{-1}$ and by applying the relevant unit conversions.

$$\tau_{syn} = 12.5 \left(\frac{1\,\mathrm{erg}\sqrt{\frac{\nu_{ch}}{1.8 \times 10^{18} B_\perp}}}{100\,\mathrm{TeV}} \right)^{-1} \left(\frac{(100\mu\,\mathrm{G})^2}{B_{rad}^2 + B_\perp^2} \right) \mathrm{yr} \tag{4.7}$$

$$B_\perp^{-\frac{1}{2}}(a^2 + B_\perp^2) = b\frac{v}{\sqrt{\nu_{ch}}} \tag{4.8}$$

Solving Equation 4.8 at the MeerKAT frequency $\nu_{ch} = 1$ GHz for:

- $v = 900000\,\mathrm{m/s}$ gives $B_\perp = 0.00245\,\mu\mathrm{G}$ or $B_\perp = 393.175\,\mu\mathrm{G}$
- $v = 950000\,\mathrm{m/s}$ gives $B_\perp = 0.00220\,\mu\mathrm{G}$ or $B_\perp = 407.653\,\mu\mathrm{G}$

The typical magnetic field strength of lobes is between 1.0 and 10.0 μG and so such large magnetic field strengths on the order of 400 μG are unlikely in the lobes.

4.4.2 Hydrodynamical approach

Another explanation for the brightened edges is a shock compression scenario. In SNRs, as the shock wave moves through the surrounding material, it compresses the gas inside the shocked region and increases its density by a factor of four (for a strong shock). This results in adiabatic heating of the electrons which boosts the flux of the shocked region and creates the shell observed in the radio (Enßlin and Gopal-Krishna, 2001).

A constant density shell model is assumed in this approach, which is only an approximation but is useful in estimating the width of the shell. The initial density is constant and given by Equation 4.9 for a mass m and radius R.

$$\rho_1 = \frac{m}{\frac{4\pi}{3}R^3} \tag{4.9}$$

Once the shock passes through the material to form the shell dR, the new density is given by Equation 4.10.

$$\rho_2 = \frac{m}{4\pi R^2 dR} \tag{4.10}$$

By mass conservation, we can equate Equations 4.9 and 4.10 to obtain Equation 4.11:

$$dR = \frac{\rho_1}{3\rho_2}R \tag{4.11}$$

In the case of a strong shock where $\rho_2 = 4\rho_1$ the width of the shell is $dR = \frac{1}{12}R$. In the case of Circinus for 1 kpc lobes, we expect a shell width of 0.083 kpc. Figure 4.18 shows the observed width of the northern shell (white box) in Circinus to be ∼0.119 kpc, which is compared to the width of 0.083 kpc expected for a strong shock (green line). We test for this approach using the northern lobe only since the shell is better defined in it compared to its southern counterpart. With this observed width, we find that $\rho_2 \sim 2.80\rho_1$, suggesting a weaker shock compared to what is observed in SNRs.

To quantify the strength of the shock, we can calculate its Mach number $\mathcal{M}$ given by Equation 4.12 (using the Rankine–Hugoniot conditions (Landau and Lifshitz, 1959)) where γ is the adiabatic index of the gas.

$$\frac{\rho_1}{\rho_2} = \frac{\gamma - 1}{\gamma + 1} + \frac{2}{\gamma + 1}\frac{1}{\mathcal{M}^2} \tag{4.12}$$

For $\mathcal{M} > 10$ when $\gamma = \frac{5}{3}$ [e.g., Mingo et al. (2012)], the LHS of Equation 4.12 approaches 1/4 defined as a strong shock. For Circinus, we derive a Mach number of $\mathcal{M}$ 2.7. Mingo et al. (2012) derived a $\mathcal{M} \sim 2.7 - 3.6$ for the northern lobe using the temperature ratios of the plasma from X-ray observations. Given that the two different approaches produce similar results, it is likely that a relatively weak shock is responsible for creating the shell in the northern lobe of Circinus.

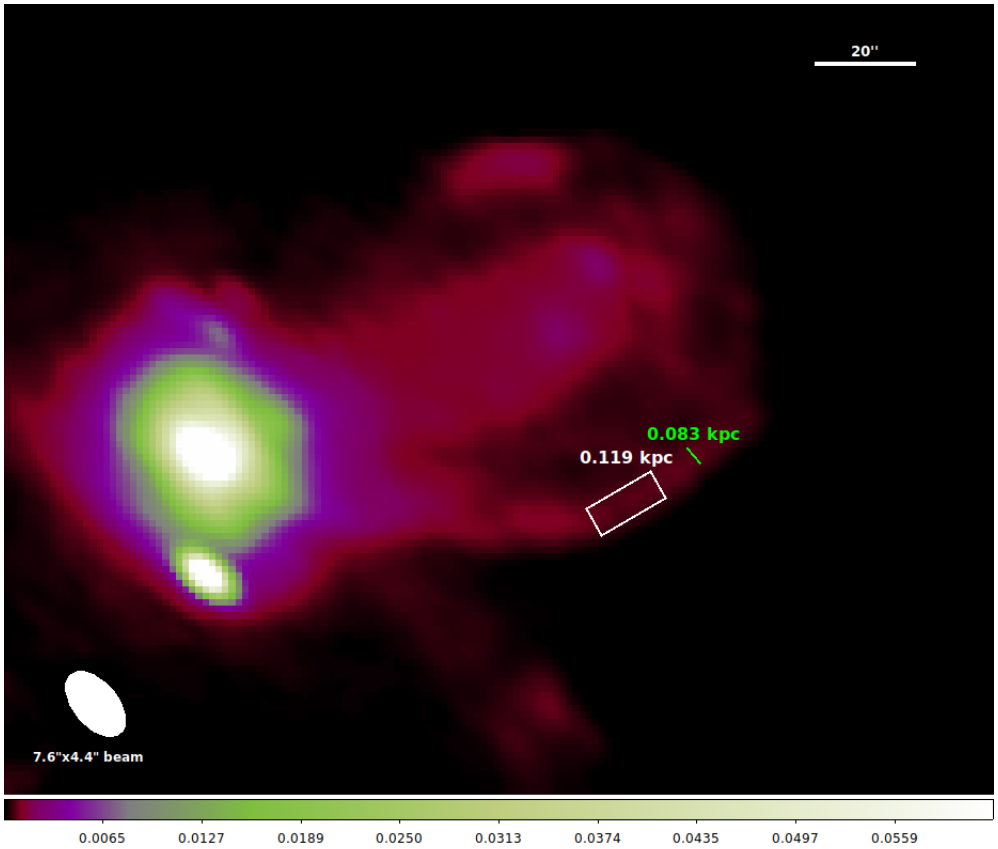

Figure 4.18: 1.375 GHz MeerKAT radio map of Circinus at a 149 MHz bandwidth showing the width of the northern shell (white box) compared to the expected width for a strong shock (green line). The image RMS is 9.03 μJy/beam with a 7.6×4.4 arcsec^2 beam (shown in the bottom left of the image).

4.5 Multi-wavelength analysis of SN1996cr

4.5.1 Modelling the radio light curve

We measured the MeerKAT radio flux density of SN1996cr to be 93.20 ± 0.01 mJy from the 1375 ± 74.5 MHz map.

To model the radio light curve, we do the following:

- Fit the basic Chevalier model to the archival ATCA data in Table 4.11 at a frequency of $\nu = 1.4$ GHz (for Models 1-4 described in Section 3.5.1) firstly with four free parameters ($K1$, $K2$, p & m) and then two free parameters ($K1$ & $K2$ freed and p & m fixed). The curve fitting is done with both the methods discussed in Section 3.5.1.
- Find the best model that fits the ATCA data for each fitting method and then

use this model to find the best-fit parameters after including the MeerKAT data point.

Days after explosion	Flux (mJy)	Instrument
1449	85.2 ± 2.1	ATCA
3198	481 ±7.5	ATCA
4093	505 ± 3.2	ATCA
4678	423 ± 27.3	ATCA
5791	330 ± 40.1	ATCA
8420	93.2 ± 0.009	MeerKAT

Table 4.11: Radio flux data points used in the modelling of the radio light curve of SN1996cr.

To fit the Chevalier model to the ATCA data we first free all four parameters - the results of which can be seen in Table 4.12. We then redid the fit by fixing $p = 2.86$ and $m = 0.91$ (setting it to their average best-fit values from the first round of fitting with four free parameters). Table 4.13 shows the results for the two free parameters. In every case, the model overestimates the flux detected with MeerKAT. Overall, model 1 yields the lowest minimum χ^2/least-squares value and produces the closest flux to the MeerKAT data point for each fitting method per number of free parameters. Model 1 is thus considered as the best-fit model for $a(m)$ & $b(p, m)$ and can be seen in Figures 4.19 - 4.22 where the last data point corresponds to the MeerKAT flux and is not considered in the fit.

Model	**χ^2 method**						**Least-squares method**					
	$K1$	$K2$	p	m	**Minimum χ^2 value**	**MeerKAT predicted flux**	$K1$	$K2$	p	m	**Minimum least-squares value**	**MeerKAT predicted flux**
1	3.03	4942.42	2.98	0.94	164.56	309.00 mJy	11.11	8170.71	3.0	0.78	2184.60	195.72 mJy
2	4.04	1714.14	2.72	0.94	169.42	337.39 mJy	12.12	907.07	2.84	0.83	6688.60	262.75 mJy
3	3.03	3328.28	2.97	0.94	171.38	339.44 mJy	6.06	1714.14	3.0	0.89	5036.31	263.41 mJy
4	4.04	907.07	2.49	0.94	190.24	400.91 mJy	3.03	1714.14	2.84	1.0	6712.18	277.93 mJy

Table 4.12: Results for models 1-4 with $K1$, $K2$, p and m free for the ATCA data.

Model	**χ^2 method**				**Least-squares method**			
	$K1$	$K2$	**Minimum χ^2 value**	**MeerKAT predicted flux**	$K1$	$K2$	**Minimum least -squares value**	**MeerKAT predicted flux**
1	4.04	4942.42	162.10	309.09 mJy	6.0	2521.21	3905.07	237.87 mJy
2	4.04	2521.21	341.72	336.80 mJy	8.0	907.07	8640.99	246.67 mJy
3	4.04	2521.21	173.91	348.71 mJy	5.0	1714.14	9115.75	296.83 mJy
4	5.05	907.07	331.46	339.34 mJy	5.0	907.07	16571.27	335.95 mJy

Table 4.13: Results for models 1-4 with p and m fixed for the ATCA data.

Next, we fit the Chevalier model to the ATCA and MeerKAT data for model 1 by freeing all four parameters. Table 4.14 compares the results before and after the inclusion of the MeerKAT data point. From these results, we note that to accommodate for the MeerKAT flux, $K1$ and $K2$ need to increase by one order of magnitude, m drops to 0.5-0.6 and p is not affected as much.

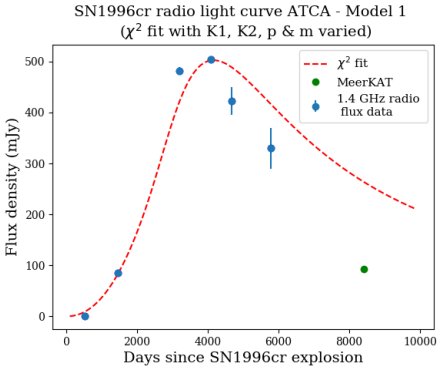

Figure 4.19: SN1996cr radio flux model 1 with χ^2 fit for ATCA data with four free parameters.

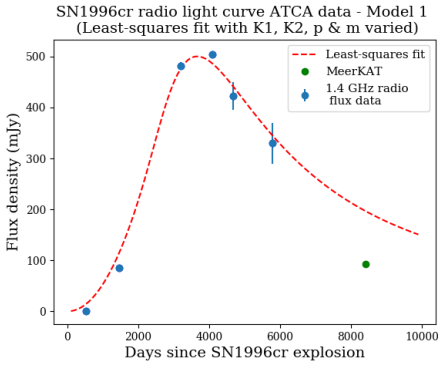

Figure 4.20: SN1996cr radio flux model 1 with least squares fit for ATCA data with four free parameters.

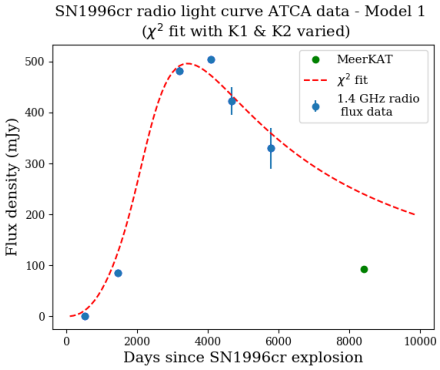

Figure 4.21: SN1996cr radio flux model 1 with χ^2 fit for ATCA data with two free parameters.

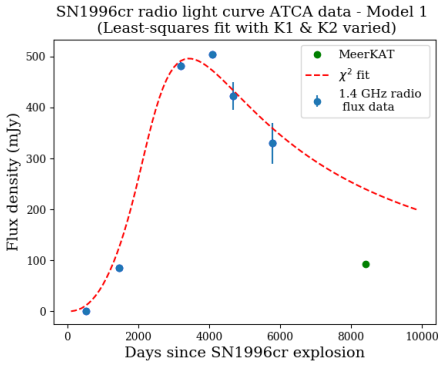

Figure 4.22: SN1996cr radio flux model 1 with least squares fit for ATCA data with two free parameters.

For the remainder of this discussion, the χ^2 fit (Figure 4.23) will be referred to as the MeerKAT favoured Chevalier (MFC) model and the least-squares fit (Figure 4.24) will be referred to as the ATCA favoured Chevalier (AFC) model. The implications of these models can be seen in Table 4.15.

The MFC model naturally fits the MeerKAT data point, since the statistical uncertainty in the MeerKAT flux is very low compared to the ATCA data (as seen in Table 4.11), but this occurs at the expense of lowering the peak. Conversely, the AFC model provides a good fit of the peak but overestimates the MeerKAT flux (Figure 4.24). It can also be said that to accommodate for the MeerKAT flux in the MFC model, the flux in the early absorption phase increases more gently in time compared to the AFC model, and the flux decline in the emission phase is steeped in time.

To understand the behaviour of the free parameters for each model, we allowed each parameter to vary with the other three fixed at the best-fit values for each model.

Data	χ^2 method						Least-squares method					
	$K1$	$K2$	p	m	**Minimum χ^2 value**	**MeerKAT predicted flux**	$K1$	$K2$	p	m	**Minimum least-squares value**	**MeerKAT predicted flux**
ATCA	3.03	4942.42	2.98	0.94	164.56	309.00 mJy	11.11	8170.71	3.0	0.78	2184.60	195.72 mJy
ATCA + MeerKAT	51.40	33996.97	3.0	0.5	3736.97	93.20 mJy	34.66	21555.56	3.0	0.6	7623.50	150.69 mJy

Table 4.14: Results for models 1 with $K1$, $K2$, p and m free for the ATCA data only and the ATCA + MeerKAT data.

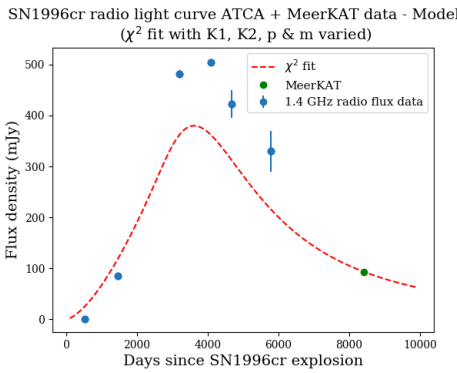

Figure 4.23: SN1996cr radio flux model 1 with χ^2 fit for ATCA+MeerKAT data with four free parameters.

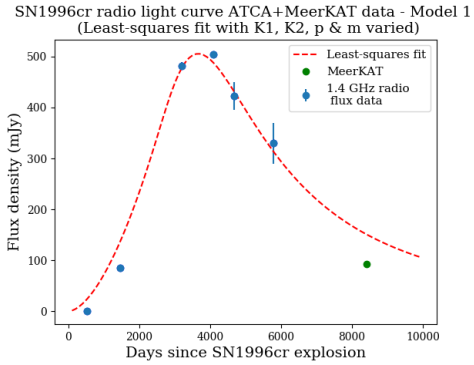

Figure 4.24: SN1996cr radio flux model 1 with least squares fit for ATCA+MeerKAT data with four free parameters.

This is shown in Figures 4.25 -4.28. We found that:

- Increasing $K1$ increases the overall flux density, increases the peak value, and steepens both the absorption phase and emission phase fluxes' evolution with time.
- Increasing $K2$ shifts the graph to the top right, which means it increases the peak flux value in the absorption phase, delays the start of the emission phase, and increases the flux in this latter phase.
- Increasing m also shifts the graph to the top right, like $K2$, but steepens the flux increase with time in the absorption phase.
- Increasing p shifts the graph to the bottom left, which means it decreases the peak value of the absorption phase flux, it results in an earlier start for the emission phase and decreases the flux in this latter phase.

Therefore, in the MFC model to better fit the ATCA data and specifically the peak of the data, we could increase $K1$ beyond 50 mJy and m beyond 0.5, but this no longer includes the MeerKAT data point.

Properties	MeerKAT-fitted Chevalier model	ATCA-fitted Chevalier model
Forward shock radius	$R \propto t^{0.5}$	$R \propto t^{0.6}$
Electron energy distribution	$N(E) = N_0 \times E^{-3.0}$	$N(E) = N_0 \times E^{-3.0}$
Flux (Absorption phase)	$F \propto t^{1.5}$	$F \propto t^{1.7}$
Flux (Emission phase)	$F \propto t^{-2.5}$	$F \propto t^{-2.2}$

Table 4.15: Summary of SN1996cr radio light curve modelling results.

To improve this model, including archival data with statistical uncertainty along the same order of magnitude as the MeerKAT results could assist as well as more flux density measurements between days 5000 and 8000 after the explosion of SN1996cr. In general, it can be noted that the basic Chevalier model is not sufficient to accurately describe the emission/flux decline phase that is measured by MeerKAT (it can describe the absorption phase relatively well) and a more complex model might be required to describe the temporal evolution of the radio flux of SN1996cr.

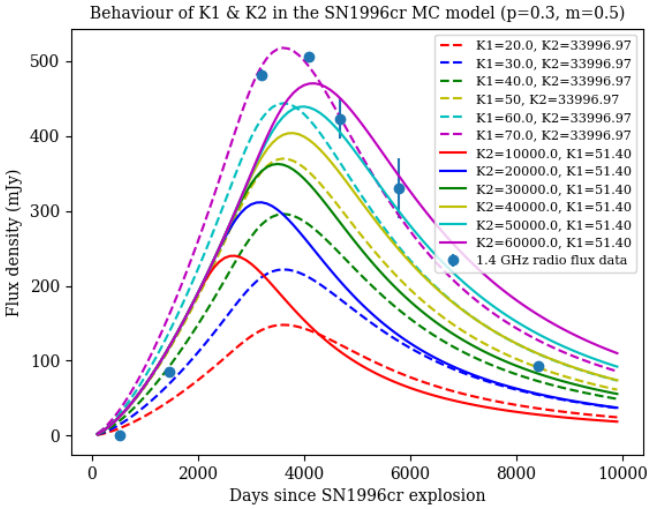

Figure 4.25: Behaviour of $K1$ and $K2$ in the SN1996cr MFC radio flux model.

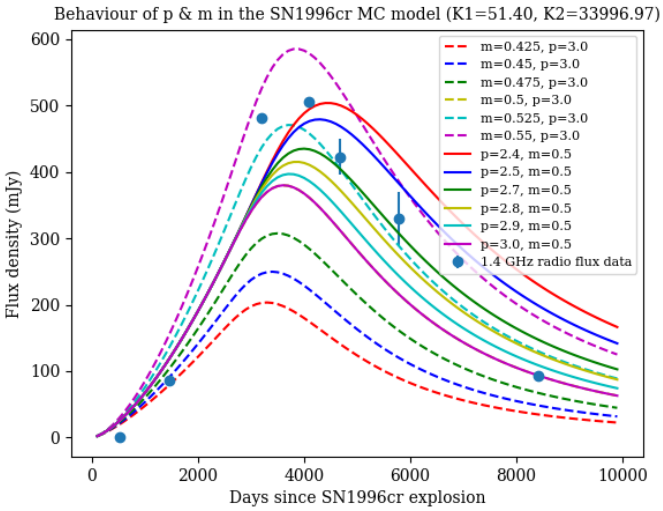

Figure 4.26: Behaviour of m and p in the SN1996cr MFC radio flux model.

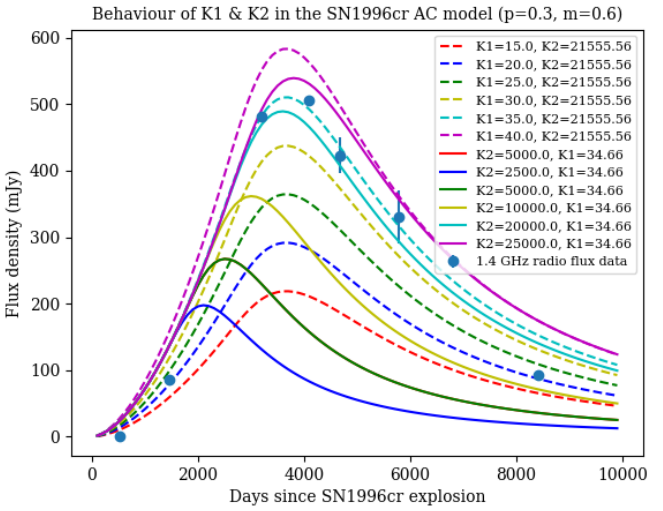

Figure 4.27: Behaviour of $K1$ and $K2$ in the SN1996cr AFC radio flux model.

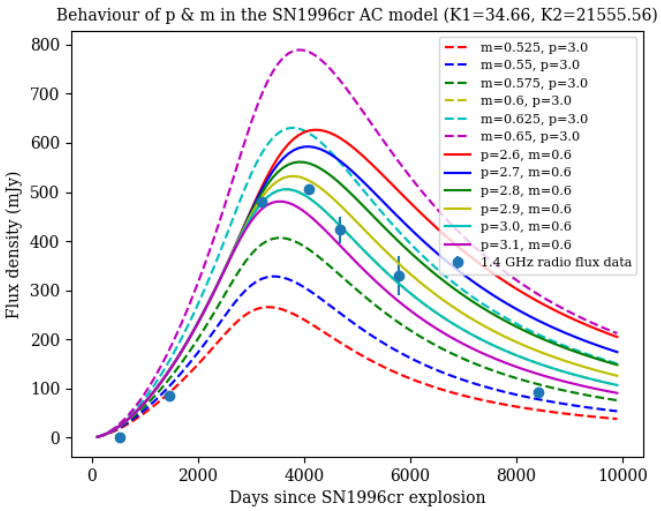

Figure 4.28: Behaviour of m and p in the SN1996cr AFC radio flux model.

4.5.2 Modelling the γ-ray light curve

We modeled the γ-ray light curve assuming the *Fermi*-LAT GeV emission of Circinus originates from SN1996cr. We performed a binned likelihood analysis of two-year time bins for the full ten years of data - totalling five intervals. The same likelihood routine was used as the ten-year run in each interval but with a new source model. The source model was set up such that sixteen parameters were fixed at the global best-fit values from the v9 analysis and the other fixed parameters were set at their values from the 4FGL-DR2 catalog. 20 spectral parameters were freed in the source model as outlined in Section 3.5.2.

In the initial run, we performed a binned likelihood for energies above 0.1 GeV using the two-year time binning with the Minuit algorithm to perform the fit. Intervals 1 and 2, corresponding to the first four years, did not converge using this method. To achieve successful convergence, we applied a NEWMINUIT fit to the two-year binned likelihood analysis above 1 GeV. The final GeV flux of Circinus in each interval is shown in Table 4.16.

Interval	**Flux (photons/cm^2/s)**	**TS value**
1	$(7.64 \pm 2.17) \times 10^{-10}$	22.35
2	$(7.07 \pm 2.07) \times 10^{-10}$	19.74
3	$(5.57) \pm 1.97) \times 10^{-10}$	12.19
4	$(4.38 \pm 1.83) \times 10^{-10}$	9.92
5	$(6.85 \pm 2.14) \times 10^{-10}$	15.91

Table 4.16: GeV flux of Circinus and corresponding TS value for the final two-year binned likelihood analysis.

The resultant light curve after a χ^2 curve-fit is shown in Figure 4.29 which shows the best-fit of the two models: the constant model (Flux=C1) and the decline model (Flux=C2/t). We also derived the 1σ 68% confidence interval of $C1$ and $C2$ (Equation 4.13) assuming the critical χ^2 value of 1.0 for a p-value of 0.32 (68% containment) and one degree of freedom.

$$\chi^2 - \chi^2_{min} < 1.0 \tag{4.13}$$

To find the minimum and maximum values of the intervals, we found the C1 and C2 values when Equation 4.13 is equal to 1.0:

- $C1$: $\chi^2 = 1.81 + 1.0 = 2.81 \Rightarrow (C1_{min}, C1_{max}) = (5.25 \times 10^{-10}, 7.06 \times 10^{-10})$ photons/cm^2/s

- $C2$: $\chi^2 = 1.21 + 1.0 = 2.21 \Rightarrow (C2_{min}, C2_{max}) = (3.40 \times 10^{-6}, 4.56 \times 10^{-6})$ photons/cm^2

The χ^2 values are very similar for both models and so one model cannot be favoured over the other.

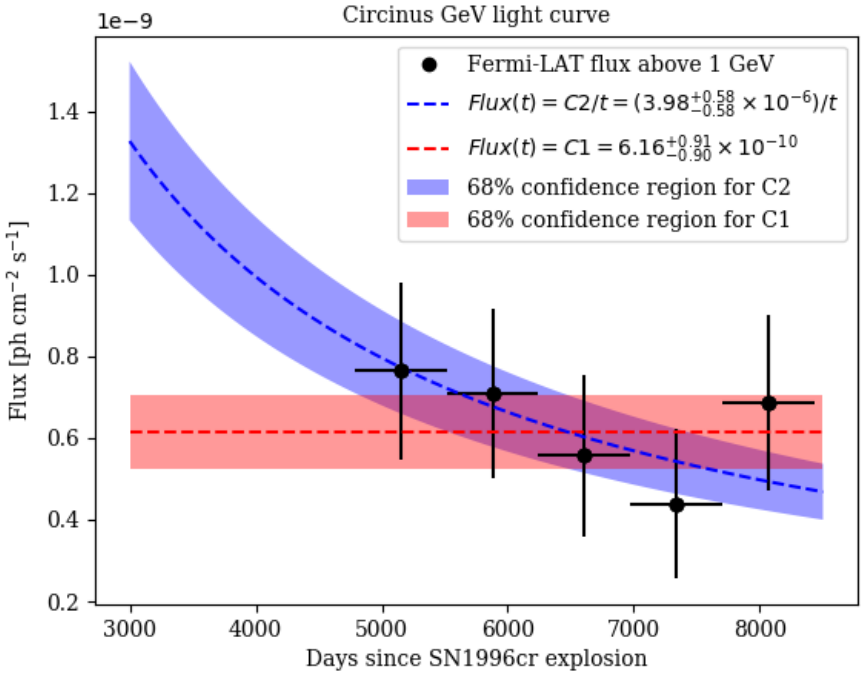

Figure 4.29: GeV light curve of Circinus above 1 GeV fitted with two models.

4.6 Discussion of results

The following subsections cover a discussion on the interpretation of the multi-wavelength results outlined in this chapter.

4.6.1 Superiority of MeerKAT images.

Dr Beatriz Mingo and Dr Emil Lenc shared their ATCA images of Circinus Mingo et al. (2012). Their 1.499 GHz ATCA radio image in Figure 4.30 is of a similar central frequency to MeerKAT. A comparison between these two images of Circinus (Figure 4.1 and Figure 4.30) demonstrates how much deeper the MeerKAT image is. In the MeerKAT image, the shock structure is observed better, the localisation of the core is more precise, the regions of different brightness are observed more clearly, and there is a higher sensitivity to fainter emission. Also, the hotspot in the NW lobe is more visible and clearly defined.

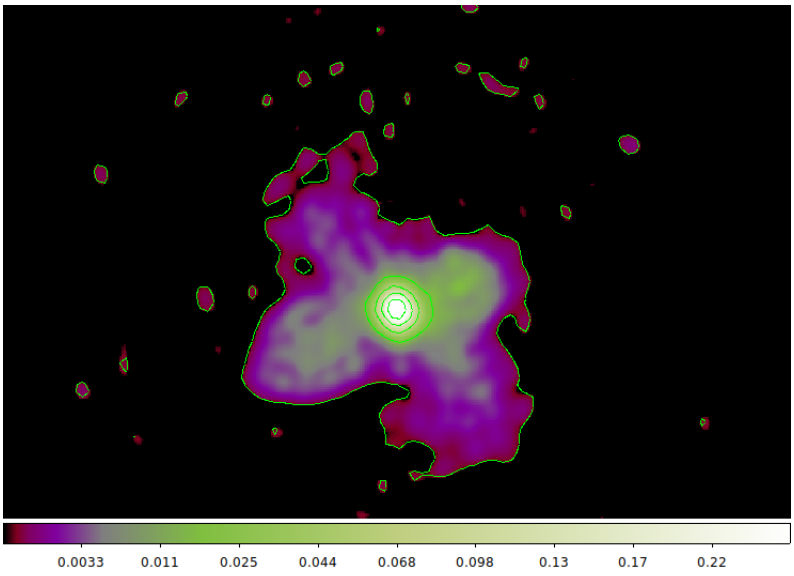

Figure 4.30: 1.499 GHz ATCA radio map of Circinus with a 20.1×18.6 arcsec^2 beam [Image scale: 1 px $\sim$ 2.0 arcsec] (Mingo et al., 2012).

When comparing the flux of the lobe substructure between MeerKAT and ATCA observations, we found that the lobe flux is larger than the shell flux in the measurements compared to the ATCA measurements in which these structures show similar fluxes. This also demonstrates MeerKAT's ability over ATCA's to distinguish between regions of different brightness more clearly.

MeerKAT observations of Circinus thus confirm the presence of its radio lobes and

allow us to study its structure in detail.

4.6.2 Comparison to the Fermi bubbles

In both the Circinus lobes and the Fermi bubbles, brightened edges are observed in the radio band with counterparts in the X-ray band indicative of shocked regions. The cocoon region in the Fermi bubbles is observed as enhanced GeV emission with *Fermi*-LAT. Enhanced radio emission is observed in the Circinus lobes known as plumes but the lobes of Circinus are not spatially resolvable with *Fermi*-LAT to observe any possible GeV counterpart to this excess. Understanding the GeV emission in Circinus could be enabled with CTA-South observations.

4.6.3 Towards understanding the origin of the lobe emission

Challenging previous claims against the starburst model

In general, a flatter spectral index can be associated with ongoing particle acceleration and a steeper index can be associated with an ageing electron population along the flow due to radiative losses.

A variation in spectral index across the lobes is used by Mingo et al. (2012) as evidence against the starburst-driven model. They observed spectral flattening towards the hotspots and steepening in the shells and they refer to Figure 4.31 taken from (Elmouttie et al., 1998a). They claim that this behaviour is typical of radio jets interacting with the ISM producing hotspots. In the AGN jet-driven model, this interaction is also responsible for the formation of shock waves which are observed in both the radio and X-ray for Circinus.

The error in the spectral index by Mingo et al. (2012) is large and their claim of spectral flattening should be considered as tentative evidence.

The spectral index map produced by MeerKAT in Figure 4.6 and the indices reported for the lobe sub-structure in Table 4.6 do not show the large variations found in ATCA observations. The only noticeable feature is that the southern hotspot is possibly steeper than its surroundings. This observation, therefore, challenges the claim made by Mingo et al. (2012) that the spectral index distribution shows support for the AGN jet-driven model.

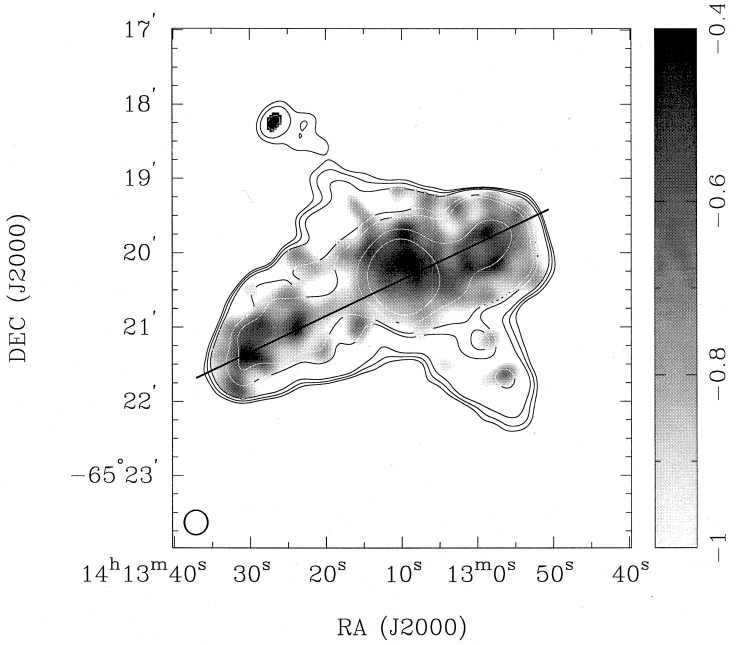

Figure 4.31: 1.499 GHz - 5.000 GHz ATCA spectral index map with 5.000 GHz ATCA radio emission contours (Elmouttie et al., 1998a).

Origin of emission in the shocked region (shell)

When calculating the width of the shocked region due to synchrotron cooling, we found that the expected width is an order of magnitude larger than the observed width from MeerKAT observations. To match the observations, the magnetic field would need to be close to 400 μG (and the typical B for lobes are between 1.0 and 10.0 μG) or require a larger effective magnetic field associated with a stronger ISRF field with significant inverse Compton losses. Synchrotron cooling is thus not a feasible mechanism to explain the width of the shocked region.

The shocked region is more likely created due to shock compression. Using a hydrodynamical approach, we found the shock wave to increase the density in the Northern shell by a factor of 2.8 relative to its surrounding medium density. We derived a Mach number $\mathcal{M}$ 2.7 from this observation, compatible with the results by Mingo et al. (2012) who used a different approach, indicating a relatively weak shock.

There is a relation between the radio spectral index α_r and $\mathcal{M}$ (Colafrancesco et al., 2017) which we can use to evaluate our results shown in Equation 4.14. For $\mathcal{M}$ 2.7 a radio spectral index of ~ 0.8 is expected. This index is roughly compatible with the Figure 4.6 in which the lobe edges have indices $\sim 0.6 - 0.7$.

$$\alpha_r = \frac{3 + \mathcal{M}^2}{2\mathcal{M}^2 - 2} \tag{4.14}$$

For shock waves with $\mathcal{M} > \sqrt{5} \sim 2.2$, particle acceleration is possible (Vink and Yamazaki, 2014). Our calculated Mach number thus permits particle acceleration on shock fronts, although it is close to the lower limit of $\sqrt{5}$. We conclude that the shock wave around the Circinus lobes can be one of the potential sites of acceleration of relativistic electrons present in these lobes. All these results from our hydrodynamical approach support a weak shock compression model.

Feasibility of the starburst-driven model

To assess the feasibility of the starburst-driven model, we consider the argument made by Mingo et al. (2012). The age of the lobes is inferred to be $\sim 10^6$ years for a gas expansion velocity of 900-950 km/s and the total energy needed to create the shocked regions is calculated to be 2×10^{55} erg (Mingo et al., 2012). A single SN explosion at maximum efficiency releases 10^{51} erg. For a timescale of 10^6 years, this would require a SN rate of $\sim$0.02/year $[\frac{10^{55}}{10^{51}}/10^6$ years]. This matches well with the SN rate derived by Elmouttie et al. (1998a) (0.02/year) and Mingo et al. (2012) (0.026/year). Thus, the compatibility of these timescales permits a superwind driven model.

4.6.4 Interpretation of the GeV emission of Circinus

CR-ISM interaction

In the analysis by Guo et al. (2019) they found that the γ-ray luminosity of Circinus is consistent with an empirical relation for star-forming galaxies (Ackermann et al., 2012) in which the GeV emission originates from interactions between SNR-accelerated CRs and the ISM. Figure 4.32 shows the relation between the IR and γ-ray luminosity displayed for a sample of starburst and local group galaxies and includes the results for Circinus by Hayashida et al. (2013) in red and by Guo et al. (2019) in blue. The lower flux and luminosity obtained by Guo et al. (2019) meant that Circinus lies closer to this empirical scaling relation, compared to Hayashida et al. (2013) .

We calculated the γ-ray luminosity of Circinus using our results (which includes an

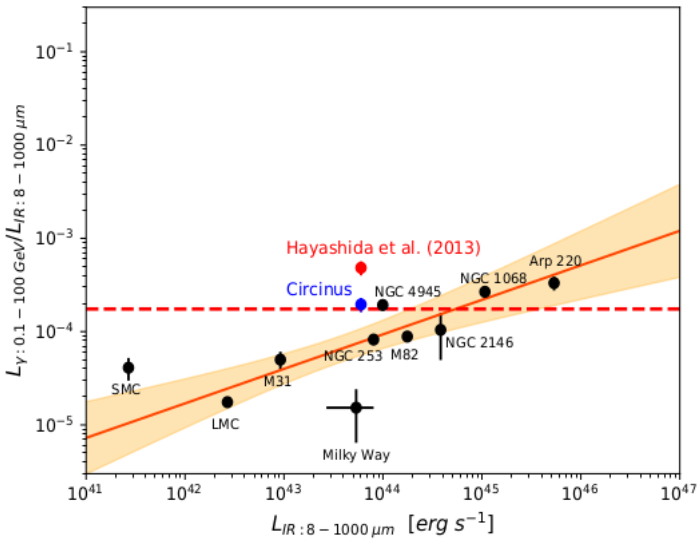

Figure 4.32: 0.1-100 GeV γ-ray to 8-1000μm IR luminosity ratio for a sample of galaxies including Circinus (Guo et al., 2019).

even lower flux) to see how it compares with the scaling relation. For this, we redid the likelihood analysis in the 0.1-100.0 GeV range (using the same approach as v9 with a different maximum energy) for the same fixed photon index $\Gamma = 2.26$ and found a similar photon flux of $F_{\gamma_{0.1-100.0\,\mathrm{GeV}}} = (9.56 \pm 1.39) \times 10^{-9}$ photons/cm^2/s. To calculate the luminosity we first use Equation 4.15 (Ghisellini et al., 2009) get the energy flux between ν_1 and ν_2 (the frequencies associated with the minimum and maximum energy i.e. 0.1 GeV and 100.0 GeV respectively) using the spectral index $\alpha_\gamma = 1 - \Gamma$ and the Planck constant h.

$$S_\gamma(\nu_1, \nu_2) = \frac{\alpha_\gamma h \nu_1 F_\gamma}{1 - \alpha_\gamma} \left(\left(\frac{\nu_2}{\nu_1} \right)^{1-\alpha_\gamma} - 1 \right) \tag{4.15}$$

Using the energy flux $S_\gamma(\nu_1, \nu_2)$ we calculated the γ-ray luminosity from Equation 4.16 (Ghisellini et al., 2009) where d_L is the luminosity distance ($\sim$4 Mpc for Circinus) and the red-shift z ($\sim$9.2 $\times 10^{-4}$).

$$L_\gamma = 4\pi d_L^2 \frac{S_\gamma(\nu_1, \nu_2)}{(1+z)^{1-\alpha_\gamma}} \tag{4.16}$$

The second row of Table 4.17 shows the result for the γ-ray luminosity using the 4FGL-DR2 photon index in the likelihood analysis. This value is consistent with the luminosity obtained by Guo et al. (2019) in the first row.

In the analysis by Guo et al. (2019) they freed more spectral parameters including

the photon index for which they obtain $\Gamma = 2.2$ as their best-fit. To test how much lower we could go in luminosity, we redid the analysis freeing both the normalisation and photon index and obtained $\Gamma = 2.06 \pm 0.11$. With this, we obtain a lower luminosity. However, all three results in Table 4.17 have similar γ-ray to IR luminosity ratios (assuming $L_{IR_{8.0-1000.0\,\mu\mathrm{m}}} = 0.66 \times 10^{44}$ erg/s (Hayashida et al., 2013)). The smaller photon index does produce a smaller ratio bringing Circinus even closer to the empirical star-forming galaxies scaling relation. In addition, in the proton calorimeter model, for which Guo et al. (2019) advocate, the expected γ-ray luminosity for Circinus is $(1.05 \pm 0.40) \times 10^{40}$ erg/s (Guo et al., 2019). A lower photon index thus brings us even closer to the proton calorimeter limit (shown in red in Figure 4.32).

	Γ	$F_{\gamma_{0.1-100.0\,\mathrm{GeV}}}$ **(photons/cm^2/s)**	$L_{\gamma_{0.1-100.0\,\mathrm{GeV}}}$ **(erg/s)**	$\frac{L_{\gamma_{0.1-100.0\,\mathrm{GeV}}}}{L_{IR_{8.0-1000.0\,\mu\mathrm{m}}}}$
Guo et al. (2019)	2.20	$(5.72 \pm 1.96) \times 10^{-9}$	$(1.17 \pm 0.44) \times 10^{40}$	1.95×10^{-4}
4FGL-DR2 Γ	2.26	$(9.56 \pm 1.39) \times 10^{-9}$	$(1.12 \pm 0.16) \times 10^{40}$	1.87×10^{-4}
Γ freed	2.06 ± 0.11	$(6.10 \pm 1.86) \times 10^{-9}$	$(1.02 \pm 0.40) \times 10^{40}$	1.70×10^{-4}
Proton calorimeter limit	-	-	1.05×10^{40}	1.75×10^{-4}

Table 4.17: *Fermi*-LAT γ-ray luminosity in the 0.1-100.0 GeV range for different photon indices.

In summary, we can confirm that it is possible for the GeV emission from Circinus to originate from the CR-ISM interaction (due to star-forming processes) and our results provide evidence that Circinus is a proton calorimeter.

Search for the flux decline of SN1996cr

The flux output from the ten-year *Fermi*-LAT likelihood analysis is consistent with Guo et al. (2019) and 4FGL-DR2. The GeV flux obtained by Guo et al. (2019) (10 years of observations and eight-year source catalog) was lower than both the 4FGL catalog (eight-year source catalog) and the likelihood analysis by Hayashida et al. (2013) (four years of observations and two-year source catalog). Guo et al. (2019) propose that this drop in flux is a result of the additional point sources they observed. The 4FGL-DR2 catalog (ten-year source catalog) includes more data than the 4FGL catalog and the additional point sources used by Guo et al. (2019) and using this updated catalog we find a lower GeV flux. Considering that as more data is included, from the analysis by Hayashida et al. (2013) to the one by Guo et al. (2019) and then our analysis, a drop in flux is observed, it is possible that there is an actual flux decline with time and it is not just a result of additional point sources that were not resolved initially.

The variability of this emission was studied by Guo et al. (2019) and they found that the GeV flux of Circinus in the first five years drops by a factor of $\sim 1.5 - 2$ in the second five years of observation. They consider this as marginal evidence of variability on the timescale of years.

We thus considered the case in which this flux decline is dominated by the γ-ray emission of SN1996cr. This investigation was motivated by the possible case of GeV flux decline observed in SN2004dj (Xi et al., 2020). Applying a two-year binning to the ten years of data, we were able to obtain the flux within each interval and generate the light curve. We tested for both a constant and a decline model and found that both models are plausible. To better understand this GeV emission, we require more observations with *Fermi*-LAT which could favour one model over the other and help us better understand the origin of this emission (SN1996cr, lobes or some other process). CTA-South's higher angular resolution could also play an instrumental role in understanding the GeV emission from Circinus.

Scientific case for H.E.S.S. observations

I am a MSc member of the modelling group of the H.E.S.S. Starburst/Seyfert task force and the responsibility of this modelling group is to model VHE γ-ray emission from the Circinus and NGC 1068 galaxies, but not to analyse the H.E.S.S. observations (for which other members are responsible). Thus, the preliminary flux upper limits used in this section are provided by the leader of the H.E.S.S. Starburst/Seyfert task force, Andrew Chen for the sake of comparison with the emission models produced in this thesis.

Circinus is observed as a point source with the H.E.S.S. since the angular scale of the lobes of Circinus (<1 arcmin) cannot be spatially resolved with the H.E.S.S. instrument. There are ∼7 hours of H.E.S.S. observations of Circinus in 2006 & 2007 (before the launch of *Fermi*-LAT) and ∼20 hours in 2014 but with no γ-ray excess.

The preliminary H.E.S.S. results for Circinus, in Table 4.18, is based on the entire data set for Circinus but using the old data analysis.

We can use our broadband emission model to predict the VHE emission observed with H.E.S.S. using the results of the power-law fit in the observable H.E.S.S. energy range (shown again in Table 4.18). The integral upper limit above 1 TeV observed with H.E.S.S. at the location of Circinus is 1.058×10^{-13} ph/cm^2/s. This upper limit is smaller than the predicted flux value at 1 TeV in our model found to be

1.5×10^{-13} ph/cm^2/s (assuming a power-law index of -2.34 when fitting a power-law spectrum to the SED in the 0.2-5.0 TeV range). In the case of the lobes of NGC 1068, there exist good constraints after 100 hours of H.E.S.S. observations. The preliminary integral H.E.S.S. upper limit for these lobes is similar to the flux predicted according to our model.

	Circinus lobes		**NGC 1068 lobes**	
	Γ	F(>1 TeV) (ph cm^{-2}s^{-1})	Γ	F(>1 TeV) (ph cm^{-2}s^{-1})
H.E.S.S.	2.5	1.058×10^{-13}	2.4	1.0×10^{-13}
Broadband emission model	2.34	1.5×10^{-13}	2.36	0.9×10^{-13}

Table 4.18: H.E.S.S. integral flux upper limits compared to the modeled VHE predictions.

We can also make predictions using the results of the two-year time binned likelihood analysis, in which we found that the flux (above 1 GeV) decline model is just as likely as the steady emission. SN1996cr was only observed by *Fermi*-LAT 4000 days after it exploded, but there are observations before this with H.E.S.S. Using the flux decline model, we can find the GeV flux at the time of the H.E.S.S. observations - day 39570 (May 2006) and day 6879 (May 2014) after the explosion of SN1996cr. This GeV flux can then be extrapolated to TeV energies and compared with the H.E.S.S. upper limits, shown in Table 4.19. It should be noted that this extrapolation to TeV energies is an overestimation, but is sufficient for the purpose of this analysis.

In the first case, we assume the photon index of 2.26 (given by the 4FGL-DR2 source catalog) when extrapolating to TeV energies. Using this index, we find that the 2014 predicted flux is lower than the H.E.S.S. upper limit. So we tried re-running the analysis on the full ten-year data set using approach v9 but with a minimum energy of 1.0 GeV (as opposed to 0.1 GeV) and freeing the spectral index this time, yielding a best-fit photon index of 2.22. Using this index to do the extrapolation produces fluxes above the H.E.S.S. upper limits.

Γ	$F(>1$ **TeV, May 2006)** **(ph cm^{-2}s^{-1})**	$F(>1$ **TeV, May 2014)** **(ph cm^{-2}s^{-1})**
2.26	1.669×10^{-13}	0.960×10^{-13}
2.22	2.205×10^{-13}	1.268×10^{-13}

Table 4.19: Predicted VHE flux of Circinus detectable by H.E.S.S. based on the GeV flux decline model of SN1996cr.

In summary, we found that our estimates of the expected γ-ray emission from the radio lobes of Circinus and the extrapolated SN1996cr GeV emission can be tested with H.E.S.S.. Since the TeV flux is expected to drop with time, my estimates show that it makes sense to derive flux upper limits from the whole H.E.S.S. data as well

as from 2006, 2007 and 2014 individually using the new data analysis. This presents a new scientific case to renalyse the archival H.E.S.S. data of Circinus to search for a brighter TeV signal. The H.E.S.S. observations can constrain the lobe structures in nearby galaxies and allow us to probe models for transient events with data collected before the *Fermi*-LAT launch.

Chapter 5

Conclusion

5.1 Summary of results

In this project, we first conducted a spatial analysis of the L-band MeerKAT images of Circinus. We compared these images to previous ATCA images of the Circinus lobes and found that MeerKAT enables deeper observations of the same structures with a higher sensitivity to fainter emission. MeerKAT is thus better able to distinguish regions of different brightness, including the precise localisation of the edge-brightening effect.

The features from the MeerKAT observations were also compared to existing multi-wavelength observations of the Fermi bubbles. Similarities between the bubbles and lobes include edge-brightening observed in both the radio and X-ray. Enhanced emission regions are observed as plumes (radio) in the Circinus lobes and as 'cocoons' (GeV) in the Fermi bubbles.

The two-point MeerKAT spectral index analysis shows a harder index for the lobes (NW: 0.68 ± 0.01 & SE: 0.66 ± 0.01) and shells (NW: 0.51 ± 0.01 & SE: 0.59 ± 0.01) compared to the derived spectral indices of the lobes (NW: 0.71 ± 0.06 & SE: 0.78 ± 0.16) and shells (NW: 0.70 ± 0.13 & SE: 0.84 ± 0.20) from ATCA observations by Mingo et al. (2012). The MeerKAT results also show a more uniform distribution of the lobe sub-substructure contrary to the ATCA results showing spectral flattening towards the hotspots used as tentative (due to large errors) evidence against the starburst model. The MeerKAT observations thus challenge prior evidence used in support of the jet model and so a starburst origin for the lobes is still possible.

One of the objectives of this project is understanding the origin of the lobe emission. The computations show that the shocked region is not produced due to synchrotron cooling but rather shock compression. From the observed width of the shell from the MeerKAT observations, it is found that as the shock wave passes through the ISM it increases the density of the shocked region by a factor of 2.8 corresponding to a weak shock. This is further supported by the computed shock Mach number of $\mathcal{M}$ 2.7 which is less than the Mach number required for a strong shock ($\mathcal{M} > 10$). Furthermore, this Mach number also permits particle acceleration, suggesting that the shock front is a potential particle acceleration site in the lobes.

Hence, it is likely that a weak shock created the shell enabling weak particle acceleration resulting in the edge-brightening effect.

Using the results of the likelihood analysis of the ten-year *Fermi*-LAT data with the 4FGL-DR2 catalog, the GeV flux ($(9.56 \pm 1.39) \times 10^{-9}$ photons/cm^2/s) and luminosity ($(1.12 \pm 0.16) \times 10^{40}$ erg/s) was obtained. These results are compatible with the 4FGL-DR2 catalog and the findings by Guo et al. (2019). This GeV luminosity is consistent with the empirical star-forming galaxy relation (as found by Guo et al. (2019) but not by Hayashida et al. (2013) who used fewer data and an earlier source catalog) suggesting that the GeV emission can originate from the CR-ISM interaction. Furthermore, the luminosity obtained also supports that Circinus is a proton calorimeter in which the γ-ray luminosity scales linearly with the SFR.

The Likelihood analysis on the 10-year data set was rerun for a two-year time binning to obtain the flux within each bin and to generate the GeV light curve. We investigated the possibility that the GeV emission originated from the flux decline of SN1996cr. Previous analyses (Hayashida et al., 2013; Guo et al., 2019) and the 4FGL-DR2 catalog all assumed a constant flux evolution. In this project, a constant and a flux decline model are explored and both are shown to be plausible and so it is still possible for SN1996cr to be the source of the GeV emission. More *Fermi*-LAT data is required to investigate the GeV emission origin further.

A radio light curve of SN1996cr was also modeled using the basic Chevalier model fitted to archival ATCA data and MeerKAT data. This model could not accurately describe the flux decline of SN1996cr observed with MeerKAT and a more complex model might be required to describe the temporal evolution of the radio flux of SN1996cr better.

A broadband emission model of the Circinus lobes was developed which fit the lower energy data well for a magnetic field of $3.5\,\mu$G and $N = 1.5 \times 10^{-10}$ cm^{-3}. Including contributions from the ISRF as inputs for inverse Compton emission en-

hanced the VHE emission significantly. According to the model, observation of the lobes by *Fermi*-LAT is unlikely (as expected) but there is promise for detection by CTA-South. Using the fitted power-law broadband emission model and the GeV light curve, both extrapolated to TeV energies yielded an expected flux (1.5×10^{-13} ph/cm^2/s and $> 1.3 \times 10^{-13}$ ph/cm^2/s respectively) greater than the existing H.E.S.S. upper limits of Circinus (1.058×10^{-13} ph/cm^2/s). This presents a scientific case for H.E.S.S. to search for a brighter TeV signal which can be used to constrain the lobe structures.

In summary, we were able to successfully observe the Circinus lobes with MeerKAT through deeper and more sensitive observations than before. Through the multi-wavelength analysis we found that the shell of the lobes is likely created due to a weak shock accelerating electrons to produce the brightened lobe edges and the MeerKAT spectral index map challenges previous evidence made against the starburst model. We also found that the GeV emission is more consistent with a starburst origin due to the CR-ISM interaction, but at the same time we cannot rule out the possibility that this GeV emission originates from the flux decline of SN1996cr. The similarities between the Circinus lobes and Fermi bubbles include the brightened edges and enhanced emission in the plumes. Future multi-wavelength observations with instruments such as MeerKAT and CTA-South would be fruitful in understanding the origin of the lobe emission and possibly finding further connections to the Fermi bubbles.

5.2 Future work

Analysis of MeerKAT observations at other frequencies could reveal new structures not seen in the 1020 MHz - 1380 MHz range considered in this project. These radio images can also enable more observations of the brightened edges to study the shock wave and see if evidence for particle acceleration in the shells is evident across the entire band of radio frequencies observed with MeerKAT.

To better understand the origin of the GeV emission more Fermi-LAT data is required which can be used to study variability (AGN core origin) and fit a model to the GeV light curve to find support for the decline model (SN1996cr origin). CTA-South observations which could potentially resolve the lobes would enable investigating the GeV emission from the lobes. These observations with CTA could also be used to find GeV counterparts to the radio structures to better understand the lobe emission. Further reanalysis of H.E.S.S. observations could also constrain

the lobe structures to better understand its VHE emission.

References

Abdollahi, S., Acero, F., Ackermann, M., Ajello, M., Atwood, W. B., and Axelsson et al., M. (2020). Fermi Large Area Telescope Fourth Source Catalog. *ApJs*, 247(1):33.

Ackermann, M., Ajello, M., Allafort, A., Baldini, L., Ballet, J., and Bastieri et al., D. (2012). GeV Observations of Star-forming Galaxies with the Fermi Large Area Telescope. *ApJ*, 755(2):164.

Ackermann, M., Albert, A., Atwood, W. B., Baldini, L., Ballet, J., and Barbiellini et al., G. (2014). The Spectrum and Morphology of the Fermi Bubbles. *ApJ*, 793(1):64.

Aldrovandi, S. M. V. (1981). Supermassive black holes and emission lines of active galaxies and QSOs - Accretion rate, black hole mass, and photoionization models. *A&A*, 97(1):122–127.

Alloin, D., Johnson, R., and Lira, P. (2006). *Physics of Active Galactic Nuclei at all Scales*, volume 693.

Atwood, W. B., Abdo, A. A., Ackermann, M., Althouse, W., Anderson, B., and Axelsson et al., M. (2009). The Large Area Telescope on the Fermi Gamma-Ray Space Telescope Mission. *ApJ*, 697:1071–1102.

Baldwin, J. E. (1955). A survey of the integrated radio emission at a wave-length of 3.7 m. *MNRAS*, 115:684–689.

Ballet, J., Burnett, T. H., Digel, S. W., and Lott, B. (2020). Fermi Large Area Telescope Fourth Source Catalog Data Release 2. *arXiv e-prints*, page arXiv:2005.11208.

Bauer, F. (2007). Supernova 1996cr in ESO 97-G13 [with corrected sentence, re: Cbet 876]. *Central Bureau Electronic Telegrams*, 879:1.

Bauer, F. E., Brandt, W. N., Sambruna, R. M., Chartas, G., Garmire, G. P., and Kaspi et al., S. (2001). A Chandra Study of the Circinus Galaxy Point-Source Population. *AJ*, 122(1):182–193.

Bauer, F. E., Dwarkadas, V. V., Brandt, W. N., Immler, S., Smartt, S., and Bartel et al., N. (2008). Supernova 1996cr: SN 1987A's Wild Cousin? *ApJ*, 688(2):1210–1234.

Bisht, R. S., Ghosh, S. K., Iyengar, K. V. K., Rengarajan, T. N., Tandon, S. N., and Verma, R. P. (1990). Far Infrared Observations of Circinus and NGC4945 Galaxies. In Hollenbach, D. J. and Thronson, Harley A., J., editors, *NASA Conference Publication*, volume 3084, page 86.

Bland-Hawthorn, J. and Cohen, M. (2003). The Large-Scale Bipolar Wind in the Galactic Center. *ApJ*, 582(1):246–256.

Booth, R. S., de Blok, W. J. G., Jonas, J. L., and Fanaroff, B. (2009). MeerKAT Key Project Science, Specifications, and Proposals. *arXiv e-prints*.

Briggs, D. S. (1995). *High Fidelity Deconvolution of Moderately Resolved Sources*. PhD thesis, New Mexico Institute of Mining and Technology.

Carretti, E., Crocker, R. M., Staveley-Smith, L., Haverkorn, M., Purcell, C., and Gaensler et al., B. M. (2013). Giant magnetized outflows from the centre of the Milky Way. *Nature*, 493(7430):66–69.

Cherenkov Telescope Array Consortium, Acharya, B. S., Agudo, I., Al Samarai, I., Alfaro, R., and Alfaro et al., J. (2019). *Science with the Cherenkov Telescope Array*.

Chevalier, R. A. (1996). The Circumstellar Interaction Model for Radio Supernovae. In Taylor, A. R. and Paredes, J. M., editors, *Radio Emission from the Stars and the Sun*, volume 93 of *Astronomical Society of the Pacific Conference Series*, page 125.

Chevalier, R. A. (1998). Synchrotron Self-Absorption in Radio Supernovae. *ApJ*, 499:810–819.

Colafrancesco, S., Marchegiani, P., and Paulo, C. M. (2017). The correlation between radio power and Mach number for radio relics in galaxy clusters. *MNRAS*, 471(4):4747–4759.

CTA Consortium and Observatory. CTA Performance. `http://www.cta-observatory.org/science/cta-performance/(versionprod3b-v2)`.

CTA Consortium and Observatory. Southern Hemisphere Array. `https://www.cta-observatory.org/about/array-locations/chile/#1564040981984-d3f8f5dd-7690`.

Curran, S. J., Johansson, L. E. B., Bergman, P., Heikkilä, A., and Aalto, S. (2001). Molecular gas conditions in NGC 4945 and the Circinus galaxy. *A&A*, 367:457–469.

Curran, S. J., Johansson, L. E. B., Rydbeck, G., and Booth, R. S. (1998). A molecular ring in the Circinus galaxy. *A&A*, 338:863–873.

Curran, S. J., Rydbeck, G., Johansson, L. E. B., and Booth, R. S. (1999). A molecular outflow in the Circinus galaxy. *A&A*, 344:767–778.

Davies, R. E., Forbes, D. A., Ryder, S., Ashley, M. C. B., Burton, M., and Storey et al., J. W. V. (1998). Near-infrared line and radio continuum imaging of the Circinus galaxy. *MNRAS*, 293(2):189–196.

Dickinson, C. (2018). Large-Scale Features of the Radio Sky and a Model for Loop I. *Galaxies*, 6(2):56.

Egger, R. and Aschenbach, B. (1996). Interaction of the Loop I supershell with the Local Hot Bubble. In Zimmermann, H. U., Trümper, J., and Yorke, H., editors, *Roentgenstrahlung from the Universe*, pages 249–250.

Elmouttie, E., Haynes, R. F., Jones, K. L., Ehle, M., Beck, R., and Wielebinski, R. (1995). The polarized radio lobes of the Circinus galaxy. *MNRAS*, 275(4):L53–L59.

Elmouttie, M., Haynes, R. F., and Jones, K. L. (1997). 12CO J = 1 - 0 observations of the Circinus galaxy using the Mopra 22 M radio telescope. *pasa*, 14(2):140–45.

Elmouttie, M., Haynes, R. F., Jones, K. L., Sadler, E. M., and Ehle, M. (1998a). Radio continuum evidence for nuclear outflow in the Circinus galaxy. *MNRAS*, 297(4):1202–1218.

Elmouttie, M., Koribalski, B., Gordon, S., Taylor, K., Houghton, S., Lavezzi, T., Haynes, R., and Jones, K. (1998b). The kinematics of the ionized gas in the Circinus galaxy. *MNRAS*, 297(1):49–68.

Enßlin, T. A. and Gopal-Krishna (2001). Reviving fossil radio plasma in clusters of galaxies by adiabatic compression in environmental shock waves. *A&A*, 366:26–34.

Fanaroff, B. L. and Riley, J. M. (1974). The morphology of extragalactic radio sources of high and low luminosity. *MNRAS*, 167:31P–36P.

Finkbeiner, D. P. (2004). Microwave Interstellar Medium Emission Observed by the Wilkinson Microwave Anisotropy Probe. *ApJ*, 614(1):186–193.

For, B. Q., Koribalski, B. S., and Jarrett, T. H. (2012). Gas and star formation in the Circinus galaxy. *MNRAS*, 425(3):1934–1950.

Frater, R. H., Brooks, J. W., and Whiteoak, J. B. (1992). The Australia Telescope - Overview. *Journal of Electrical and Electronics Engineering Australia*, 12(2):103–112.

Freeman, K. C., Karlsson, B., Lynga, G., Burrell, J. F., van Woerden, H., and Goss et al., W. M. (1977). A large new galaxy in Circinus. *A&A*, 55:445–458.

Gardner, F. F. and Whiteoak, J. B. (1982). The Circinus galaxy - A second case of intense nuclear H2O emission. *MNRAS*, 201:13P–15P.

garner, R. (2018). Fermi mission overview. `https://www.nasa.gov/content/fermi-gamma-ray-space-telescope`. NASA.

Ghisellini, G., Maraschi, L., and Tavecchio, F. (2009). The Fermi blazars' divide. *MNRAS*, 396(1):L105–L109.

Ginzburg, V. L. and Syrovatskii, S. I. (1965). Cosmic Magnetobremsstrahlung (synchrotron Radiation). *ARAA*, 3:297.

Greenhill, L. J., Booth, R. S., Ellingsen, S. P., Herrnstein, J. R., Jauncey, D. L., and McCulloch et al., P. M. (2003). A Warped Accretion Disk and Wide-Angle Outflow in the Inner Parsec of the Circinus Galaxy. *ApJ*, 590(1):162–173.

Griffiths, R. E., Ptak, A., Feigelson, E. D., Garmire, G., Townsley, L., and Brandt et al., W. N. (2000). Hot Plasma and Black Hole Binaries in Starburst Galaxy M82. *Sci*, 290(5495):1325–1328.

Guo, F. and Mathews, W. G. (2012). The Fermi Bubbles. I. Possible Evidence for Recent AGN Jet Activity in the Galaxy. *ApJ*, 756(2):181.

Guo, X.-L., Xin, Y.-L., Liao, N.-H., and Fan, Y.-Z. (2019). The Circinus Galaxy Revisited with 10 yr Fermi-LAT Data. *ApJ*, 885(2):117.

H. E. S. S. Collaboration, Abdalla, H., Aharonian, F., Ait Benkhali, F., Angüner, E. O., and Arakawa et al., M. (2018). The starburst galaxy NGC 253 revisited by H.E.S.S. and Fermi-LAT. *A&A*, 617:A73.

Hallmann, S. (2015). *Search for a Neutrino Signal from the Fermi Bubbles with ANTARES Telescope*. PhD thesis, Friedrich-Alexander-Universität Erlangen-Nürnberg.

Harnett, J. I., Whiteoak, J. B., Reynolds, J. E., Gardnere, F. F., and Tzioumis, A. (1990). New radio observations of the Circinus galaxy. *MNRAS*, 244:130–132.

Hayashida, M., Stawarz, Ł., Cheung, C. C., Bechtol, K., Madejski, G. M., and Ajello et al., M. (2013). Discovery of GeV Emission from the Circinus Galaxy with the Fermi Large Area Telescope. *ApJ*, 779(2):131.

Heckman, T. M., Armus, L., and Miley, G. K. (1990). On the Nature and Implications of Starburst-driven Galactic Superwinds. *ApJs*, 74:833.

Irwin, J. A. and Saikia, D. J. (2003). Giant Metrewave Radio Telescope observations of NGC 3079. *MNRAS*, 346(3):977–986.

Jonas, J. and MeerKAT Team (2016). The MeerKAT Radio Telescope. In *Proceedings of MeerKAT Science: On the Pathway to the SKA. 25-27 May, 2016 Stellenbosch, South Africa (MeerKAT2016).*, page 1.

Jones, D. I., Crocker, R. M., Reich, W., Ott, J., and Aharonian, F. A. (2012). Magnetic Substructure in the Northern Fermi Bubble Revealed by Polarized Microwave Emission. *ApJL*, 747(1):L12.

Józsa, G. I. G., White, S. V., Thorat, K., Smirnov, O. M., Serra, P., and Ramatsoku et al., M. (2020). MeerKATHI – an end-to-end data reduction pipeline for MeerKAT and other radio telescopes. *arXiv e-prints*, page arXiv:2006.02955.

Kaneda, H., Suzuki, T., Yamagishi, M., Onaka, T., Ishihara, D., and Sakon et al., I. (2010). AKARI far-infrared observations of the ISM in nearby galaxies. In *Astronomical Society of India Conference Series*, volume 1, pages 91–97.

Kantzas, D., Petropoulou, M., and Mastichiadis, A. (2016). Early-time signatures of γ-ray emission from supernovae in dense circumstellar media. In *Supernova Remnants: An Odyssey in Space after Stellar Death*, page 139.

Kataoka, J., Sofue, Y., Inoue, Y., Akita, M., Nakashima, S., and Totani, T. (2018). X-Ray and Gamma-Ray Observations of the Fermi Bubbles and NPS/Loop I Structures. *Galaxies*, 6(1):27.

Kellermann, K. I., Sramek, R., Schmidt, M., Shaffer, D. B., and Green, R. (1989). VLA Observations of Objects in the Palomar Bright Quasar Survey. *AJ*, 98:1195.

Kennicutt, Robert C., J. (1998). The Global Schmidt Law in Star-forming Galaxies. *ApJ*, 498(2):541–552.

Kennicutt, R. C. and Evans, N. J. (2012). Star Formation in the Milky Way and Nearby Galaxies. *ARAA*, 50:531–608.

Kharb, P., O'Dea, C. P., Baum, S. A., Hardcastle, M. J., Dicken, D., and Croston et al., J. H. (2014). Very Large Baseline Array observations of Mrk 6: probing the jet-lobe connection. *MNRAS*, 440(4):2976–2987.

Kraft, R. P., Vázquez, S. E., Forman, W. R., Jones, C., Murray, S. S., and Hardcastle et al., M. J. (2003). X-Ray Emission from the Hot Interstellar Medium and

Southwest Radio Lobe of the Nearby Radio Galaxy Centaurus A. *A&A*, 592:129–146.

Landau, L. D. and Lifshitz, E. M. (1959). *Fluid mechanics*.

Leahy, J. P., Bridle, A. H., and Strom, R. G. (2013). An Atlas of DRAGNs.

Lyngå, G. and Hansson, N. (1972). Nebulae of the Southern Milky Way: An Atlas. *A&A*, 6:327.

Maldera, S., Wood, M., Caputo, R., Riccardo, R., Charles, E., Digel, S., and Baldini, L. (2019). Fermi LAT Performance. `https://www.slac.stanford.edu/exp/glast/groups/canda/lat_Performance.htm`. Stanford: SLAC National Accelerator Laboratory.

Marconi, A., Moorwood, A. F. M., Origlia, L., and Oliva, E. (1994). A prominent ionization cone and starburst ring in the nearby Circinus galaxy. *The Messenger*, 78:20–24.

Massaro, E., Tramacere, A., Perri, M., Giommi, P., and Tosti, G. (2006). Log-parabolic spectra and particle acceleration in blazars. III. SSC emission in the TeV band from Mkn501. *A&A*, 448(3):861–871.

Matthews, T. A., Morgan, W. W., and Schmidt, M. (1964). A Discussion of Galaxies Indentified with Radio Sources. *ApJ*, 140:35.

Mebold, U., Goss, W. M., van Woerden, H., and Freeman, K. C. (1977). Radio observations of the Circinus galaxy. *Proceedings of the Astronomical Society of Australia*, 3:72–74.

Meunier, C., Bauer, F. E., Dwarkadas, V. V., Koribalski, B., Emonts, B., and Hunstead et al., R. W. (2013). Performing a stellar autopsy using the radio-bright remnant of SN 1996cr. *MNRAS*, 431:2453–2463.

Mingo, B., Hardcastle, M. J., Croston, J. H., Evans, D. A., Kharb, P., and Kraft et al., R. P. (2012). Shocks, Seyferts, and the Supernova Remnant Connection: A Chandra Observation of the Circinus Galaxy. *ApJ*, 758(2):95.

Mirabal, N. (2019). Fermi science support centre: Analysis thread. `https://fermi.gsfc.nasa.gov/ssc/data/analysis/scitools/`. NASA: Goddard Space Flight Center.

Molinari, S., Bally, J., Noriega-Crespo, A., Compiègne, M., Bernard, J. P., and Paradis et al., D. (2011). A 100 pc Elliptical and Twisted Ring of Cold and Dense Molecular Clouds Revealed by Herschel Around the Galactic Center. *ApJl*, 735(2):L33.

Monnier, J. D. and Allen, R. J. (2013). *Radio and Optical Interferometry: Basic Observing Techniques and Data Analysis*, page 325.

Moorwood, A. F. M. and Glass, I. S. (1984). Infrared activity in Circinus and NGC 4945 : two galaxies containing luminous H2O masers. *A&A*, 135:281–288.

Muxlow, T., Beswick, R. J., Richards, A. M. S., and Thrall, H. J. (2006). Starburst galaxies. In *Proceedings of the 8th European VLBI Network Symposium*, page 31.

Nayana A., J., Chandra, P., and Ray, A. K. (2018). Long-term Behavior of a Type IIP Supernova SN 2004dj in the Radio Bands. *ApJ*, 863:163.

Nazarova, L. S., O'Brien, P. T., and Ward, M. J. (1999). The effect of an attenuated continuum on the coronal line spectrum of NGC 1068 and the Circinus galaxy. *A&A*, 343:682–690.

Offringa, A. R., McKinley, B., Hurley-Walker, N., Briggs, F. H., Wayth, R. B., and Kaplan et al., D. L. (2014). WSCLEAN: an implementation of a fast, generic wide-field imager for radio astronomy. *MNRAS*, 444(1):606–619.

Oliva, E., Salvati, M., Moorwood, A. F. M., and Marconi, A. (1994). Size and physical conditions of the coronal line region in a nearby Seyfert 2: the Circinus galaxy. *A&A*, 288:457–465.

Padovani, P. (1997). Gamma-Ray Emitting AGN and Unified Schemes. In Giraud-Heraud, Y. and Tran Thanh van, J., editors, *Very High Energy Phenomena in the Universe; Moriond Workshop*, page 7.

Porter, T. A., Moskalenko, I. V., and Strong, A. W. (2006). Inverse Compton Emission from Galactic Supernova Remnants: Effect of the Interstellar Radiation Field. *ApJL*, 648(1):L29–L32.

Predehl, P., Sunyaev, R. A., Becker, W., Brunner, H., Burenin, R., and Bykov et al., A. (2020). Detection of large-scale X-ray bubbles in the Milky Way halo. *Nature*, 588(7837):227–231.

Protheroe, R. J. (2002). Factors Determining Variability Time in Active Galactic Nucleus Jets. *Publ. Astron. Soc. Australia*, 19(4):486–498.

Roy, A. L., Goss, W. M., and Anantharamaiah, K. R. (2008). Detection of the H92α recombination line from the starbursts in the Circinus galaxy and NGC 1808. *A&A*, 483(1):79–88.

Sambruna, R. M., Netzer, H., Kaspi, S., Brandt, W. N., Chartas, G., and Garmire et al., G. P. (2001). High-Resolution X-Ray Spectroscopy of the Seyfert 2 Galaxy Circinus with Chandra. *ApJL*, 546(1):L13–L17.

Singh, V., Ishwara-Chandra, C. H., Sievers, J., Wadadekar, Y., Hilton, M., and Beelen, A. (2015). Discovery of rare double-lobe radio galaxies hosted in spiral galaxies. *MNRAS*, 454(2):1556–1572.

Snowden, S. L., Egger, R., Freyberg, M. J., McCammon, D., Plucinsky, P. P., and Sanders et al., W. T. (1997). ROSAT Survey Diffuse X-Ray Background Maps. II. *ApJ*, 485(1):125–135.

Spoelstra, T. A. T. (1973). Galactic Loops as Supernova Remnants in the Local Galactic Magnetic Field. *A&A*, 24:149.

Su, M. and Finkbeiner, D. P. (2012). Double Gamma-ray Lines from Unassociated Fermi-LAT Sources. *arXiv e-prints*, page arXiv:1207.7060.

Su, M., Slatyer, T. R., and Finkbeiner, D. P. (2010). Giant Gamma-ray Bubbles from Fermi-LAT: Active Galactic Nucleus Activity or Bipolar Galactic Wind? *ApJ*, 724(2):1044–1082.

Tang, Q.-W., Wang, X.-Y., and Tam, P.-H. T. (2014). Discovery of GeV Emission from the Direction of the Luminous Infrared Galaxy NGC 2146. *ApJ*, 794(1):26.

Taylor, G. B., Carilli, C. L., and Perley, R. A., editors (1999). *Synthesis Imaging in Radio Astronomy II*, volume 180 of *Astronomical Society of the Pacific Conference Series*.

Thompson, A. R. (1989). The Interferometer in Practice. In Perley, R. A., Schwab, F. R., and Bridle, A. H., editors, *Synthesis Imaging in Radio Astronomy*, volume 6 of *Astronomical Society of the Pacific Conference Series*, page 11.

Thompson, A. R., Moran, J. M., and Swenson, George W., J. (2017). *Interferometry and Synthesis in Radio Astronomy, 3rd Edition*.

Tomisaka, K. and Ikeuchi, S. (1988). Starburst Nucleus: Galactic Scale Bipolar Flow. *ApJ*, 330:695.

Tramacere, A., Giommi, P., Perri, M., Verrecchia, F., and Tosti, G. (2009). Swift observations of the very intense flaring activity of Mrk 421 during 2006. I. Phenomenological picture of electron acceleration and predictions for MeV/GeV emission. *A&A*, 501(3):879–898.

Tramacere, A., Massaro, E., and Taylor, A. M. (2011). Stochastic Acceleration and the Evolution of Spectral Distributions in Synchro-Self-Compton Sources: A Self-consistent Modeling of Blazars' Flares. *ApJ*, 739(2):66.

Urry, C. M. and Padovani, P. (1995). Unified Schemes for Radio-Loud Active Galactic Nuclei. *PASP*, 107:803.

Vink, J. (2012). Supernova remnants: the X-ray perspective. *A&A Rev*, 20:49.

Vink, J. (2017). *X-Ray Emission Properties of Supernova Remnants*, page 2063.

Vink, J. and Yamazaki, R. (2014). A Critical Shock Mach Number for Particle Acceleration in the Absence of Pre-existing Cosmic Rays: M= $\sqrt{5}$. *ApJ*, 780(2):125.

Whiteoak, J. B. and Bunton, J. D. (1985). FST observations of NGC 4945 and the Circinus galaxy. *Proceedings of the Astronomical Society of Australia*, 6:171–174.

Wilson, A. S. and Ulvestad, J. S. (1982). Radio structures of Seyfert galaxies. IV. Jets (?) in NGC 1068, and NGC 4151. *ApJ*, 263:576–594.

Wilson, A. S. and Ulvestad, J. S. (1987). A Radiative Bow Shock Wave (?) Driven by Nuclear Ejecta in a Seyfert Galaxy. *ApJ*, 319:105.

Woosley, S. and Janka, T. (2005). The physics of core-collapse supernovae. *Nature Physics*, 1(3):147–154.

Worrall, D. M. (2004). AGN: cores and jets. In *AAS/High Energy Astrophysics Division #8*, AAS/High Energy Astrophysics Division, page 32.01.

Xi, S.-Q., Liu, R.-Y., Wang, X.-Y., Yang, R.-Z., Yuan, Q., and Zhang, B. (2020). A Serendipitous Discovery of GeV Gamma-Ray Emission from Supernova 2004dj in a Survey of Nearby Star-forming Galaxies with Fermi-LAT. *ApJL*, 896(2):L33.

Young, A. J., Wilson, A. S., and Shopbell, P. L. (2001). A Chandra X-Ray Study of NGC 1068. I. Observations of Extended Emission. *A&A*, 556(1):6–23.

Zhang, R. and Guo, F. (2020). Simulating the Fermi Bubbles as Forward Shocks Driven by AGN Jets. *ApJ*, 894(2):117.

Zubovas, K., King, A. R., and Nayakshin, S. (2011). The Milky Way's Fermi bubbles: echoes of the last quasar outburst? *MNRAS*, 415(1):L21–L25.